



Universidad de Valladolid



PROGRAMA DE DOCTORADO EN INVESTIGACIÓN BIOMÉDICA

TESIS DOCTORAL:

**New insights into the role of mitochondrial
respiration in macrophage functions**

Presentada por Dino Joaquín Gobelli para optar al
grado de

Doctor por la Universidad de Valladolid

Dirigida por:

Dr. Miguel Ángel de la Fuente García

Dra. María Simarro Grande

Some of the original results presented in this thesis have been compiled in the following **scientific publications**:

- **Gobelli D**, Serrano-Lorenzo P, Esteban-Amo MJ, Serna J, Pérez-García MT, Orduña A, Jourdain AA, Martín-Casanueva MÁ, Á de la Fuente M, Simarro M. The mitochondrial succinate dehydrogenase complex controls the STAT3-IL-10 pathway in inflammatory macrophages. *iScience*. 2023;26(8):107473. Published 2023 Jul 25. doi:10.1016/j.isci.2023.107473
- P. Serrano-Lorenzo*, **D. Gobelli***, R. Garrido-Moraga, M.J. Esteban-Amo, J.R. López-López, A. Orduña, M.A. de la Fuente, M.A. Martín, M. Simarro. Development of a novel in vitro model to study the modulatory role of the respiratory complex I in macrophage effector functions. *PLoS ONE* 18(9): e0291442. Published 2023 Sep 19. <https://doi.org/10.1371/journal.pone.0291442>. * Contributed equally to this work.

In addition, results from other research projects within this thesis resulted in contributions to the following publications:

- Magraner-Pardo L, **Gobelli D**, de la Fuente MA, Pons T, Simarro M. Systematic Analysis of FASTK Gene Family Alterations in Cancer. *International Journal of Molecular Sciences*. 2021; 22(21):11337. <https://doi.org/10.3390/ijms222111337>
- Serna, J., Peraza, D. A., Moreno-Estar, S., Saez, J. J., **Gobelli, D.**, Simarro, M., Hivroz, C., López-López, J. R., Ciudad, P., Fuente, M. A. d. I., & Pérez-García, M. T.. Characterization of endogenous Kv1.3 channel isoforms in T cells. *Journal of Cellular Physiology*. 2023; 238, 976–991. <https://doi.org/10.1002/jcp.30984>
- Bernardi A*, **Gobelli D***, Serna J*, Nawrocka P*, March-Rosselló G, et al. Novel fluorescent-based reporter cell line engineered for monitoring homologous recombination events. *PLOS ONE*. 2021; 16(4): e0237413.

<https://doi.org/10.1371/journal.pone.0237413>. * Contributed equally to this work.

- Montero-Jodra, A, de la Fuente MA, **Gobelli D**, Martín-Fernández M, Villar J, Tamayo E, Simarro M. The mitochondrial signature of cultured endothelial cells in sepsis: Identifying potential targets for treatment. *Biochimica et Biophysica Acta (BBA) - Molecular Basis of Disease*. 2024, 166946, ISSN 0925-4439, <https://doi.org/10.1016/j.bbadis.2023.166946>.

Funding:

This thesis has been carried out under the supervision of Prof. Miguel Ángel de la Fuente García and Prof. María Simarro Grande at the Instituto de Biología y Genética Molecular (Universidad de Valladolid-CSIC), Valladolid. It has been possible thanks to the following funding:

Project: Ministerio de Ciencia e Innovación, PID2020-118517RB-I00 Consejería de Educación, Junta de Castilla y León, VA172P20 Consejería de Sanidad, Junta de Castilla y León, GRS 2201/A/2020 Instituto de Salud Carlos III, PI21/00381 Junta de Castilla y León, CCVC8485.

Contrato predoctoral Universidad de Valladolid-Banco Santander. From 2019 to 2023.

Universidad de Valladolid and ERASMUS+ Mobility Grants to conduct research in the lab of Dr. Alexis Jourdain in the Université de Lausanne, Switzerland

Index

Index	I
Abbreviations.....	V
Abstract	IX
Resumen	XI
Introduction.....	1
1. Immune system.....	1
2. Macrophages	3
3. Mitochondria	11
4. Role of mitochondrial complexes in macrophage polarization	24
Hypothesis.....	29
Objectives.....	29
Material and Methods	33
1. Cell Line and Culture Conditions:.....	33
2. Assay for cell proliferation	43
3. Gene expression analysis	43
4. Total protein extraction and Western blot analysis.....	45
5. Mitochondrial protein studies	46
6. Detection of mitochondrial ROS.....	47
7. Measurement of Mitochondrial Membrane Potential (MMP)	48
8. Phagocytosis assay in RAW 264.7 macrophages.....	49
9. Gentamicin protection assay.....	50
10. Determination of intracellular metabolite concentration.....	52
11. Cytokine detection assay in macrophages.....	54
12. NO detection assay in RAW 264.7 macrophages	55

13. Seahorse XF assay in RAW 264.7 macrophages	56
14. Electron transport chain (ETC) activities	59
15. Statistical analysis	60
Results	65
Chapter 1: Generation of RAW 264.7 <i>Ndufs4</i> ^{-/-} , <i>Sdha</i> ^{-/-} and <i>Sdhb</i> ^{-/-} lines	65
1. Generation of plasmids for gene editing of RAW 264.7 cells	65
2. Generation of RAW 264.7 KO cells for <i>Ndufs4</i> , <i>Sdha</i> , and <i>Sdhb</i>	70
Chapter 2: Role of CI in macrophage respiration and effector functions	73
1. Impact on ETC activities	73
2. Evaluation of mitochondrial respiratory profile	75
3. Changes in mitochondrial function	77
4. Stability of CI subunits in <i>Ndufs4</i> ^{-/-} macrophages.....	78
5. Analysis of distribution pattern of free ETC complexes and SCs	79
6. CI Activity assessment in <i>Ndufs4</i> ^{-/-} Cells by In-Gel Activity (IGA) assay	80
7. <i>Ndufs4</i> controls macrophage effector functions	81
Chapter 3: Role of SDH/CII in macrophage respiration and effector functions.....	85
1. Characterization of <i>Sdha</i> ^{-/-} and <i>Sdhb</i> ^{-/-} macrophages	85
2. Role of SDH/CII in cytokine response	92
3. NO production	97
4. Phagocytosis and bactericidal activity of macrophages without SDH/CII.....	99
5. Effects of SDH/CII deficiency on signaling pathways	101
6. Changes in TCA metabolites in <i>Sdha</i> ^{-/-} and <i>Sdhb</i> ^{-/-} macrophages	110
7. MitoROS as a potential inhibitor of Stat3 Y705 phosphorylation	113
Discussion	117
Conclusions.....	131

References	133
Annexes	151
Table 1: Oligonucleotides and primers used for cloning	153
Table 2: Primers used for PCR and sequencing	154
Table 3: Primers used for real-time PCR	154
Table 4: Antibodies used for Western blot	155
Table 5: Target site sequencing of <i>Ndufs4</i>^{-/-}, <i>Sdha</i>^{-/-} and <i>Sdhb</i>^{-/-} clones	157
Table 6: Key resources table	159
Solutions composition	163



Abbreviations

ADP: Adenosine diphosphate
AMPK: AMP-Activated Protein Kinase
Arg1: Arginase-1
ATP: Adenosine triphosphate
BMDMs: Bone marrow-derived macrophages
BN-PAGE: Blue-native gel electrophoresis
BSA: Bovine serum albumin
cDNA: Complementary DNA
CI: Complex I
CII: Complex II
CIII: Complex III
CIV: Complex IV
CS: Citrate synthase
DCPIP: 2,6-dichlorophenol-indophenol
DMEM: Dulbecco's Modified Eagle Medium
DMF: Dimethyl fumarate
DMM: Dimethyl malonate
ECAR: Extracellular acidification rate
ELISA: Enzyme-linked immunosorbent assay
ETC: Electron transport chain
FAD: Flavin adenine dinucleotide
FADH₂: Reduced flavin adenine dinucleotide
FCCP: Carbonyl cyanide (4-trifluoromethoxy) phenyl-hydrazone
Fe-S: Iron-sulfur
FITC: Fluorescein isothiocyanate
FMN: Flavin mononucleotide
gRNA: Single-guide RNA
GTP: Guanosine triphosphate
HDR: Homology-directed repair

HITI: Homology-Independent Targeted Integration
HKEC: Heat-killed *E. coli*
HRP: Horseradish peroxidase
IGA: In-Gel Activity
IL: Interleukin
IMM: Inner mitochondrial membrane
iNOS: Inducible nitric oxide synthase
IRF: Interferon regulatory factor
ISP: Iron-sulfur protein
KO: Knock-out
LPS: Lipopolysaccharide
Midiprep: Medium-scale plasmid purification
MitoROS: Mitochondrial ROS
MMP or $\Delta\psi$: Mitochondrial membrane potential
MOI: Multiplicity of infection
NBT: Nitro blue tetrazolium
NHEJ: Utilizes non-homologous end joining
NLRs: Nod-like receptors
NO: Nitric oxide
OCR: Oxygen consumption rate
OD: Optical density
OI: 4-octyl itaconate
OXPHOS: Oxidative phosphorylation
PAMPs: Pathogen-associated molecular patterns
PBS: Phosphate-buffered saline
PCR: Polymerase chain reaction
PGs: Prostaglandins
PHD: Hydroxylase domains enzymes
PRRs: Pattern recognition receptors
PVDF: Polyvinylidene difluoride
q-PCR: Quantitative PCR

RNS: Reactive nitrogen species

ROS: Reactive oxygen species

RT-PCR: Reverse Transcription PCR

SCs: Supercomplexes

SDH: Succinate dehydrogenase

STAT: Signal Transducer and Activator of Transcription

TBS-T: Tris-Buffered Saline with Tween 20

TCA: Tricarboxylic acid

TLR: Toll-like receptors

TNF- α : Tumor necrosis factor α

UPLC-MS: Ultra-performance liquid chromatography-mass spectrometry



Abstract

The interplay between the activation of innate immune cells, in particular macrophages, and their energy metabolism has gained considerable interest in the scientific community. Macrophages play critical roles in the innate immune response and their functional capabilities are strongly influenced by their metabolic status. However, the precise impact of the mitochondrial electron transport chain (ETC) on macrophage functions is an aspect that remains poorly understood. This thesis investigates the intricate interplay between ETC complexes, in particular complex I (CI) and complex II (CII), and macrophage responses. The innovative CRISPR/Cas9 HITI technique was used to create knockout (KO) models in the mouse macrophage cell line RAW 264.7, targeting the genes *Ndufs4* (complex I) and *Sdha*, *Sdhb* (complex II). The absence of *Ndufs4* impaired CI activity, thereby affecting macrophage metabolism with reduced basal respiration and ATP production, coupled with an increased mitochondrial ROS levels. *Ndufs4*^{-/-} macrophages displayed an altered cytokine response with increased IL-6 and decreased IL-10 production, suggesting a shift towards a pro-inflammatory state, associated with enhanced phagocytic capacity. *Sdha*^{-/-} and *Sdhb*^{-/-} macrophages exhibited reduced succinate dehydrogenase (SDH) activity, severe impaired respiratory capacity and an altered cytokine response. Macrophages lacking these subunits showed reduced stabilization of HIF-1 α and a reduced production of the pro-inflammatory cytokine IL-1 β upon LPS activation. In addition, these subunits were found to be essential for the synthesis of IL-10 following LPS stimulation, a critical cytokine that acts to dampen the macrophage inflammatory response. The study also identified important changes in key signaling pathways, highlighting the role of redox balance in Stat3-IL-10 signaling. The results reveal a complex regulatory network in which mitochondrial complexes influence macrophage metabolism, signaling pathways and ultimately immune responses.



Resumen

La interacción entre la activación de los macrófagos y su metabolismo energético ha sido objeto de estudio en la comunidad científica. Los macrófagos desempeñan un papel fundamental en la respuesta inmunitaria innata y su capacidad funcional depende en gran medida de su estado metabólico. Sin embargo, el impacto preciso de la cadena mitocondrial de transporte de electrones (ETC) en las funciones de los macrófagos es un aspecto que sigue siendo poco conocido. Esta tesis investiga la compleja interacción entre los complejos ETC, en particular el complejo I (CI) y el complejo II (CII), y las respuestas de los macrófagos. Utiliza la innovadora técnica CRISPR/Cas9 HITI para generar modelos *knockout* (KO) dentro de la línea celular de macrófagos murinos RAW 264.7, dirigiéndose específicamente a los genes *Ndufs4*, (subunidad de CI) y *Sdha*, *Sdhb* (subunidades de CII). La ausencia de *Ndufs4* deteriora la actividad de la CI, afectando así al metabolismo de los macrófagos con una reducción de la respiración basal y de la producción de ATP, junto con un aumento de los niveles de ROS mitocondriales. Los macrófagos *Ndufs4*^{-/-} mostraron una respuesta alterada de citoquinas con una mayor producción de IL-6 y menor de IL-10, lo que sugiere un cambio hacia un estado proinflamatorio, junto con una mayor capacidad fagocítica. Los macrófagos *Sdha*^{-/-} y *Sdhb*^{-/-} mostraron una actividad reducida de la Succinato Deshidrogenasa (SDH), una capacidad respiratoria muy disminuida y una respuesta de citoquinas alterada. Los macrófagos deficientes en estas subunidades mostraron una menor estabilización de HIF-1 α y una menor producción de la citocina proinflamatoria IL-1 β tras la activación por LPS. Además, estas subunidades resultaron esenciales para la síntesis de IL-10 tras la estimulación con LPS, una citoquina crítica que actúa para moderar la respuesta inflamatoria de los macrófagos. El estudio también identificó cambios importantes en vías de señalización clave, destacando el papel del equilibrio redox en la señalización de Stat3. Los resultados revelan una compleja red de regulación en la que los complejos mitocondriales influyen en el metabolismo de los macrófagos, las vías de señalización y, en última instancia, las respuestas inmunitarias.





Introduction



Introduction


1. Immune system

The immune system is a sophisticated and intricate network of heterogeneous cells that play an essential role in maintaining homeostasis and responding to foreign antigens, including bacteria, fungi, parasites, viruses, cancer cells, and toxins. It can be categorized into two interconnected branches: the innate immune system and the adaptive immune system.

The innate immune system is characterized by its rapid response and nonspecific elimination of invading pathogens. It comprises myeloid cells, as well as innate lymphoid cells, all of which are instrumental in processes like phagocytosis, killing and cytokine production, contributing to antimicrobial defense¹. On the other hand, the adaptive immune system is distinguished by its specificity and memory and consists of B and T lymphocytes. These cells provide long-lasting protection against reinfection by the same microorganism following the initial exposure to the pathogen. The response of the adaptive immune system is slower compared to the innate immune system due to the need for lymphocytes to be activated by antigen-presenting cells and undergo clonal expansion to generate a specific response to the antigen.

1.1 Innate immune system

The first line of defense against microbial invasion is provided by the anatomical and physiological barriers of the skin and mucous membranes. These barriers include layers of epithelial cells tightly bound together by tight junctions, creating a physical obstacle to pathogen penetration. Additionally, in epithelia such as those in the respiratory, gastrointestinal, and genitourinary tracts, the surface is covered by cilia and a layer of secreted mucus. Epithelial cilia allow for the constant movement and renewal of mucus so that foreign particles are expelled from the body. Other mechanisms of innate defense involve small bioactive molecules, such as complement proteins, defensins, antimicrobial peptides, and other soluble



substances. Finally, the innate immune response is mediated by a wide variety of cells, including macrophages, neutrophils, basophils, eosinophils, innate lymphoid cells, dendritic cells, and mast cells. They have crucial functions in host defense, such as phagocytosis of pathogens, release of antimicrobial proteases, killing and production of cytokines and chemokines that attract and stimulate other immune cells. Macrophages and dendritic cells also participate in antigen presentation, which is fundamental for initiating adaptive immune responses.

As mentioned earlier, the innate immune response is characterized by rapid activation, partly due to the antigen recognition strategy. Unlike the adaptive immune system, which is characterized by a diversity of receptors, each specialized for a unique antigen, the innate immune system employs a limited repertoire of germline encoded pattern recognition receptors (PRRs). These receptors recognize pathogen-associated molecular patterns (PAMPs), which are common motifs found in related microbial groups or conserved within a particular class of microbes. In addition to their ability to recognize PAMPs, PRRs can also detect damage-associated molecular patterns (DAMPs) released by damaged or dying host cells. This can occur in response to various stressors, including infection, trauma, or tumor transformation. PRRs are widely expressed on a large number of cells, allowing the innate system to respond rapidly to an invading disease or toxin.

PRRs are divided into families, including Toll-like receptors (TLR), Nod-like receptors (NLR), with humans having at least 10 TLR genes and 23 NLR genes, and mice having 12 TLR genes and 34 NLR genes. Additionally, there are C-type lectin receptors (CLR). PRRs can form different heterodimers and also employ various adapters to transmit signals, leading to an overlap of signaling pathways. As a result, the immune response to some signals is redundant and has a synergistic impact.

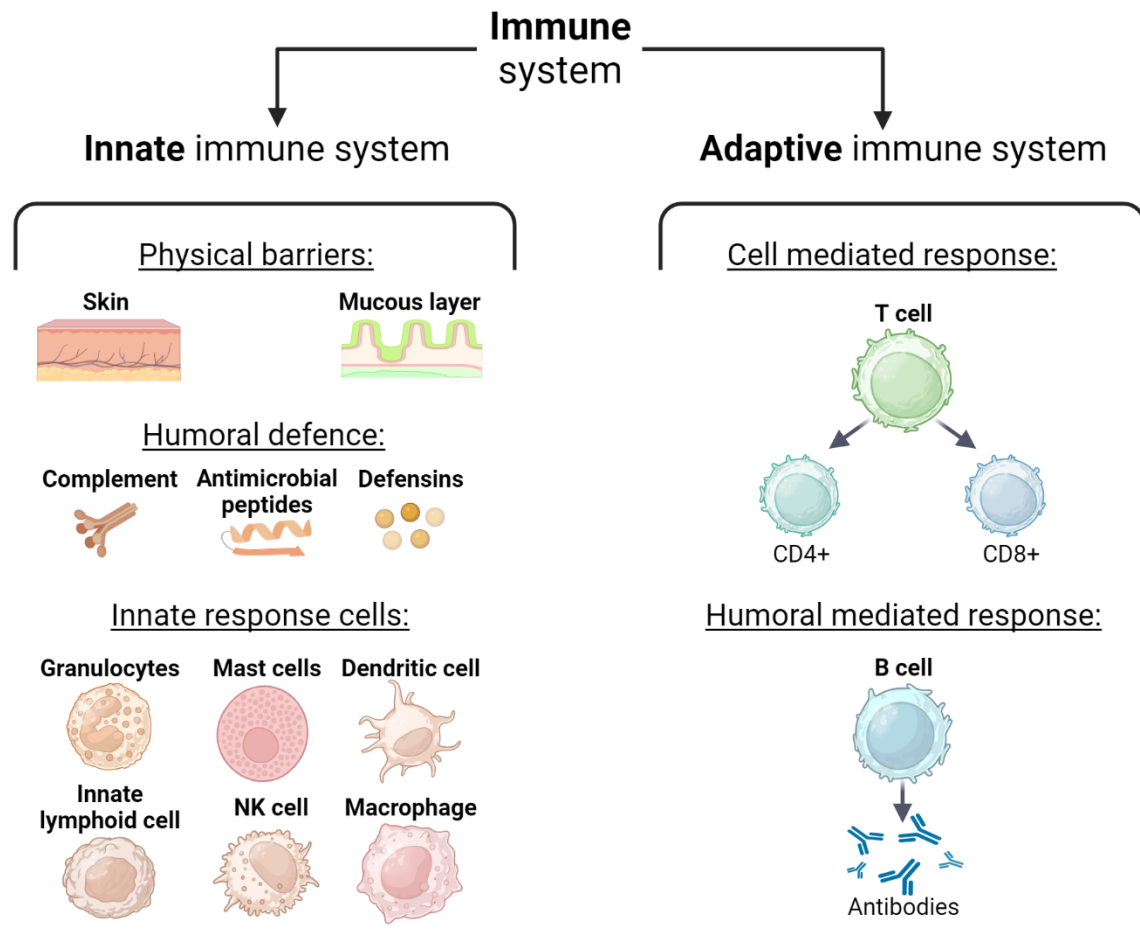


Figure 1: An overview of the immune system, illustrating the components of the innate and adaptive immune systems. The innate immune system consists of physical and bioactive molecular barriers and an initial inflammatory response involving macrophages, mast cells, dendritic cells, granulocytes, innate lymphoid cells and natural killer cells. The adaptive immune response is mediated by B and T cells, which generate a specialized and acquired immune response to specific pathogens through antibodies and CD4+ and CD8+ cells. Source: Self-elaborated with BioRender.

2. Macrophages

Phagocytic cells, such as macrophages, are key elements in immune responses. These cells are highly versatile, playing an important role in maintaining tissue homeostasis and defending against pathogens. Macrophages are found in numerous tissues and organs throughout the body and exhibit a high degree of plasticity, being able to differentiate into different functional states depending on the tissue microenvironment. Macrophages can be derived from monocytes in the

circulation, which differentiate into mature macrophages upon entering tissues. However, some macrophages are tissue-resident and have a fetal origin, meaning they are derived from embryonic progenitors and are maintained in the tissues throughout life.

The various functions of macrophages in different tissues are achieved in part through the activation of specific signaling pathways and transcriptional programs, which are influenced by unique signals in each tissue's niche. For example, macrophages in the liver (Kupffer cells) are responsible for the removal of damaged or senescent erythrocytes and maintain iron homeostasis, while alveolar macrophages in the lungs are involved in the clearance of foreign particles and protection against respiratory infections. Finally, it is relevant to mention that macrophages also play a crucial role in tissue development by shaping tissue architecture and modulating cellular proliferation and differentiation.

2.1 Role in infection

Macrophages act as one of the first lines of defense against invasive pathogens in the early stages of an infection. These cells use phagocytosis, a process in which they engulf and destroy harmful particles, to control inflammation and eliminate necrotic or apoptotic cells generated by pathogens. This process involves the interaction of receptors on macrophages with ligands on the surface of microbes or other particles, leading to the internalization of particles through an actin-based mechanism². Once engulfed, macrophages direct the material into an intracellular organelle called the phagosome. The phagosome undergoes a series of transformations, interacting with endosomes and lysosomes. The phagosome then matures into a phagolysosome, a highly hydrolytic and bactericidal compartment. Macrophages use different strategies to eliminate bacteria. One primary method involves the acidification of the phagolysosome, effectively disrupting bacterial metabolism³. Simultaneously, hydrolytic enzymes like lysozymes are released to break down bacterial cell walls, while antimicrobial peptides known as defensins create ionic imbalances within bacterial cells, ultimately causing their death⁴. Nutrient deprivation is another strategy; macrophages can use scavenger molecules

like lactoferrin, which sequesters Fe^{2+} , to deprive bacteria of essential nutrients needed for growth⁵. Alternatively, macrophages can also employ reactive molecules to eliminate bacteria, known as reactive oxygen species (ROS) and reactive nitrogen species (RNS). ROS generated by NADPH oxidase in phagocytic cells contribute to the elimination of many bacteria. Nitric oxide (NO) produced by inducible nitric oxide synthase (iNOS, also named NOSII or NOS2), can react to form S-nitrosothiols or react with ROS to form peroxynitrite, which contributes to the early elimination of microbes in the phagolysosomes⁶⁻⁸. In addition to recognizing and engulfing pathogens through phagocytosis, macrophages release a variety of pro-inflammatory cytokines and chemokines to enhance their antimicrobial activity. They also activate the adaptive immune system by presenting antigens through the major histocompatibility complex (MHCII) to T cells and secreting cytokines that help regulate the immune response.

As the infection resolves, macrophages switch to an anti-inflammatory phenotype, helping to suppress the immune response and promoting tissue repair. During tissue repair, macrophages play a critical role in wound healing and regeneration. They secrete a variety of growth factors and soluble mediators that promote fibroblast differentiation, extracellular matrix formation, and tissue remodeling.

2.2 Macrophage polarization

Macrophages are versatile immune cells that respond to different signals from pathogens and the extracellular environment, leading to diverse functions regulated by different signaling pathways. This diversity of phenotypic states is referred to as macrophage polarization and results in significant changes in gene expression that influence their responsiveness to immune stimuli.

Activation of macrophages is commonly delineated into two principal types based on the stimuli and the achieved transcriptional changes: the classical pro-inflammatory or M1 type and the alternatively activated or M2 type considered anti-inflammatory and associated with tissue repair, remodeling and immune regulation. However, activation is heterogeneous within the M1 and M2 categories, with different polarizing stimuli leading to different subsets of markers and functional responses.

Thus, a more precise characterization has been proposed based on the specific signals used to induce activation⁹.

M1 polarization is a state of activation that is induced by TLR agonists, including PAMPS such as lipopolysaccharide (LPS), and cytokines such as IFN- γ and tumor necrosis factor α (TNF- α). LPS, a ligand for TLR4, activates a multireceptor complex consisting of LPS-binding protein (LBP), CD14, and MD-2¹⁰⁻¹². This complex triggers a signaling cascade that involves the adaptor protein Myeloid Differentiation Primary Response 88 (MyD88), along with other adaptors and kinases that activate the kinases IKK, p38, and JNK, ultimately leading to the activation of the transcription factors NF- κ B and AP-1^{13,14}. These transcription factors promote the expression of pro-inflammatory cytokines, including Interleukin (IL)-1, IL-6, IL-12, and IL-23, as well as inflammatory intermediates including ROS and RNS. In addition to NF- κ B and AP-1, Signal Transducer and Activator of Transcription (STAT)1/3, Interferon Regulatory Factor (IRF) 5 and activin A are some of the key transcription factors involved in macrophage M1 polarization¹⁵⁻¹⁷.

The alternative activation of macrophages is induced by stimuli such as IL-4 and IL-13. These cytokines activate specific signaling pathways, for example, IL-4 binds to IL-4 receptor alpha (IL-4R α) and leads to the activation of the STAT6. STAT6 promotes the expression of several genes that are involved in the induction of M2 polarization, including Arginase-1 (Arg1), Resistin-Like Molecule α (RELM α), and Chitinase-like Molecules (CHIL3). Although STAT6 axis plays a crucial role in regulating transcription through IL-4, there are additional pathways and transcription factors that contribute to the activation of the M2 genes. Peroxisome proliferator-activated receptor gamma (PPAR γ), IRF4 or Kruppel-like factor 4 (KLF4) are examples of those¹⁸. M2 macrophages serve a dual function in tissue remodeling by both degrading and rebuilding the extracellular matrix. They express matrix metalloproteinases like collagenase for extracellular matrix degradation and produce fibronectin and Transforming Growth Factor-beta (TFG- β) to stimulate extracellular matrix reconstitution by fibroblasts. To support their role in tissue remodeling, M2

polarized macrophages have high phagocytic capacity, but are poor Antigen Presenting Cells (APCs) due to lower expression of MHCII and CD80/86¹⁹.

The M1 and M2 phenotypes exhibit cross-regulatory mechanisms to finely adjust the gene expression profile according to the specific environmental stimuli. Additionally, macrophages can adopt intermediate states to better perform necessary functions within a particular tissue. It is important to note that the activation state reached by macrophages is not irreversible; once polarized, macrophages can still be reprogrammed from one state to another. Importantly, macrophage activation involves changes in its metabolic responses, which can generate additional immunomodulatory effects.

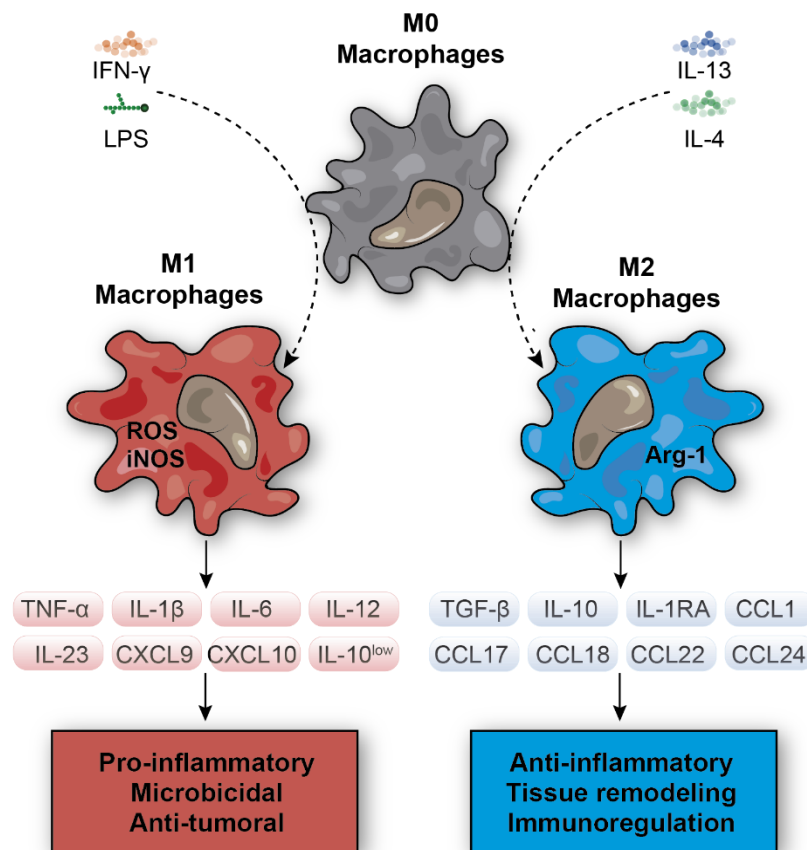


Figure 2: Canonical pro-inflammatory M1 polarization and anti-inflammatory M2 polarization of macrophages. The different stimuli, secreted cytokines, and biological functions between M1 and M2 macrophages were summarized. IFN: interferon, LPS: lipopolysaccharide, IL: interleukin, iNOS: inducible nitric oxide synthase, TNF: tumor necrosis factor, Arg1: arginase1, CCL: chemokine (C-C motif) ligand, CXCL: chemokine (C-X-C) ligand. Source: Self-elaborated.

2.3 Cytokines

Cytokines are low molecular weight proteins that play a crucial role in cell signaling and communication, particularly in the context of the immune system. They are secreted by various cell types, including immune cells like macrophages, lymphocytes, and dendritic cells, as well as non-immune cells such as endothelial cells and fibroblasts. Cytokines help regulate immune responses, inflammation, and haematopoiesis²⁰⁻²². These proteins act by binding to specific receptors on target cells, initiating a cascade of intracellular signaling events that ultimately modulate cellular functions, such as proliferation, differentiation, migration, and apoptosis. Cytokines can be classified into different groups, such as proinflammatory cytokines, which promote inflammation, and anti-inflammatory cytokines, which help to resolve inflammation and maintain tissue homeostasis.

IL-1, IL-6, and TNF- α are the main proinflammatory cytokines, and predominantly produced by macrophages. IL-1 and TNF- α cooperate at the inflammation site, stimulating the expression of proinflammatory enzymes such as cyclooxygenase, lipoxygenase (LOX), and iNOS, which are responsible for producing prostaglandins (PGs), leukotrienes (LTs), and NO, respectively. Furthermore, these cytokines serve as chemotactic agents and induce the expression of adhesion molecules like ICAM-1, VCAM-1, and E-selectin^{23,24}. IL-6 is a pleiotropic cytokine, acting as either pro- or anti-inflammatory cytokine depending on the context, and has a wide range of activities in immune regulation, hematopoiesis, inflammation, and oncogenesis^{25,26}.

IL-10 is an essential anti-inflammatory cytokine that plays a significant role in the regulation of the immune response, with macrophages being the main target cells through which IL-10 exerts its anti-inflammatory effects. In addition to dendritic cells and regulatory T lymphocytes, stimulated macrophages are capable of producing relatively high levels of IL-10. This suggests that IL-10 dampens inflammatory responses in an autocrine/paracrine manner^{27,28}. Upon binding to its receptors, IL-10 activates Janus kinases (JAKs). These kinases then facilitate the phosphorylation of STAT3, which subsequently migrates to the cell nucleus. Once inside the nucleus, STAT3 modulates the transcription of related genes, resulting in the suppression of

the expression of inflammatory cytokines such as IL-1, IL-6, and TNF- α ²⁹⁻³¹. Regulation of its expression is essential in order to maintain a balanced immune response; overproduction may enable immune evasion, while downregulation can contribute to tissue damage following infection.

2.4 Immunometabolism

It has been widely reported that the mitochondrial metabolic status is a major determinant of macrophages effector activities. The primary function of catabolic metabolism is to produce energy in the form of adenosine triphosphate (ATP) by breaking down organic matter, which is essential to sustain life. Research has shown that the regulation of metabolic processes, such as oxidative phosphorylation (OXPHOS) and aerobic glycolysis, not only maintain cellular homeostasis by providing energy (ATP) but it is also linked to immune function and responses to infection³². Activation of macrophages by classical or alternative pathways leads to significant changes in their metabolic profile, and metabolic dysregulation in macrophages is associated with functional impairment.

M1 polarization is associated with a dramatic shift in their energy metabolism from oxidative to glycolytic pathway upon activation. M1-activated macrophages by IFN- γ and LPS are characterized by a decrease in oxygen consumption rate (OCR) and an increase in extracellular acidification rate (ECAR)³³. This phenotype is analogous to the 'Warburg effect', a phenomenon observed by Otto Warburg in tumor cells at the beginning of the last century, which consisted of increased glycolytic flux and lactate production even in the presence of oxygen³⁴. Glycolysis serves as an efficient metabolic pathway to facilitate rapid ATP production, which is crucial for fulfilling the energy requirements of the immune response during acute infections. As a result, M1 macrophages upregulate glycolysis and the pentose phosphate pathway (PPP) while mitochondrial respiration decreases³⁵. It also allows Krebs cycle metabolites to act as signaling molecules and influence key inflammatory pathways. For example, citrate can be redirected away from the Krebs cycle and be involved in the synthesis of ROS, RNS and PGs^{36,37}.

In contrast to M1 macrophages, M2 macrophages carry out functions such as wound healing and tissue repair, which require a sustained energy supply that is met by high mitochondrial respiration. Alternative activation by IL-4 stimulation leads to a delayed, marginal upregulation of ECAR and an increase in OCR^{38,39}. M2 metabolic activity is characterized by an upregulation of fatty acid oxidation and oxidative metabolism. Prior research has demonstrated the importance of oxidative metabolism in maintaining the M2 phenotype, with inhibition of OXPHOS inducing M1 characteristics in M2 macrophages^{40,41}. The pentose phosphate pathway is also more limited in M2 macrophages³⁵. Glycolysis status in M2 macrophages is more controversial. Some studies suggest that glycolysis, although less dominant than in pro-inflammatory M1 macrophages, remains upregulated and is essential for M2 functionality^{42,43}. In contrast, others suggest that glycolytic activity is not required for M2 differentiation when OXPHOS remains intact⁴⁴. Data from Rodríguez-Prados *et al.* showed that alternative activation has minimal effects on glucose consumption, suggesting a down-regulation of glycolysis in M2 macrophages⁴¹. In addition to the established impact of metabolic pathways on macrophage function, recent research has further clarified the metabolic diversity of tissue macrophages in both humans and mice during homeostasis, identifying OXPHOS as the primary distinguishing feature among macrophages located in different organs⁴⁵. This highlights the intricate relationship between mitochondrial function and macrophage behavior in different tissue niches.

Amino acid metabolism is also relevant to the functional phenotype of macrophages. A hallmark of M1 macrophages is the elevated expression of iNOS which facilitates the synthesis of NO from arginine. NO serves as an important antimicrobial effector which also inhibits mitochondrial respiration⁴⁶. In contrast, M2 macrophages do not produce NO. Instead, they have high levels of Arg1, which catalyzes the conversion of arginine to polyamines, which are essential for collagen production, cellular proliferation, fibrosis, and tissue remodeling^{35,47-49}.

Although unique metabolic profiles can be easily recognized, the molecular mechanisms governing the regulation of macrophage polarization by different metabolic flux patterns remain poorly understood.

3. Mitochondria

Almost all metabolic pathways in the cell are linked and regulated by the mitochondria. The mitochondrion is an organelle which is ubiquitous in all eukaryotic organisms and is considered as the metabolic hub, frequently called “the powerhouse of the cell”, producing most of the cellular energy as ATP. In addition to their roles in cellular respiration and ATP synthesis, mitochondria play multiple essential roles in several biological processes. These include generating NADH and guanosine triphosphate (GTP) during the Krebs cycle, facilitating the synthesis of amino acids, heme groups, and iron-sulfur (Fe-S) clusters, as well as producing phospholipids necessary for membrane formation⁵⁰. Moreover, mitochondria are involved in calcium signaling, stress responses and apoptosis^{51–54}.

Structurally, mitochondria are organelles with a double membrane: the outer mitochondrial membrane that separates the intermembrane space from the cytosol, and the inner mitochondrial membrane (IMM) that separates the mitochondrial matrix from the intermembrane space (IMS). The outer and inner membranes of the mitochondria display distinct structural and functional characteristics⁵⁴. For example, the presence of porins in the outer membrane, proteins responsible for creating pores in the membrane, facilitate the passage of ions and small, uncharged particles through this membrane, making it permeant⁵⁵. In contrast, the IMM, which is folded into numerous ridges called cristae which considerably increase its total surface area, is highly selective, containing specialized protein complexes that regulate the transport of molecules and ions⁵⁶. This selective permeability is crucial for maintaining the electrochemical gradient across the IMM, which powers the production of ATP through OXPHOS. Additionally, the IMM hosts the mitochondrial respiratory chain, also known as the electron transport chain (ETC), a series of protein complexes that play a vital role in cellular respiration and energy generation.

The internal compartment enclosed by the IMM is the mitochondrial matrix, a specialized environment that plays a crucial role in the energy metabolism. The matrix is composed of a dense concentration of enzymes, solutes, and mitochondrial DNA. The mitochondrial matrix is the site where occurs the Krebs cycle. The matrix also contains enzymes responsible for fatty acid β -oxidation, which is the process by which fatty acids are broken down into acetyl-CoA molecules that can be further be processed in the Krebs cycle.

Another important function of the mitochondrial matrix is to store and maintain the organelle's own genetic material. Mitochondria contain their own DNA, which is circular and resembles that of bacteria. This unique genetic material is inherited maternally and encodes for 13 proteins essential for electron transport and ATP synthesis. The mitochondrial matrix also contains the machinery, such as ribosomes and tRNA molecules, necessary for translating mitochondrial transcripts into proteins⁵⁶.

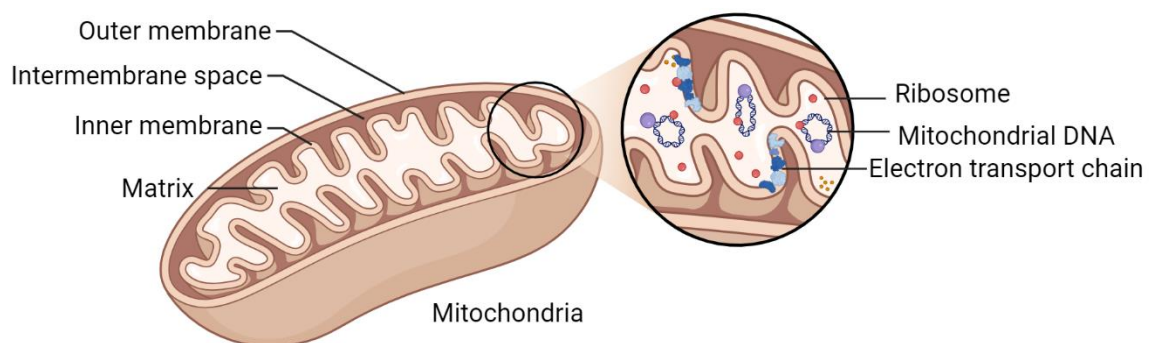


Figure 3: Scheme of mitochondrial structure. Source: Self-elaborated with BioRender.

3.1 Krebs cycle

The Krebs cycle, or citric acid cycle, is a sequence of chemical reactions that take place in the mitochondrial matrix as part of cellular respiration and play a central role in the metabolism of eukaryotic cells. It is also called the tricarboxylic acid cycle (TCA) cycle, because citric acid has three carboxyl groups in its structure. This cycle consists of a cyclic series of eight enzyme-catalyzed reactions that serves as a

bridge between glycolysis and the ETC, connecting carbohydrate, lipid, and protein metabolism pathways⁵⁷. The main function of the Krebs cycle is to capture, through carrier molecules, the electrons released from molecules during oxidation. These captured electrons produce high-energy molecules that initiate mitochondrial electron transport.

The Krebs cycle begins with the formation of citrate, a six-carbon compound, which results from the condensation of oxaloacetate and acetyl-CoA (derived from the metabolic breakdown of carbohydrates, fatty acids, and proteins). This reaction is catalyzed by the enzyme citrate synthase (CS). Subsequently, citrate is converted into isocitrate through the action of the enzyme aconitase. Isocitrate undergoes oxidation, resulting in the loss of one carbon atom and the formation of α -ketoglutarate, a five-carbon molecule. The enzyme responsible for this transformation is isocitrate dehydrogenase. Simultaneously, a molecule of CO_2 and a pair of electrons are released. The released electrons are captured by NAD^+ (oxidized nicotinamide adenine dinucleotide), converting it to NADH (reduced nicotinamide adenine dinucleotide), while the CO_2 diffuses out of the cell. The cycle advances with the oxidation of α -ketoglutarate by the enzyme α -ketoglutarate dehydrogenase, yielding succinyl-CoA, a four-carbon molecule, and releasing another molecule of CO_2 . The electrons produced are captured by another NAD^+ to form NADH. The fifth step involves succinyl-CoA synthetase, where succinyl-CoA transfers its CoA group to guanosine diphosphate (GDP), generating GTP. GTP can be subsequently converted into ATP by transferring its phosphate group to adenosine diphosphate (ADP). Succinyl-CoA is converted into succinate, a four-carbon compound. The enzyme succinate dehydrogenase, located in the IMM, catalyzes the following step, in which succinate loses two hydrogen atoms and becomes fumarate, a four-carbon molecule containing a trans double bond. The released electrons are captured by flavin adenine dinucleotide (FAD), leading to the formation of reduced flavin adenine dinucleotide (FADH₂). Fumarate then gains a water molecule, catalyzed by fumarase, and transforms into malate, a four-carbon molecule possessing a hydroxyl group. The final reaction in the cycle is the oxidation of malate to oxaloacetate by malate dehydrogenase. This process involves the loss

of two hydrogen atoms, resulting in the regeneration of oxaloacetate, a four-carbon molecule with two carboxyl groups, thereby replenishing the molecule utilized in the initial step and allowing the cycle to continue. The released electrons are captured by another NAD^+ to form NADH .

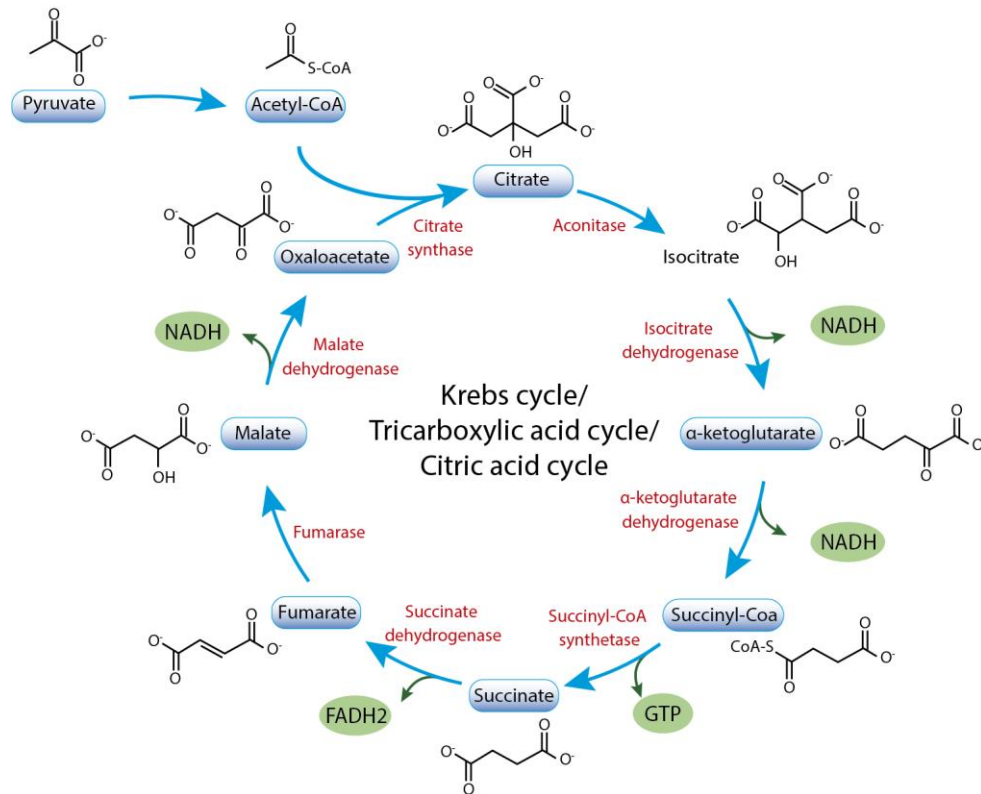


Figure 4: Illustration of the Krebs cycle or citric acid cycle or tricarboxylic acid cycle. Enzymes are in red. Source: Self-elaborated.

Altogether, one turn of cycle results in the release of two carbon dioxide molecules and the generation of three NADH , one FADH_2 , and one GTP . The NADH and FADH_2 that are formed in the cycle transfer their electrons to the ETC in the mitochondria that, by OXPHOS, leads to the production of ATP , the energy molecule that the cell uses to perform its functions. This cycle repeats twice for every glucose molecule that undergoes cellular respiration since there are two pyruvates produced through the process of glycolysis, leading to the formation of two acetyl-CoA per glucose.

3.2 Oxidative phosphorylation (OXPHOS)

The process of OXPHOS encompasses two components: the ETC comprising complexes I-IV, and ATP synthesis by ATP synthase, also named complex V (CV). This process involves the oxidation of reducing equivalents (NADH and FADH₂) coupled to ATP synthesis from ADP.

As previously described, molecules derived from the catabolism of glucose, fatty acids, and proteins are metabolized to produce acetyl-CoA as an energy-rich intermediate. Subsequently, the oxidation of acetyl-CoA in the Krebs cycle is coupled to the reduction of redox carriers NAD⁺ and FAD⁵⁸. The reduced carriers, NADH and FADH₂ transfer electrons to the ETC in the IMM, where enzymatic reactions catalyze their oxidation. The electrons are then shuttled to other complexes in the ETC by two mobile molecules: coenzyme Q or ubiquinone and cytochrome c. Ultimately, the process concludes with the reduction of oxygen, catalyzed by the binding of protons, resulting in the formation of water. The transfer of electrons is accompanied by the release of energy which is utilized by the complexes I, III and IV to pump protons across IMM. The pumping of protons from the mitochondrial matrix to the IMS establishes an electrochemical transmembrane gradient. This gradient consists of two components: a concentration gradient (ΔpH or pH difference) and an electrical gradient, specifically termed the mitochondrial membrane potential ($\Delta\text{p}\Psi$ or MMP)⁵⁹. Finally, CV utilizes this potential difference to effectively couple the diffusion of protons with the synthesis of ATP⁶⁰. The CV is divided into two functional units: F₀ and F₁. The F₀ unit is embedded in the IMM and is responsible for facilitating the movement of protons across the membrane. This proton translocation provides the energy needed for the F₁ unit, located in the matrix side of the membrane, to catalyze the conversion of ADP and P_i into ATP⁶¹.

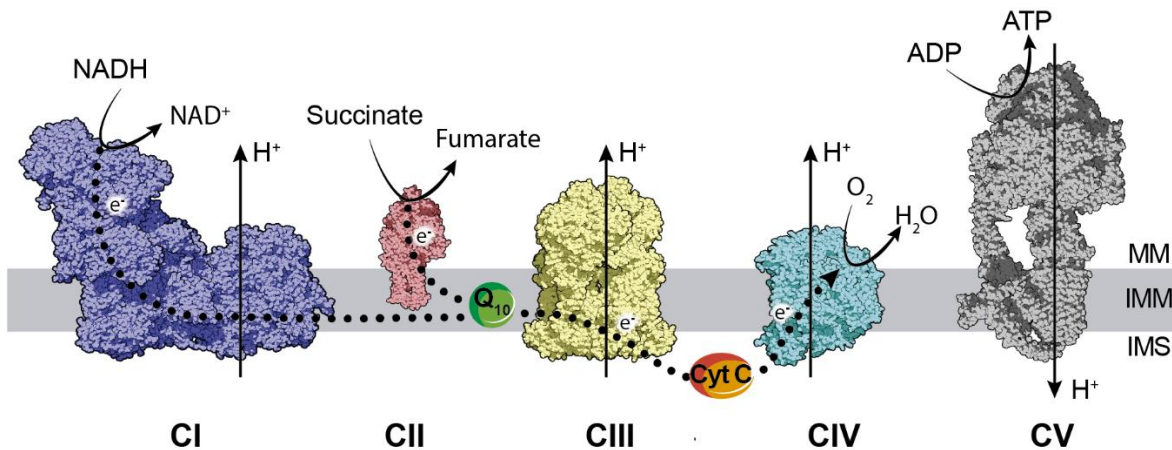


Figure 5: Schematic representation of the OXPHOS system. This diagram depicts the electron transport chain (ETC) complexes and ATP synthase (CV). It illustrates the proton (H⁺) pumping into the intermembrane space and the flow of electrons, denoted by the orange dotted line. Atomic models for each complex are provided with their Protein Data Bank (PDB) identifiers: CI (PDB 7V2C), CII (PDB 1ZOY), CIII (PDB 6FO2), CIV (PDB 5IY5), and CV (PDB 6TT7). Key molecules such as ubiquinone (Q₁₀) and cytochrome c (Cyt c) are also indicated. The grey rectangle demarcates the approximate boundary of the membrane. Labels for the mitochondrial matrix (MM), intermembrane space (IMS), and inner membrane (IMM) are included for spatial orientation. Source: Self-elaborated.

3.3 The electron transport chain (ETC)

The ETC consists in four large protein complexes (I-IV) embedded within the IMM, along with two mobile electron carriers, coenzyme Q (ubiquinone) and cytochrome c. Each complex contains multiple protein subunits and cofactors that assist in electron transfer.

Three complexes in the ETC, complexes I, III, and IV, are responsible for proton-pumping activity through different mechanisms. However, complex II (CII) does not participate in proton pumping; instead, it contributes to the reduction of ubiquinone, which serves as an electron source for complex III (CIII)⁶². Complexes I and II participate in electron donation to CIII through different substrates; complex I (CI) oxidizes NADH, whereas CII acts on succinate. The electrons are then accepted by CIII in the form of ubiquinol, the reduced form of ubiquinone. This ubiquinol is subsequently oxidized by CIII and the electrons are ultimately transferred to cytochrome c, which acts as an intermediary electron carrier, shuttling electrons to complex IV (CIV). CIV mediates the final reduction of oxygen to water.

Consequently, the resulting proton gradient is utilized by ATP synthase to convert ADP into ATP.

3.3.1 Complex I (CI)

With a total mass of about 1 MDa in mammals, CI is the respiratory chain's biggest component. It comprises a structure made up of 45 subunits and nine prosthetic groups. Thirty-seven subunits are encoded by the nuclear DNA, synthesized by cytoplasmic ribosomes, and imported into the mitochondria⁶³. The mitochondrial DNA encodes 7 integral membrane components, which are produced by mitochondrial ribosomes⁶⁴. This complex has a L-shaped structure with one arm attached to the IMM and the other arm projected into the matrix space^{65–67}. Based in the structure and functionality, CI can be subdivided in three modules called N-module, the Q-module, and the P-module.

The N-module is responsible for the binding and oxidation of NADH, converting it to NAD⁺. This reaction occurs as a hydride ion is transferred from NADH to the flavin mononucleotide (FMN) prosthetic group⁶⁸. The resulting reduced FMN then passes its electrons to a series of 7 Fe-S clusters⁶⁹. The Q-module handles the transfer of electrons from the Fe-S clusters to ubiquinone, which is bound at the Q-binding site, thus converting ubiquinone to ubiquinol⁷⁰. The P-module, or proton pumping module, is responsible for translocating protons from the matrix to the intermembrane space. The exact mechanism of proton pumping within the P-module remains a matter of debate. A proposed mechanism involves a series of electrostatically driven proton transfers from one subunit into the next, this process is referred to as the domino effect⁷¹.

Moreover, CI is an important producer of cellular ROS, which can be generated as a by-product of the electron transfer process. ROS is generated by reaction of O₂ with fully reduced FMN, regulated by the NADH/NAD⁺ ratio. Conditions like respiratory chain inhibition or low ATP demand elevate this ratio, leading to increased ROS formation. Importantly, CI generates large amounts of ROS during reverse electron transport (RET). RET is produced when electrons are forced back into CI due to a high MMP and an elevated ubiquinol pool⁷². Although ROS play an

important role in various cellular processes, excessive production of these species can lead to oxidative stress and the damage of cellular components^{73–75}.

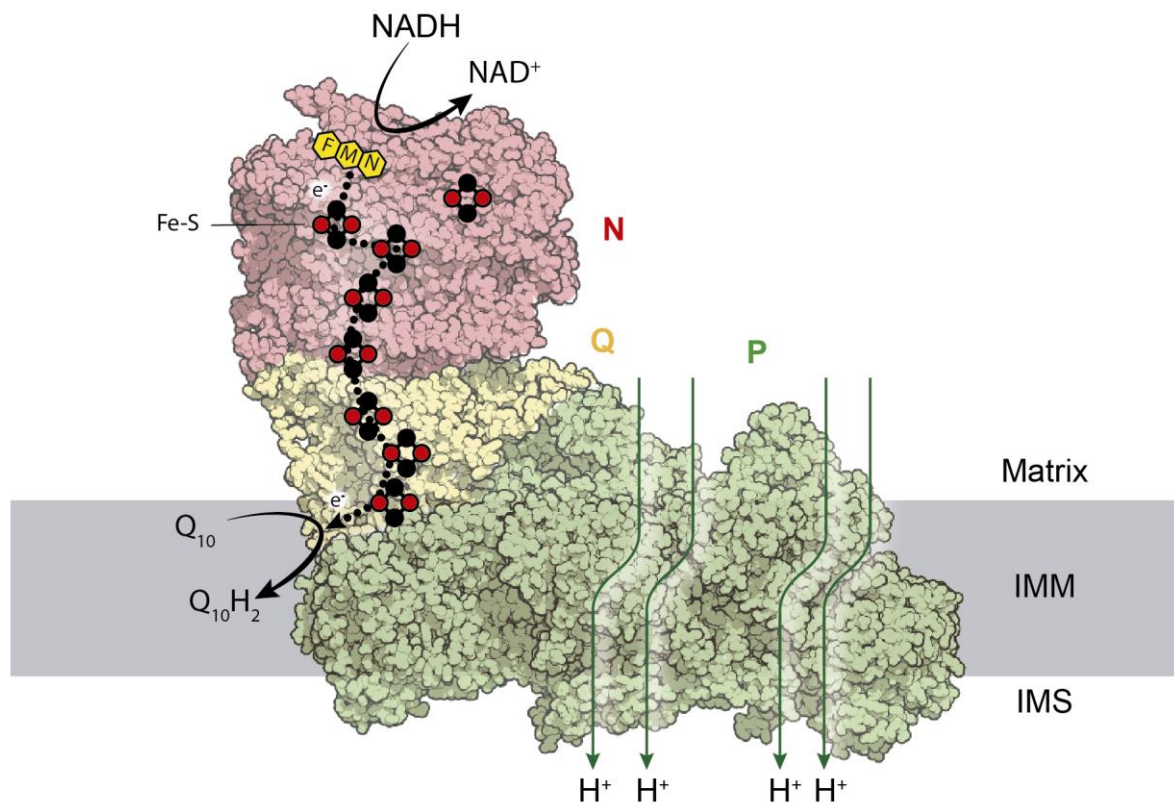


Figure 6: Overview of structures of complex I. The diagram of mammalian CI from *S. scrofa* (PDB 7V2C) highlights structural elements for enzymatic activity, including molecules: flavin mononucleotide (FMN), iron-sulfur clusters (Fe-S), ubiquinone (Q_{10}), and cytochrome c (Cyt c). An orange dotted line denotes the electron transfer pathway to Q_{10} . Functional modules within CI are color-coded: N module for NADH oxidation is in red, Q module for Q_{10} reduction is in yellow, and P module for proton pumping is in green. The grey rectangle marks the approximate boundary of the membrane, with annotations for the mitochondrial matrix (MM), intermembrane space (IMS), and inner membrane (IMM) included for spatial context. Source: Self-elaborated.

3.3.2 Complex II (CII)

CII, also known as succinate dehydrogenase (SDH), is the smallest complex in the respiratory chain, with a mass of approximately 140 kDa. CII is the only complex in the ETC that can directly contribute to the Krebs cycle. This unique ability of CII to perform dual functions in cellular respiration is due to its catalytic activity, which allows it to catalyze the conversion of succinate to fumarate in the citric acid cycle, while also assisting in electron transfer.

The structure of CII is composed of four subunits, SDHA, SDHB, SDHC, and SDHD, all of them encoded by the nuclear DNA, and contains several prosthetic groups. SDHA contains the catalytic site to oxidize succinate and has the FAD prosthetic group. This group accepts electrons from succinate during its oxidation to fumarate to form FADH₂. SDHB, on the other hand, contains three Fe-S clusters (2Fe-2S, 4Fe-4S, and 3Fe-4S). SDHC and SDHD, integral membrane components, anchor the complex to the IMM and hold the heme b group. The pocket formed by transmembrane helix I of SDHC, transmembrane helix II of SDHD and the C-terminal segment of SDHB contains the ubiquinone binding site. The released electrons from succinate oxidation are transferred to the [3Fe-4S] cluster through a chain of redox centers, including FAD, [2Fe-2S], and [4Fe-4S]. It is proposed that heme b acts as an electron sink in this pathway and complete reduction of ubiquinone occurs by accepting a pair of electrons, either from heme b or the [3Fe-4S] cluster⁷⁶. Although CII does not participate in proton translocation, its function is essential for the overall efficiency of OXPHOS by providing reduced ubiquinone to CIII.

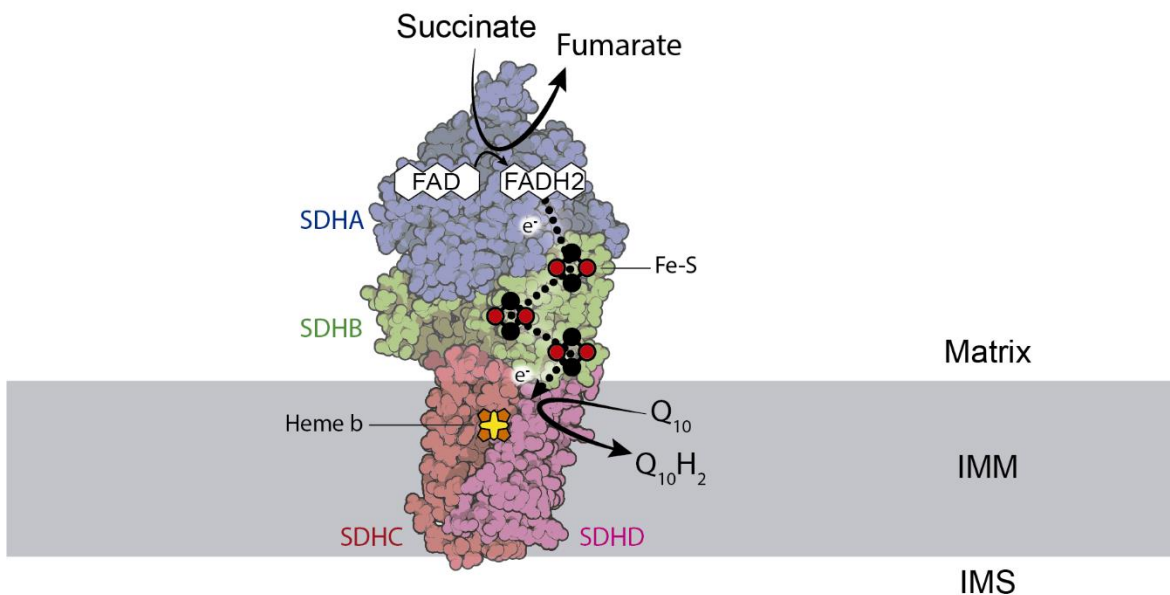


Figure 7: Overview of structures of complex II. The diagram of mammalian CII from *S. scrofa* (PDB 1ZOY) elucidates the structural components for enzymatic activity, highlighting molecules: flavin adenine dinucleotide (FAD), iron-sulfur clusters (Fe-S), and ubiquinone (Q₁₀). An orange dotted line marks the electron transfer pathway to Q₁₀. The four subunits within CII are color-coded for clarity: SDHA in blue, SDHB in green, SDHC in red, and SDHD in pink. A light grey rectangle outlines the approximate boundary of the mitochondrial

membrane, with labels provided for the mitochondrial matrix (MM), intermembrane space (IMS), and inner membrane (IMM) for spatial context. Source: Self-elaborated.

3.3.3 Complex III (CIII)

CIII, also known as cytochrome bc₁ complex or ubiquinol-cytochrome c oxidoreductase, is an essential component of the respiratory chain. It consists of 11 subunits and has a mass of approximately 240 kDa^{77,78}. CIII plays a key role in receiving electrons from both CI and CII through ubiquinol and transferring them to cytochrome c.

The CIII includes three catalytic structures: cytochrome b, Rieske iron-sulfur protein (ISP) and the cytochrome c₁. When ubiquinol interacts with CIII, it is oxidized to ubiquinone and transfers two protons to the intermembrane space, while the two released electrons follow the Q-cycle mechanism⁷⁹. One of the electrons is donated to the Rieske ISP, which contains a 2Fe-2S cluster. The Rieske ISP transfers the acquired electron to heme c₁ in the cytochrome c₁, which in turn transfers it to the soluble electron carrier cytochrome c⁸⁰. The other electron is transferred via two hemes b to the cytochrome b to partially reduce a different ubiquinone molecule, converting it to a ubisemiquinone radical. When another ubiquinol molecule undergoes the same process, the second electron from this molecule reduces the ubisemiquinone to ubiquinol, thus completing the cycle.

CIII also generates ROS during the electron transfer process^{81,82}. Although CIII may not produce ROS at levels comparable to CI during RET, its contribution to ROS generation may be physiologically relevant under certain conditions. For example, when mitochondria are actively synthesizing ATP, where ROS production from CI is relatively low, CIII role in ROS generating may become significant⁷². The ubisemiquinone radical intermediate can release electrons to molecular oxygen, leading to the production of ROS. Factors that affect the stability of this radical, such as changes in the MMP or the loss of cytochrome c, could modulate this ROS production.

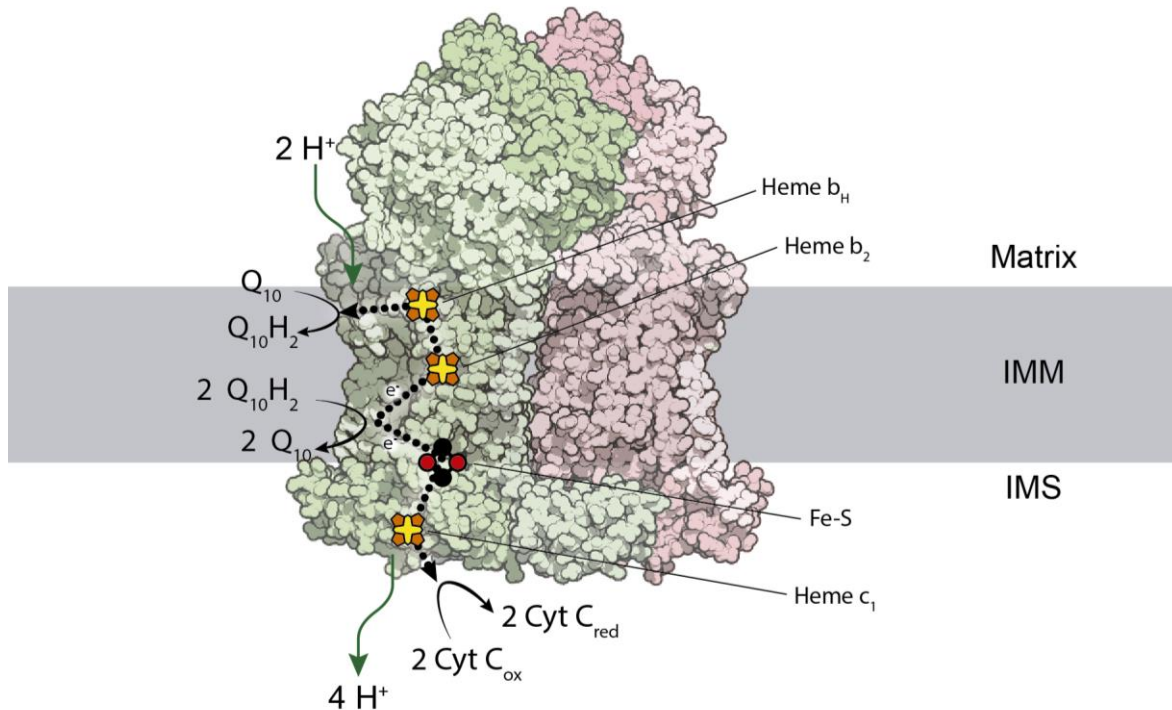


Figure 8: Overview of structures of complex III. The diagram of mammalian dimer CIII₂ from *B. taurus* (PDB 6FO2) detailed the structural elements for enzymatic functionality, highlighting key molecules: iron-sulfur clusters (Fe-S), cytochrome c (cyt c), heme groups, and ubiquinone (Q₁₀). An orange dotted line indicates the electron transfer pathway to Q₁₀. one protomer of the dimeric CIII is represented in green and the other in red. A light grey rectangle delineates the approximate boundary of the mitochondrial membrane. Annotations for the mitochondrial matrix (MM), intermembrane space (IMS), and inner membrane (IMM) are included to provide spatial context. Source: Self-elaborated.

3.3.4 Complex IV (CIV)

CIV, also known as cytochrome c oxidase (COX), is the terminal enzyme of the ETC and has a mass of approximately 200 kDa. It is composed of 13 subunits, with three of them being encoded by the mitochondrial DNA, while the remaining ten are nuclear-encoded^{83,84}. The primary function of CIV is to catalyze the transfer of electrons from reduced cytochrome c to molecular oxygen, resulting in the formation of water. This process is coupled with the translocation of protons across the IMM, contributing to the proton gradient required for ATP synthesis.

The structure of CIV comprises three main catalytic subunits: Subunit I, the largest subunit of CIV, encompasses two heme groups and two copper centers. These

prosthetic groups facilitate the crucial electron transfer reactions necessary for the reduction of oxygen to water. Subunit II, on the other hand, serves as the electron acceptor from the soluble carrier molecule, cytochrome c. It receives electrons from cytochrome c and transfers them to Subunit I. The third core subunit, Subunit III, contains three tightly bound phospholipids that have been proposed to regulate the uptake of oxygen and its subsequent transfer to the active site of the enzyme. These phospholipids likely participate in modulating the enzyme's activity, ensuring precise control over the oxygen reduction process^{85,86}.

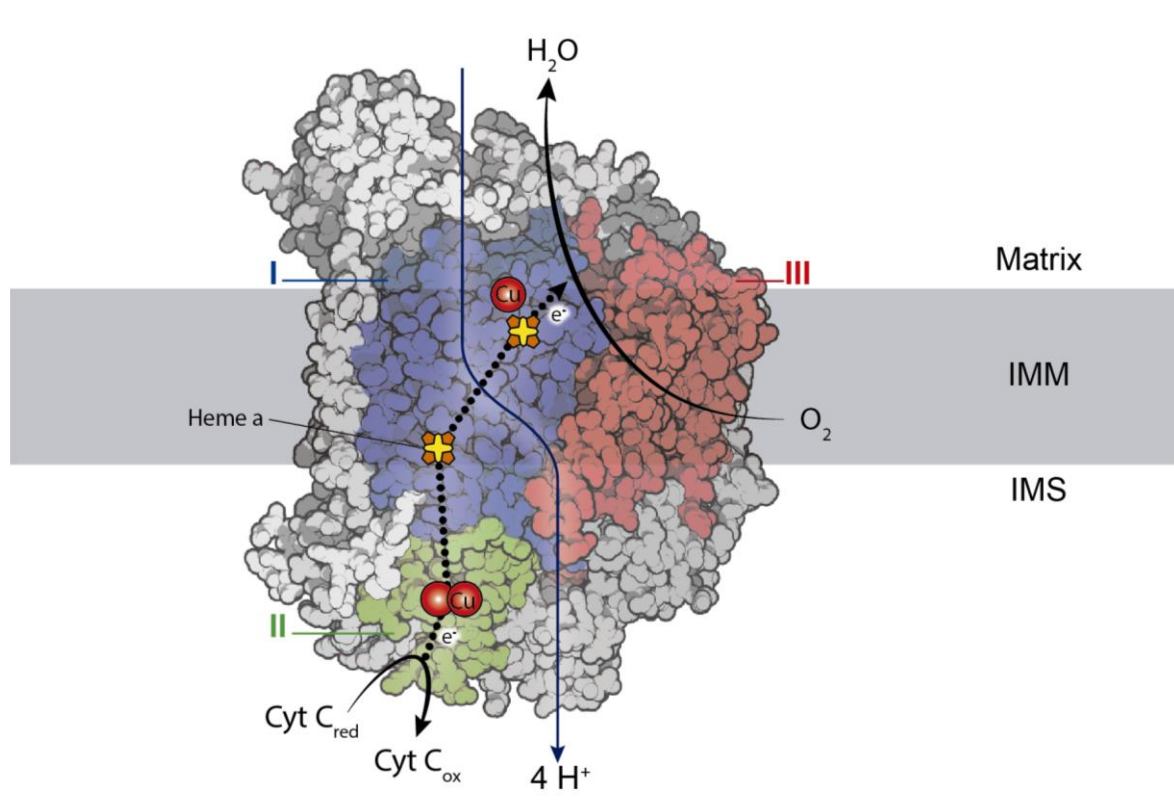


Figure 9: Overview of structures of complex IV. The diagram of mammalian CIV from *B. taurus* (PDB 5IY5) shows the structural components for enzymatic activity, including key molecules: heme groups, copper centers (Cu) and cytochrome c (cyt c). An orange dotted line signifies the electron transfer pathway leading to the final reduction of oxygen to water. The three main catalytic subunits are color-coded: Subunit I in blue, Subunit II in green, and Subunit III in red. A light grey rectangle outlines the approximate boundary of the mitochondrial membrane, and annotations for the mitochondrial matrix (MM), intermembrane space (IMS), and inner membrane (IMM) provide spatial context. Source: Self-elaborated.

3.3.5 Supercomplexes (SCs)

In addition to assembling into individual complexes, mitochondrial components have long been shown to assemble into SCs. These represent a higher level of structural organization within the ETC. Initially identified by blue-native gel electrophoresis (BN-PAGE) of detergent-solubilized inner mitochondrial membranes in mammalian cells, the structures of CI+CIII₂+CIV (often referred to as the respirasome), CI+CIII₂ and CIII₂+CIV have been further elucidated using cryo-electron microscopy (cryo-EM)^{87–91}.

The prevalence of individual complexes within the SCs varies from one complex to another. For example, the majority of CI is incorporated into the respirasome and CI+CIII₂ SCs. In contrast, CIV exists predominantly in the free state, either as a monomer or as a dimer. The discrepancy highlights the dynamic nature of SCs assembly and its potential tissue-specific adaptations. In astrocytes, CI is predominantly found as an isolated entity, whereas in neurons it is predominantly part of SCs⁹². Such differences in the distribution of SCs in different tissues suggest they are highly regulated by a context-dependent assembly mechanism, likely serving specific metabolic needs.

Although the existence and functional role of SCs is widely accepted in the scientific literature, the precise mechanisms by which they enhance mitochondrial function remain an active area of investigation. Several hypotheses have been proposed to explain their function. First, the formation of SCs is thought to confer protection against excessive ROS production^{92,93}. This is critical for maintaining cellular homeostasis and reducing oxidative stress. Second, SCs are suggested to regulate the activity of individual respiratory complexes, thereby coordinating the overall efficiency of the ETC^{94,95}. Other theories suggest that SCs formation enhance the structural integrity of individual respiratory complexes⁹⁶.

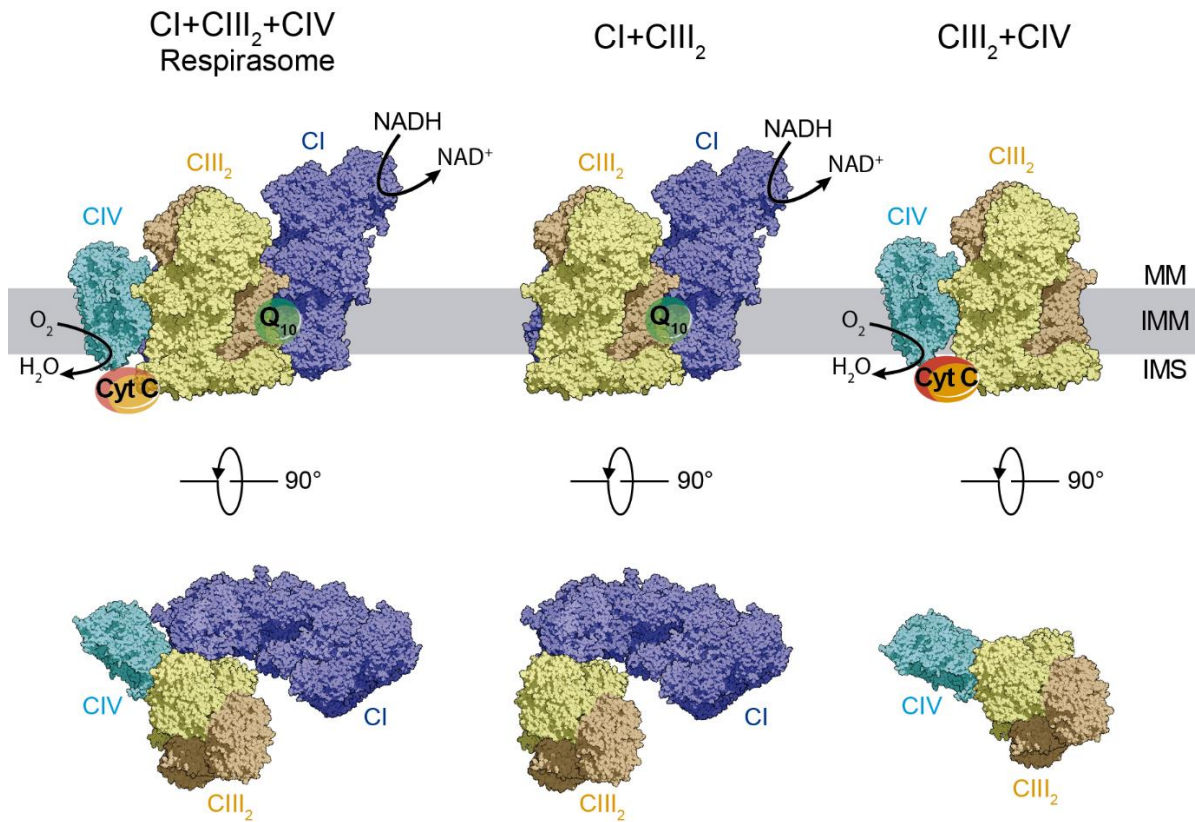


Figure 10: Overview of Respiratory Supercomplexes. Atomic models of the SCs in mammalian mitochondria: CI+CIII₂+CIV, CI+CIII₂ and CIII₂+CIV. Two views are shown: one from the side along the inner membrane and another from the top. Colored by constituent complex: CI in blue, CIII in yellow/orange, and CIV in cyan. A light grey rectangle indicates the approximate boundary of the mitochondrial membrane, and labels for the mitochondrial matrix (MM), intermembrane space (IMS), and inner membrane (IMM) provide spatial orientation. Source: Self-elaborated.

4. Role of mitochondrial complexes in macrophage polarization

The intricate relationship between mitochondria and macrophages has increasingly become a focus for understanding immune regulation⁹⁷. In particular, the differential expression and activity of mitochondrial complexes has significant consequences for metabolic rates, which in turn influence the production of ATP and other key metabolites that modulate macrophage polarization.

CI, known for its role in the generation of ROS via RET, acts as an important mediator in pro-inflammatory responses. Increased levels of ROS activate the expression of proinflammatory cytokines such as IL-1 β , a process mediated via HIF-

1 α ⁹⁸. Remarkably, reducing ROS with the antioxidant MitoQ or by pharmacological inhibition of CI with rotenone or metformin results in a decrease in pro-IL-1 β and an increase in the production of the anti-inflammatory cytokine IL-10⁹⁹. Indeed, these pharmacological interventions, particularly metformin, alleviate acute airway disease in non-diabetic mice by suppressing IL-1 β production, an effect likely due to a combined downregulation of HIF-1 α and NLRP3 inflammasome activity⁹⁸. In contrast, significant ROS production leading to systemic inflammation can also be induced by genetic ablation of the CI subunit Ndufs4¹⁰⁰, a widely used mouse model of CI deficiency and the neurodegenerative Leigh syndrome^{101,102}. Other studies have shown that certain compounds that inhibit mitochondrial CI, such as metformin, have a positive effect on the phagocytic capacity of neutrophils¹⁰³. Work by Garaude *et al.* further elucidates the role of CI, showing that after phagocytosis of live bacteria, macrophages undergo alterations in SCs assemblies containing CI, characterized by a downregulation of CI activity¹⁰⁴. However, this phenomenon is absent in LPS-activated bone marrow-derived macrophages (BMDM). Interestingly, the same study identified an increase in both the abundance and activity of CII in macrophages responding to live bacteria, but not to LPS or heat-killed bacteria.

Focusing on CII, this complex serves as a critical hub for succinate oxidation, which in turn drives RET and boosts mitochondrial ROS production by CI¹⁰⁵. Tannahill *et al.* have reported that succinate can also be transported from mitochondria to the cytosol where it directly inhibits the function of Prolyl Hydroxylase Domains (PHD) to stabilize HIF-1 α , leading to increased production of pro-IL-1 β and decreased IL-10 in LPS-stimulated BMDM¹⁰⁶. Further pharmacological studies using dimethyl malonate (DMM), a competitive inhibitor of Sdha, suggested that the ROS signal derived from succinate oxidation is required for IL-1 β induction. In addition to inhibiting LPS-induced IL-1 β , DMM also increased IL-10 levels in these cells¹⁰⁷. Furthermore, itaconate, a metabolite that is highly concentrated in M1 macrophages, acts as a competitive inhibitor of CII. This inhibition reduces RET-induced ROS production and decreases the secretion of pro-inflammatory cytokines such as IL-1 β ^{108,109}. Finally, it is important to highlight that activation of the tyrosine protein

kinase Fgr by ROS is essential for CII activation and subsequent IL-1 β production in proinflammatory macrophages¹¹⁰.

CIII, is another key site for the production of superoxide, with the particularity that it releases ROS not only into the mitochondrial matrix but also into the IMS, providing an easier route to the cytosol. This allows ROS to play a role in cellular signalling. CIII-generated ROS are also responsible for the destabilization of PHD and the activation of HIF-1 α ¹¹¹. Ahmed *et al.* showed that in macrophages, double-stranded RNA recognition by TLR3 is associated with increased CIII expression, which increases mitochondrial and cytosolic ROS to provide proinflammatory and antiviral cytokines¹¹². CIV is also involved in macrophage polarization although it does not generate ROS. shRNA-mediated knockdown of the IVi1 subunit in RAW 264.7 not only increases pro-inflammatory cytokines such as IL-1 β , IL-6 and TNF- α , but also the anti-inflammatory cytokine IL-10¹¹³.

In conclusion, the role of mitochondrial complexes in modulating macrophage function and polarization is both significant and diverse. Further research is needed to clarify some of the conflicting findings in this area and to elucidate the relative importance of different complexes in different states of polarization. Understanding the molecular mechanisms underlying the role of mitochondrial complexes in macrophage polarization may provide new insights into the pathophysiology of many diseases characterized by dysfunctional macrophage responses.



Hypothesis and Objectives



Hypothesis

Prior research has highlighted a significant impact of the functionality of mitochondrial respiratory complexes on the immune response in macrophages. Nonetheless, findings vary greatly across studies. It is suggested that this variability stems largely from the diverse methodologies and systems utilized. It is hypothesized that employing precise gene editing techniques, such as CRISPR/Cas9 HITI, within a single validated cell model could accurately determine the specific impact of deficiencies in various mitochondrial complexes on macrophage immune responses.

Objectives

The overall aim of this thesis is to explore in more detail the intricate connection between mitochondrial function and immune responses in macrophages, using advanced gene editing techniques to create precise cellular models. Through this exploration, the thesis aims to bridge the existing knowledge gap from previous studies and provide a more coherent understanding. By disrupting specific genes, *Ndufs4*, *Sdha* and *Sdhb*, the thesis aims to develop more homogeneous and rigorous cellular models that are deficient in the function of mitochondrial complexes that serve as the main pathways for electrons to enter the ETC, CI and CII. These genes encode critical subunits of CI and CII, and their deletion will allow a more precise study of how the absence of these components affects the immune response in macrophages.



The specific objectives of the work will be

- To use the CRISPR/Cas9 HITI targeted gene editing technique to generate RAW 264.7 macrophage lines KO in the key subunits involved in the activities of CI (Ndufs4) and CII (Sdha and Sdhb).
- To investigate the role of Ndufs4 in CI assembly and the impact on mitochondrial biochemistry and immune metabolism.
- To investigate effect of SDH/CII deficiency on the metabolic phenotype and effector functions of macrophages.
- To elucidate the pathways and molecular mechanisms that underlie the interplay between mitochondrial respiration and macrophage immune responses.



Material and Methods



Material and Methods

1. Cell Line and Culture Conditions:

1.1 Bone Marrow-Derived Macrophages (BMDMs) extraction and culture

BMDMs were obtained and cultured using the following procedure. C57BL/6 mice (8-12 weeks old) were euthanized following approved animal protocols. The femurs and tibias were aseptically dissected and carefully cleaned of adhering soft tissue. The bones were then flushed with Dulbecco's Modified Eagle Medium (DMEM) using a 25-gauge needle attached to a syringe. The bone marrow cells were collected in a sterile falcon tube and kept on ice. The collected bone marrow cells were centrifuged at 400 xg for 5 minutes, and the supernatant was discarded. The cell pellet was resuspended in DMEM supplemented with 10% fetal bovine serum (FBS), 1% non-essential amino acids (NEAA), 1 mM sodium pyruvate, 2 mM L-glutamine and 1% penicillin/streptomycin (referred to as complete DMEM in future references). To induce macrophage differentiation, filtered L929 cell supernatant, known to contain macrophage colony stimulating factor 1 (M-CSF), was added to the culture medium at a concentration of 10%. The cells were seeded in 100 mm cell culture dishes at a density of 2×10^6 cells/dish. The dishes were then placed in a humidified incubator at 37 °C with 5% CO₂.

The cells were cultured in this medium for 9 days to allow the macrophages to differentiate from the bone marrow precursor cells. The culture medium was replaced with fresh complete DMEM containing 10% L929 cell supernatant on days 5 and 7 of culture. On day 9, non-adherent cells were removed by gentle washing with phosphate-buffered saline (PBS). The adherent cells, representing the differentiated BMDMs, were detached using a cell scraper and transferred to new culture plates to be used for experimental procedures. BMDMs were cultured in complete DMEM.

1.2 RAW 264.7 murine macrophage cell line

The RAW 264.7 murine macrophage cell line (ATCC TIB-71), originally established from a tumor in a male mouse induced with the Abelson murine leukemia virus¹¹⁴, was maintained in complete DMEM. Cells were cultured in a humidified incubator at 37 °C with 5% CO₂.

For routine sub-culturing, the culture medium was removed from the culture plate or dish and washed twice with PBS. RAW 264.7 cells were detached from the culture flasks using 0.05% trypsin-EDTA solution for 10 minutes. Complete DMEM medium was then added to deactivate the trypsin. The resulting cell suspension was collected and centrifuged at 300 xg for 3 minutes, and the pellet was resuspended in fresh DMEM containing complete growth medium. The cell suspension was carefully mixed, and an appropriate volume was seeded into new culture flasks or plates at the desired cell density.

1.3 Generation of knock-out (KO) cell lines

1.3.1 Cas9-induced Homology-Independent Targeted Integration (HITI) strategy

The deletion of specific genes in the RAW 264.7 macrophage cell line was addressed using the Cas9-induced HITI strategy¹¹⁵.

The HITI technique is a type of genome editing that relies on the CRISPR-Cas9 system to allow targeted DNA integration without the need for the homology-directed repair (HDR) process. In contrast to traditional HDR-based approaches, which require a donor template with homologous arms to ensure precise DNA repair, HITI enables the direct integration of exogenous DNA sequences into the genomic DNA without requiring homology.

In HITI, the Cas9 nuclease is guided to the target sequence by a single-guide RNA (gRNA) to cleave the genomic DNA at the desired location. However, instead of relying on the cell's HDR machinery for repair, HITI utilizes non-homologous end joining (NHEJ) repair pathways to insert the exogenous DNA. NHEJ is an error-prone DNA repair mechanism that can create indels (insertions or deletions) during the DNA repair process.

The strategy involves designing and constructing specific targeting vectors. Typically, two types of plasmids, namely the targeting vector and the donor plasmid, are employed. The targeting vector carries the Cas9 enzyme and the gRNA sequences specific to the target site. On the other hand, the donor plasmid contains the desired exogenous DNA, which is also used as a selection marker gene, flanked by the gRNA target sequences. After Cas9-mediated cleavage, the exogenous DNA from the donor plasmid is then inserted into the genome via NHEJ repair. This results in integrating of the desired DNA sequence at the target locus, thereby leading to the knock-out (KO) of the target gene.

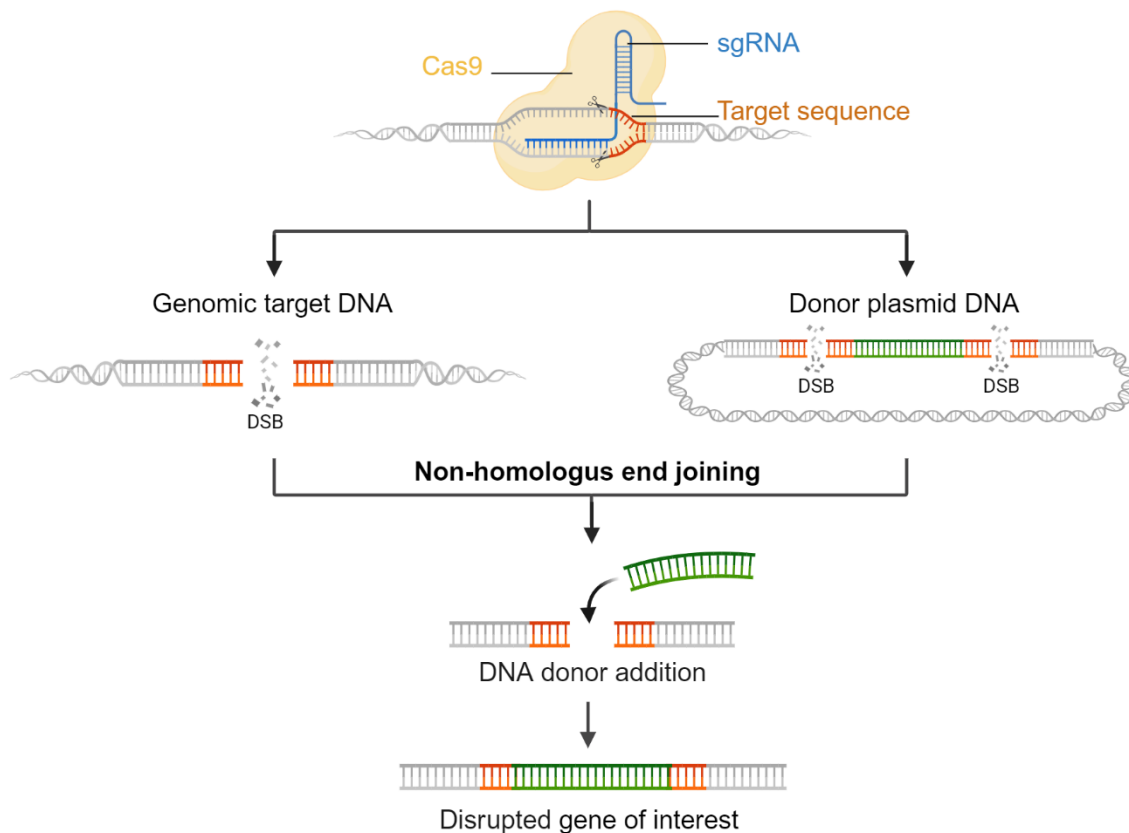


Figure 11: Homology-independent targeted integration (HITI). The gRNA of CRISPR induce double-strand breaks (DSB) at the target sequence in the genome and flanking the gene of interest in the donor plasmid. The donor DNA is then inserted into the genomic target site in either orientation by NHEJ. Source: Self-elaborated with BioRender.

1.3.2 Plasmid construction

Targeting vectors were designed to target either *Ndufs4* (CI subunit), *Sdha*, or *Sdhb* (CII subunits). The process of designing targeting vectors involved carefully selecting gRNA sequences to ensure specificity to the desired genomic location. gRNA sequences targeting exon 1 of these genes were designed using the CRISPOR tool, a bioinformatics tool that predicts off-target effects and the efficiency of the selected gRNA sequences. Forward and reverse oligonucleotides containing the guide sequences for either *Ndufs4* (CL1 and CL2), *Sdha* (CL3 and CL4) or *Sdhb* (CL5 and CL6) were annealed and cloned into the BbsI site of pX330-U6-Chimeric_BB-CBh-hSpCas9 plasmid, which generated three respective plasmids named pX330-gNdufs4, pX330-gSdha and pX330-gSdhb.

For producing HITI donor plasmids, forward and reverse primers were designed to contain the gRNA sequences for either *Ndufs4* (CL7 and CL8), *Sdha* (CL9 and CL10) or *Sdhb* (CL11 and CL12), along with the PAM sequence, stop codons (CL7, CL9 and CL11) and 21-22 nucleotides corresponding to the 5' (CL7, CL9 and CL11) and 3' (CL8, CL10 and CL12) flanking regions of the floxed blasticidin cassette of the pBS-Blast plasmid. pBS-Blast plasmid, is a pBluescript II-based plasmid, which contains a blasticidin resistance cassette flanked by loxP sequences previously generated in our laboratory. **Table 1** shows the sequences of the cloning primers CL1-12.

Polymerase chain reaction (PCR) amplification was done following the design of these primers, resulting in the generation of DNA fragments carrying the desired modifications. Subsequently, the PCR products were cloned into the BamHI and Sall sites of pBluescript II KS+ plasmid. The resulting donor plasmids were named pBLAST-gNdufs4, pBLAST-gSdha and pBLAST-gSdhb.

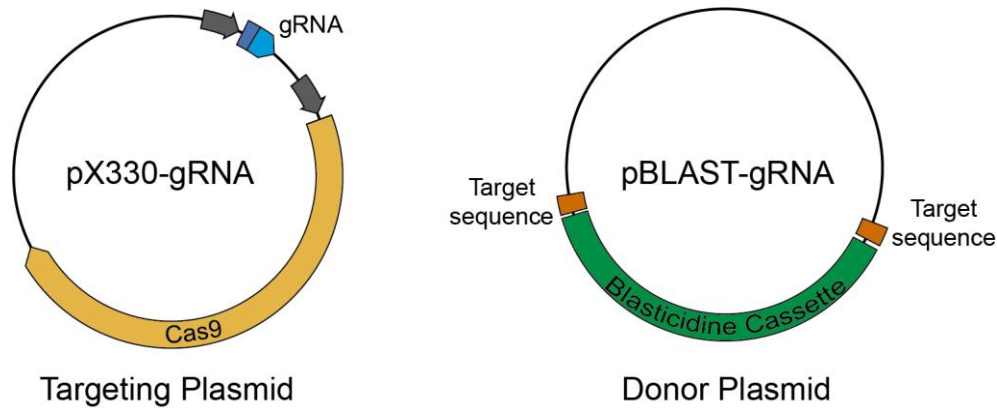


Figure 12: Scheme of the plasmids pX330-gRNA and pBLAST-gRNA used in the CRISPR/Cas9 HITI system. Source: Self-elaborated.

1.3.2.1 Preparation of *E. coli* DH10 β competent cells

Fresh streak of *E. coli* DH10 β cells was obtained by plating a frozen stock onto LB agar. The plate was incubated at 37 °C overnight. Then, a single colony from the freshly streaked plate was selected and inoculated into 5 mL of LB broth. The pre-culture was incubated at 37 °C overnight with gentle agitation. The entire pre-culture was transferred into a sterile Erlenmeyer flask which contained 100 mL of LB broth. The culture was incubated at 37 °C with gentle agitation until reaching an optical density (OD) of approximately 0.4 to 0.6 at 600 nm. The culture was then transferred to sterile centrifuge tubes and centrifuged at 2,500 xg for 5 minutes at 4 °C to pellet the cells.

The supernatant was removed carefully, and the cell pellet was gently resuspended in 30 mL of ice-cold sterile CMG buffer that contained 50 mM calcium chloride (CaCl₂), 50 mM magnesium chloride (MgCl₂). The suspension was incubated on ice 15 minutes and was then subjected to centrifugation at 2,500 xg for 5 minutes at 4 °C to pellet the cells. The supernatant was discarded, and the cell pellet was gently resuspended in 50 mL of ice-cold sterile 0.1 M CaCl₂ solution. The suspension was centrifuged again at 4,000 xg for 10 minutes at 4 °C. The supernatant was discarded and the cell pellet was carefully resuspended in 7.4 mL of ice-cold sterile CMG buffer. The cell suspension was mixed with 0.5 mL of dimethyl sulfoxide (DMSO) and transferred to sterile tubes in suitable aliquots. The tubes were immediately stored at -80 °C for long-term storage.

1.3.2.2 Transformation and amplification of plasmids

Constructed plasmids were amplified through heat shock transformation in competent *E. coli* DH10 β bacteria. A total of 10 μ L of the ligation reaction product was added to 50 μ L of competent *E. coli* DH10 β bacteria. This mixture was incubated on ice for 20 minutes, followed by a 45-seconds heat shock at 42 °C, after which it was incubated on ice for an additional 3 minutes. Next, 800 μ L of LB broth was added, and the bacterial suspension was incubated at 37 °C with shaking for an hour. The transformed bacteria were then pelleted through centrifugation at 10,000 xg for 2 minutes. The supernatant was then discarded while the bacterial pellet was resuspended in 100 μ L of LB medium. Subsequently, the transformed bacteria were plated onto LB agar plates supplemented with 100 μ g/mL of ampicillin. The plates were incubated at 37 °C overnight. The above procedure was also performed on ligation mixtures without inserts, which served as negative controls.

After selection of colonies from the transformed bacteria, a small-scale plasmid purification (miniprep) process was conducted to verify plasmid ligation. Isolated colonies were picked and inoculated into 3 mL of LB broth containing 100 μ g/mL of ampicillin at 37 °C with shaking, overnight. For plasmid DNA extraction, a 1.5 mL of the culture was utilized. The extraction was carried out utilizing the alkaline lysis method with commercial buffers P1, P2, and P3 (Qiagen). The culture was centrifuged at 10,000 xg for 5 minutes. The supernatant was then discarded, and the pellet was resuspended in 150 μ L of P1 resuspension buffer supplemented with 50 μ g/mL of RNase. Afterwards, 150 μ L of P2 lysis buffer was added, and the culture was incubated for 3 minutes. The reaction was terminated by adding 150 μ L of neutralization buffer P3. The plasmid DNA was precipitated by adding 900 μ L of absolute ethanol, followed by washing with 70% ethanol. Finally, the DNA was resuspended in TE buffer (10mM Tris-HCl, 1mM EDTA). Successful cloning was verified by PCR analysis. A compilation of primer sequences used for confirmation of successful cloning by PCR is shown in **Table 2**.

The medium-scale plasmid purification (midiprep) process utilized a PureLink HiPure Plasmid Midiprep kit to purify the plasmids from the transformed bacteria. The

transformed bacteria were grown in 100 mL LB broth containing 100 µg/mL of ampicillin at a temperature of 37 °C with shaking for 16 hours. For the Midiprep procedure, pelleted bacteria from the culture were resuspended in 4 mL of resuspension buffer, referred to as R3 buffer. Next, 4 mL of L7 buffer, the lysis buffer, were added, and the solutions were mixed by inversion, followed by a 5-minute incubation at room temperature. Finally, 4 mL of the neutralizing buffer, or N3 buffer, were added, and the vials were once again inverted to mix the solutions. The supernatant was transferred carefully to a silica column that had been pre-equilibrated with 10 mL of EQ1 buffer, an equilibrating buffer. After the liquid passed through the membrane, a column wash was performed using 10 mL of the wash buffer, W8 buffer. Next, the DNA was then eluted using 5 mL of E4 buffer, which is an elution buffer, and then precipitated by the addition of 3.5 mL of isopropanol. DNA was recovery by centrifugation at 3,200 xg for 30 minutes at 4 °C. The resulting precipitate was then washed with 70% ethanol. Finally, the DNA was resuspended in TE buffer, quantified, and stored at -20 °C for later use. The plasmids were sequenced to confirm the presence and correct orientation of the insert by employing a Sanger Sequencing Service offered by the Genomics Unit at the C.A.I. of Genomics and Proteomics at Complutense University of Madrid. The sequences of the primers used are shown in **Table 2**.

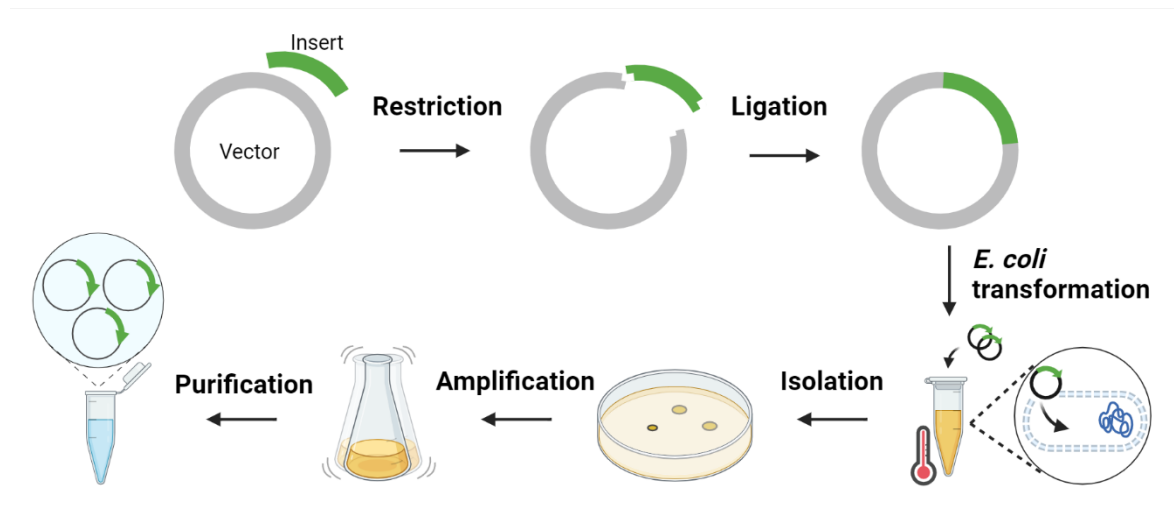


Figure 13: Diagram of plasmid production protocol. Source: Self-elaborated with BioRender.

1.3.3 Macrophages gene edition

1.3.3.1 Determination of blasticidin sensitivity

The minimum effective concentration of blasticidin required to eliminate non-transfected cells was determined for subsequent selection steps. Approximately 10,000 cells/mL were seeded into individual wells of a 96-well plate, using complete DMEM medium supplemented with varying concentrations of blasticidin (0, 1, 2, 3, 4, 5, 6, 7, 8 µg/mL). Each blasticidin concentration was tested in triplicate. The cells were incubated for 5 days at 37 °C in a humidified atmosphere containing 5% CO₂. During this period, regular microscopic observations were made on the treated cultures to assess the efficacy of blasticidin in eliminating cells.

1.3.3.2 Transfection of RAW 264.7 macrophages

RAW 264.7 cells at a density of 200,000 cells per well were cultured in a humidified atmosphere of 5% CO₂ at 37°C until reaching 90% confluence in a 24-well plate. After 24 hours, the culture medium was replaced with antibiotic-free complete DMEM.

The RAW 264.7 cells were then transfected with pX330 plasmids (pX330-gNdufs4, pX330-gSdha or pX330-gSdhb) and the corresponding HITI donor plasmids (pBLAST-gNdufs4, pBLAST-gSdha or pBLAST-gSdhb) at a molar ratio of 3:1. After a further 24 hours of incubation, the medium was replaced with complete DMEM. At 48 hours post-transfection, the medium was once again replaced with fresh complete DMEM supplemented with 2 µg/mL blasticidin to select for cells that had successfully integrated the blasticidin cassette into their genome.

Four days after transfection, the culture medium was removed and the cells were washed with PBS. The cells were then detached using trypsin-EDTA, collected in a tube and then centrifuged at 10,000 xg for 3 seconds. Next, the cell pellet was resuspended in 400 µL of complete DMEM medium. 50 µL of this cell suspension was taken to perform serial dilutions with the aim of obtaining single clones. The dilutions were distributed across 96-well plates with DMEM supplemented with 2 µg/mL blasticidin. The plates were incubated at 37 °C with 5% CO₂ for 15 days.

The wells were examined under a microscope to select those containing a single blastocidin-resistant colony. The culture medium was removed from the selected wells, and the cell colonies were washed with PBS. The cell clones were then detached using trypsin-EDTA and resuspended in 150 μ L of DMEM supplemented with 2 μ g/mL blastocidin and individually seeded into the wells of a 96-well plates. The plates were incubated at 37 °C with 5% CO₂ until a confluent growth of cells was achieved.

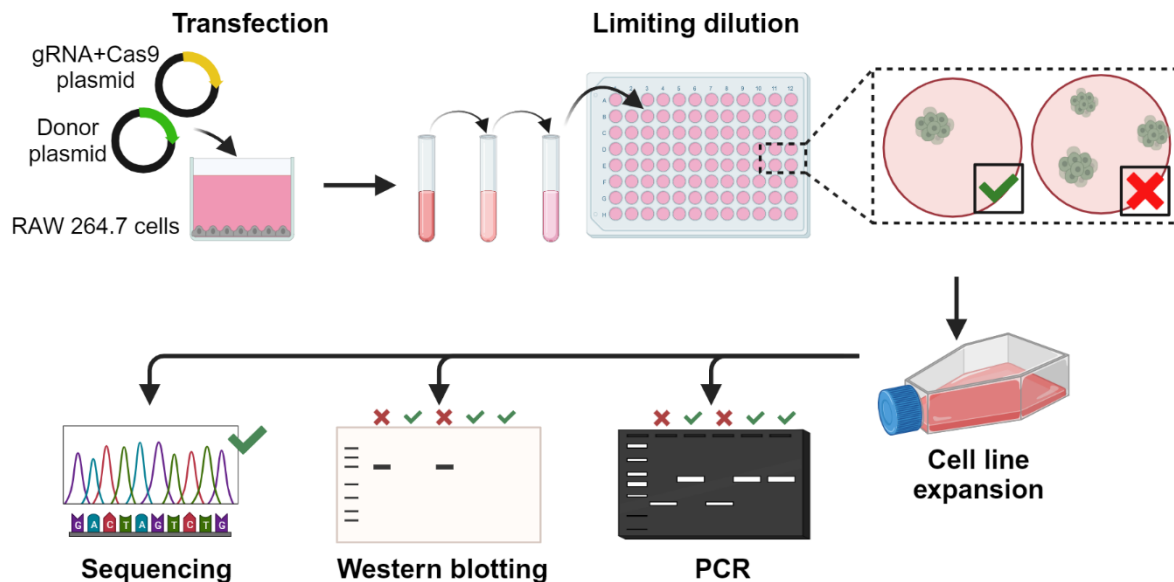


Figure 14: Knock-out cell line generation strategy. Source: Self-elaborated with BioRender.

1.3.4 Screening of gene editing

1.3.4.1 Genomic DNA extraction

The ethanol precipitation method was utilized to extract genomic DNA from RAW 264.7 cells. RAW 264.7 cells were cultured in 96-well plates until they reached approximately 90% confluency. The culture media was carefully aspirated, and the cells were resuspended in 200 μ L of lysis buffer (containing 50 mM Tris, 100 mM NaCl, 10 mM EDTA, 0.5% 2,6-Dichloroindophenol sodium salt hydrate (SDS) and 200 μ g/mL proteinase K). The cell lysate was then transferred to an Eppendorf tube and incubated at 55 °C for 1 hour. Next, 600 μ l of absolute ethanol, 20 μ l of 5M NaCl and 2 μ l of 20 mg/mL glycogen were added to the lysates. The mixture was gently

inverted several times to allow DNA precipitation. The tube was then placed at -20 °C for at least 30 minutes to facilitate DNA precipitation. Next, the sample was centrifuged at 12,000 xg for 15 minutes at 4 °C. Then, the supernatant was carefully discarded, and the DNA pellet was washed with 70% ethanol. The tube was inverted several times to wash the pellet thoroughly, followed by centrifugation at 12,000 xg for 10 minutes at 4 °C. The ethanol was carefully removed, and the DNA pellet was air-dried for approximately 15 minutes.

The dried DNA pellet was resuspended in 50 µL of TE buffer (10 mM Tris-HCl, 1 mM EDTA, pH 8.0). The resuspended DNA was incubated at 55 °C for 1 hour to ensure the pellet is completely dissolved. The spectrophotometer NanoDrop was used to verify the concentration and purity of the genomic DNA sample by measuring the absorbance at 260 nm and 280 nm. The DNA sample was then stored at -20 °C for later use.

1.3.4.2 PCR analysis

PCR analysis was conducted to confirm if gene editing and donor blasticidin cassette insertion occurred at the desired site. Specific primer sets were designed, surrounding regions adjacent to the gRNA recognition site in the genome (**refer to Table 2**). Different combinations of these primers were utilized to confirm successful gene editing at the locus of interest. PCR reactions were performed under the following conditions: 30-50 ng of genomic DNA, 0.2 mM of dNTPs, 1 unit of Phusion™ Hot Start II DNA polymerase, 1x HF Buffer, and 0.4 µM of each oligonucleotide primer. The thermal cycling program consisted of an initial denaturation step of 4 minutes at 98°C, followed by 40 cycles of denaturation for 10 seconds at 98°C, annealing for 20 seconds at 63°C, 45 seconds of extension at 72°C, and a final extension of 5 minutes at 72°C. The PCR products were visualized through electrophoresis on a 1% agarose gel.

The resulting PCR amplification products were examined to assess the presence of the expected DNA fragments compatible with successful gene editing events. In particular, the detection of suitably sized amplicons confirmed the gene modification, as well as the insertion of the blasticidin cassette at the target site.

2. Assay for cell proliferation

For the cell proliferation assay, parental Raw 264.7 and edited cells were seeded at a density of 1×10^5 cells/well in 6-well plates. At the indicated time points, cells were detached using trypsin-EDTA solution, resuspended in complete medium, and gently pipetted to obtain a single cell suspension. Cell counting was carried out using a Neubauer chamber under a light microscope considering only viable, non-clumping cells. Each sample was counted at least three times to ensure accuracy. Data obtained were used to calculate the rate of cell proliferation rate. To compute the proliferation index, the total cell number at each time point was divided by the initial seeding density.

3. Gene expression analysis

3.1 RNA extraction with TRIzol

Total RNA was extracted with TRIzol reagent (guanidine thiocyanate and phenol solution) following manufacturer's protocol. Macrophages were either activated with LPS or left unstimulated for 4 hours. The culture medium was removed from the culture plate, followed by the addition of 300 μ L of TRIzol reagent per 3×10^5 cells. The lysates were homogenized by gentle pipetting and transferred to 1.5mL Eppendorf.

After homogenization, chloroform was added to the TRIzol homogenate in a 1:5 (v/v) ratio. The mixture was shaken vigorously for 15 seconds and then incubated at room temperature for 3-5 minutes to enable phase separation. The sample was then centrifuged at 12,000 xg for 10 minutes at 4 °C. As a result, mixture separated into a lower red organic phase (containing lipids and proteins), an interphase (containing DNA), and an upper colorless aqueous phase (containing RNA).

The RNA-containing aqueous phase was carefully transferred to a new tube. Isopropanol was added to the aqueous phase in a 1:1 (v/v) ratio, and the mixture was gently inverted multiple times to facilitate RNA precipitation. The RNA was allowed to precipitate by incubating the sample at room temperature for 10 minutes.

Following this step, RNA was pelleted through centrifugation at 12,000 xg for 10 minutes at 4°C.

The RNA pellet was washed with 70% ethanol to remove residual salts and contaminants. After centrifugation at 7,500 xg for 5 minutes, the ethanol was carefully removed, and the RNA pellet was air dried at room temperature. The dried RNA pellet was resuspended in RNase-free water. The concentration and purity of the extracted RNA were determined using a NanoDrop spectrophotometer by measuring its absorbance at 260 nm.

3.2 Complementary DNA (cDNA) generation - Reverse Transcription PCR (RT-PCR)

cDNA was generated from the extracted RNA by performing a RT-PCR using the First-Strand Synthesis System kit. The reaction mixture for cDNA generation contained 3 µg of total RNA, random hexamer primers (5 µM), dNTP mix (1 mM each), 1X reverse transcriptase buffer, RiboLock RNase inhibitor (20 U), and M-Mul-V Reverse Transcriptase enzyme (40 U) supplied in the cDNA synthesis kit. The reaction mixture was gently mixed, then briefly centrifuged for homogeneity. The RT-PCR was conducted in a thermal cycler under the following conditions: an initial incubation at 25 °C for 5 minutes, followed by an incubation at 42 °C for 60 minutes. The reaction was terminated by heating at 70 °C for 5 minutes. The synthesized cDNA was diluted at a ratio of 1:10 in TE and was either used immediately or stored at -20 °C for later use.

3.3 Quantitative PCR (q-PCR)

The cDNA was used for q-PCR analysis. Amplification reactions were conducted using PowerUp SYBR Green PCR master mix and specific primer pairs for the genes of interest or housekeeping gene (Hprt1). The reaction mix included 5 µL of the previously diluted cDNA, 10 µL of 2X SYBR Green supermix, 1 µL of each forward and reverse primer (10 µM), and nuclease-free water up to a final volume of 20 µL. Reactions were performed in triplicate to ensure accuracy. The sequences of the primers used are shown in **Table 3**.

The q-PCR program was run on a thermal cycler under the following conditions: an initial denaturation at 95 °C for 10 minutes, followed by 45 cycles of denaturation at 95 °C for 15 seconds, annealing at 60 °C for 30 seconds, and extension at 72 °C for 45 seconds. After performing an additional step of 72 °C for 5 minutes for final extension, the melting curve analysis was conducted at 95 °C for 15 seconds, 60 °C for 1 minute, and 95 °C for 15 seconds to confirm the specificity of the amplification products.

Data analysis was carried out using the comparative C(T) method (also referred to as the $2^{-\Delta\Delta CT}$ method), with the Hprt1 gene serving as the normalization control. Gene expression was calculated as relative fold increase compared to the untreated parental cells.

4. Total protein extraction and Western blot analysis

To analyze protein levels, cells were lysed in RIPA buffer (50 mM Tris HCl, 150 mM NaCl, 1% NP-40, 0.5% sodium deoxycholate, 1 mM EDTA, 0.1% (w/v) SDS and 0.01% sodium azide at a pH of 7.4) supplemented with proteases and phosphatase inhibitors. Following a 30-minute incubation on ice, the lysates were centrifuged at 14,000 xg for 15 minutes at 4 °C. The resulting supernatant (protein extract) was subsequently collected and the protein concentration was determined using Pierce™ Detergent Compatible Bradford Assay Reagent according to the manufacturer's instructions. For the measurement, standard bovine serum albumin (BSA) solutions of known concentrations were used as standards and the absorbance was measured at 595 nm using a VersaMax microplate reader.

Equal amounts of protein (20-40 µg) were mixed with Laemmli buffer, then loaded into wells of an SDS-PAGE gel, typically 10% or 12% acrylamide, followed by electrophoretic separation of proteins based on their molecular weights. Electrophoretic separation was performed by applying a constant potential difference of 120 V using the PowerPac power source. The separated proteins were then transferred to a polyvinylidene difluoride (PVDF) membrane previously activated by a short rinse (1 minute) in methanol. The membrane was blocked with 5% non-fat dry milk or BSA in Tris-Buffered Saline with Tween 20 (TBS-T) for 1 hour

at room temperature to prevent non-specific binding. After blocking, the membrane was incubated with primary antibodies specific to the target proteins overnight at 4 °C. The membrane was then washed three times with TBS-T and incubated with horseradish peroxidase (HRP)-conjugated secondary antibodies for 1 hour at room temperature. Primary and secondary antibodies were diluted as indicated by the manufacturer, typically in 5% milk or BSA in TBS-T.

After secondary antibody incubation, the membranes were washed again three times with TBS-T and the protein bands were visualized using an enhanced chemiluminescent (ECL) detection system. Following this, blots were exposed to autoradiography films and developed in a darkroom. The Bio-Rad GS-800 densitometer was used to scan signals and the intensity of the protein bands was quantified using ImageJ software. The results were normalized to the loading control (β -actin) and to the untreated parental cells condition. A compilation of primary and secondary antibodies used is shown in **Table 4**.

5. Mitochondrial protein studies

5.1 Purification of mitochondria-enriched protein fractions

Cell pellets were resuspended in isotonic buffer comprising 250 mM sucrose, 20 mM Tris-HCl (pH 7.8), 0.2 mM EDTA, and 0.1 mM phenylmethylsulfonyl fluoride (sucrose-PMSF buffer). Homogenization was performed on ice, followed by a preliminary centrifugation step at 800 xg for 10 minutes to remove broken cells and debris. The resultant supernatant, containing a mixture of cytoplasmic, membrane, and mitochondrial components, was subjected to another round of centrifugation at 20,000 xg for 10 minutes. The pelleted mitochondria-enriched fraction was resuspended in sucrose-PMSF buffer and centrifuged again under the same conditions. Finally, the mitochondrial pellet was reconstituted in approximately 200-500 μ L of a buffer containing 10 mM HEPES (pH 7.6) and 0.5 M sucrose. The protein concentration in this fraction was determined using the Pierce MicroBCA protein assay kit.

5.2 Blue-Native polyacrylamide gel electrophoresis (BN-PAGE)

The purified mitochondrial fractions were resuspended in 100 to 200 μ L of a buffer containing 1.5 M aminocaproic acid and 50 mM Bis-Tris at pH 7.0. Solubilization was carried out using digitonin at a detergent:protein ratio of 4:1, and the samples were incubated on ice for 15 minutes. Post-incubation, samples were centrifuged at 20,000 \times g for 30 minutes at 4 $^{\circ}$ C, and the resulting supernatant was combined with 10 to 20 μ L of sample buffer (750 mM aminocaproic acid, 50 mM Bis-Tris, 0.5 mM EDTA, and 5% Coomassie Brilliant Blue G-250). A 3-12% Bis-Tris mini protein gel was loaded with 30-40 μ g of the mitochondrial protein, and the gel was run following established protocols. Subsequent to electrophoresis, proteins were transferred to PVDF membranes.

5.3 CI In-Gel Activity assay (IGA)

A Blue Native gel was utilized for the CI IGA. For this assay, the gel was incubated at room temperature in a solution containing 2 mM Tris-HCl (pH 7.4), 0.1 mg/mL NADH (serving as the substrate), and 2.5 mg/mL nitro blue tetrazolium (NBT, acting as the electron acceptor). NBT undergoes reduction to formazan by CI and consequently forms purple precipitates at the site of CI-containing respiratory SCs. Images representing the enzymatic activity were captured post 180 minutes of incubation in the IGA solution.

6. Detection of mitochondrial ROS

Cells under standard culture conditions were washed with PBS and detached from the plates using trypsin-EDTA. Next, cells were washed again twice with warm PBS and then incubated in phenol red-free DMEM. The cell suspension was adjusted to a concentration of 1×10^6 cells/mL in phenol red-free DMEM and aliquots were transferred to appropriate flow cytometry tubes. In some instances, cells were treated with 100 ng/mL LPS for 15 minutes at 37 $^{\circ}$ C. Untreated control groups were included for comparison.

For the detection of mitochondrial ROS (mitoROS), MitoSOX Red Mitochondrial Superoxide Indicator was used. MitoSOX Red reagent is live-cell-permeant dye

which selectively targets mitochondria. Once inside the mitochondria, MitoSOX Red reagent is oxidized by superoxide, a type of ROS produced within the mitochondria, and exhibits red fluorescence. It allows the specific detection of mitoROS by flow cytometry. MitoSOX was added to each tube at a final concentration of 1.75 μM and the tubes were gently vortexed to ensure proper mixing. The cells were then incubated for 15 minutes at 37 °C in the dark. Following the incubation process, the MitoSOX fluorescence was immediately measured using a Gallios flow cytometer. The resulting data from the flow cytometry was then analyzed using KALUZA software.

7. Measurement of Mitochondrial Membrane Potential (MMP)

To evaluate the mitochondrial mass and MMP, two fluorescent dyes, namely MitoView Green and MitoTracker Red CMXRos, were used. MitoView Green dye becomes fluorescent upon partitioning into the mitochondrial membrane and the intensity of staining is proportional to the mitochondrial mass, regardless of their MMP. On the other hand, MitoTracker Red dye incorporates into the mitochondrial matrix depending on the MMP.

RAW 264.7 macrophages were cultured in six-well plates overnight at 2×10^6 cells/well. The cells were then washed with PBS and detached using trypsin-EDTA. Cells were subsequently washed twice with warm PBS. Then, cells were resuspended in phenol red-free DMEM and the suspension was adjusted to a final concentration of 1×10^6 cells/mL. This suspension was divided into aliquots and transferred to flow cytometry tubes.

The MitoTracker Red CMXRos and MitoView Green dyes were prepared following the manufacturer's guidelines. Resuspended cells were incubated for 15 minutes at 37 °C in a 5% CO₂ atmosphere with the medium containing the dyes at a final concentration of 50 nM for MitoTracker Red and 75 nM for MitoView Green. When indicated, cells were treated with 100 ng/mL LPS for 15 minutes at 37 °C previous dye addition.

Post-incubation, cells were immediately examined by flow cytometry using a Gallios flow cytometer. Flow cytometry data were analyzed using KALUZA software. The fluorescence intensity of MitoView Green was used as a measure of mitochondrial mass, while the fluorescence intensity of MitoTracker Red indicated the MMP.

8. Phagocytosis assay in RAW 264.7 macrophages

The methodology used for the phagocytosis assay in RAW 264.7 macrophages using flow cytometry involves the use of fluorescein isothiocyanate (FITC)-labelled heat-killed *E. coli* (HKEC) as a model phagocytic target.

8.1 Labelling of bacteria

E. coli DH5 α was cultured overnight in LB broth at 37 °C in a shaking incubator. The bacterial culture was then centrifuged, and the cell pellet was resuspended in sterile PBS. The bacteria were heat-killed at 85 °C for 10 minutes. To label with FITC, HKEC was incubated with 0.4 mg/mL of FITC in PBS for 30 minutes at 37 °C in the dark. The bacteria were then washed three times with PBS to remove any unbound FITC.

8.2 Phagocytosis assay

RAW 264.7 cells under standard culture conditions were washed with PBS and detached from the culture plates using trypsin-EDTA. The cells were washed with warm PBS and then incubated in antibiotic-free DMEM. The cell suspension was adjusted to a concentration of 1×10^6 cells/mL in phenol red-free DMEM and aliquots of the cell suspension were transferred to appropriate flow cytometry tubes. Then, cells were incubated with FITC-labelled *E. coli* at a multiplicity of infection (MOI) of 100 for 15 minutes at 37 °C to allow phagocytosis.

8.3 Flow cytometry analysis

After the incubation, the cells were washed with cold PBS to remove any uninternalized bacteria. To quench the fluorescence of extracellular FITC-labelled *E. coli*, the cells were washed with a 0.1% Trypan Blue solution in PBS for 1 minute, as Trypan Blue is effective in quenching extracellular but not intracellular FITC

fluorescence. Finally, the cells were fixed with 4% paraformaldehyde in PBS for 15 minutes at room temperature, and subsequently washed with PBS.

The efficiency of phagocytosis was measured by quantifying FITC fluorescence in the cells, using a Gallios flow cytometer. Data were analyzed with Kaluza software. The percentage of FITC-positive cells was determined, representing the percentage of cells that have undergone phagocytosis.

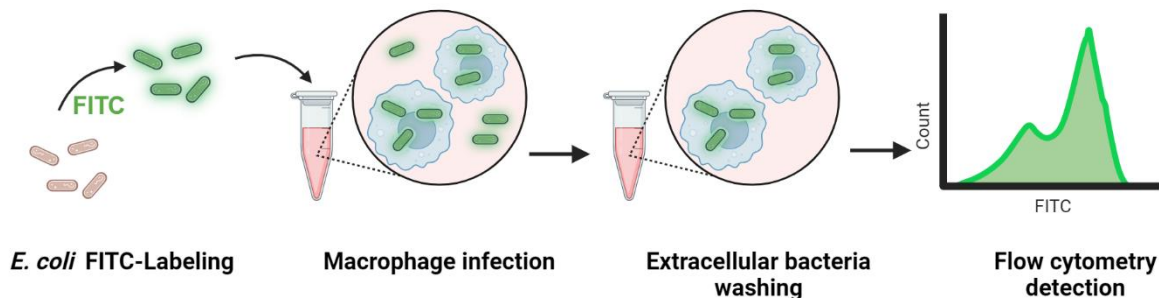


Figure 15: Representative scheme of phagocytosis assay protocol. Source: Self-elaborated with BioRender.

9. Gentamicin protection assay

The gentamicin protection assay is a standard technique used to measure the ability of invasion and survival of bacteria in the host cells, thereby inferring the bactericidal capacity of the cell. In this case, *E. coli* within RAW 264.7 macrophages.

9.1 Bacteria culture

E. coli was cultivated overnight in LB broth at 37 °C under shaking conditions. Bacterial concentration was determined by measuring the OD at 600 nm. The bacterial culture was then centrifuged, washed with PBS and resuspended in sterile antibiotic-free DMEM media.

9.2 Infection of RAW 264.7 cells with *E. coli*

RAW 264.7 cells were seeded at a density of 2×10^6 cells/well in 6-well plates and were allowed to adhere overnight under standard cell culture conditions. On the following day, the cells were washed twice with PBS, and the medium was replaced

with antibiotic-free DMEM. Then, cells were infected with *E. coli* at a MOI of 100 and incubated for 15 minutes at 37 °C to allow bacterial internalization.

After the infection period, the medium was aspirated, and cells were washed twice with warm PBS to remove extracellular bacteria. The cells were then incubated in DMEM containing gentamicin (100 µg/mL) for 15 minutes. Gentamicin is an antibiotic capable of killing extracellular bacteria but unable to penetrate mammalian cells.

Following the gentamicin treatment, the cells were washed with PBS and lysed with sterile deionized water for 5 minutes to release the intracellular bacteria. The lysates were collected and serially diluted in sterile deionized water.

9.3 Quantification of intracellular bacteria

After the cells had been lysed and the lysates had been serially diluted, the number of intracellular bacteria was measured using the drop plate method. Four 10 µL droplets were gently pipetted onto the surface of a LB agar plate for each serial dilution. The droplets were spaced apart to avoid merging. The plates were then left undisturbed at room temperature for approximately 15 minutes, allowing the droplets to absorb into the agar. Finally, the plates were incubated at 37 °C overnight. The day after, bacterial colonies in each droplet were counted. The number of colony-forming units (CFU) per mL was calculated by taking the average count of the four droplets for each dilution, multiplied by the dilution factor and then by 100 (to account for the 10 µL volume). This provided the number of intracellular bacteria within the macrophages.

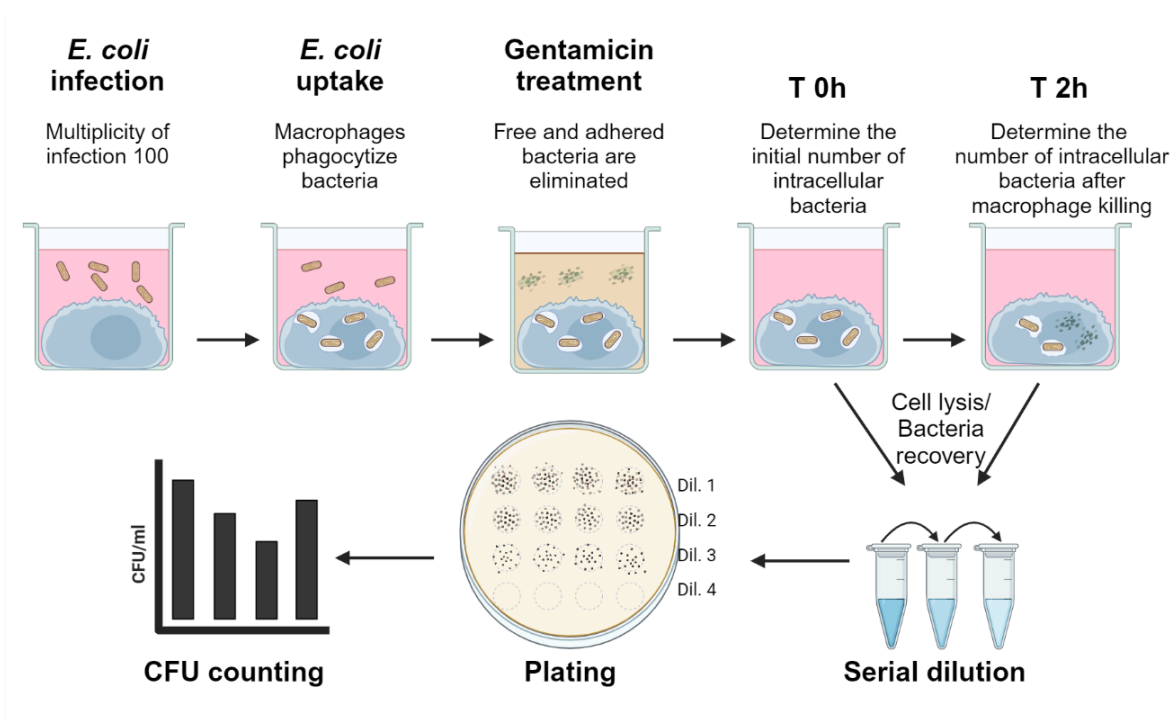


Figure 16: Representative scheme of gentamicin protection assay protocol. Source: Self-elaborated with BioRender.

10. Determination of intracellular metabolite concentration

10.1 Ultra-performance liquid chromatography-mass spectrometry (UPLC-MS)

Concentrations of intracellular metabolites produced during glycolysis and the TCA cycle were determined using UPLC-MS.

10.1.1 Sample preparation

RAW 264.7 cells were seeded in 150 mm dishes and allowed to attach overnight under standard culture conditions. For each condition, 2×10^7 cells were used in each experiment. The following day, cells were either stimulated with 100 ng/mL LPS or left unstimulated for 24 hours. After the incubation, the cells were washed with cold PBS and detached by mechanical scrapping. The cells were then washed by centrifugation with cold PBS and subsequently resuspended in a 2:2:1 (v/v/v) solution of acetonitrile:methanol:water, allowing enzyme denaturation and deproteinization. The mixture was vortexed for 30 seconds and snap-frozen in liquid

nitrogen at $-192\text{ }^{\circ}\text{C}$ for a minute to stop metabolic processes. Samples were then thawed at room temperature and sonicated for 15 minutes. This process was repeated twice. Following this, the samples were incubated for one hour at $-20\text{ }^{\circ}\text{C}$ and then centrifugated at $16,000\text{ }xg$ for 15 minutes for deproteinization. Protein pellets were quantified using the Bradford assay and the supernatant was dried using a SpeedVac-type evaporator. The resultant solid residue was resuspended in a 1:1 (v/v) acetonitrile:water solution. The samples were sonicated at $4\text{ }^{\circ}\text{C}$ for 10 minutes, following which they were centrifuged at $16,000\text{ }xg$ for 15 minutes to eliminate insoluble materials.

10.1.2 Chromatographic separation and metabolomic analysis

An UPLC-MS assay was used to analyze the levels of intracellular lactate, citrate, itaconate, succinate, malate, and oxaloacetate. Prior to UPLC-MS analysis, samples were re-evaporated to dryness and resuspended in Milli-Q water. The chromatographic separation was carried out with an Acquity CORTECS UPLC C18 column directly interfaced into the electrospray ionization source of a Q-TOF mass spectrometer. An elution gradient involving the eluents (A) 23 water/methanol/formic acid (95:5:0.1, v/v/v) with 5 mM ammonium formate, and (B) 100% acetonitrile with 0.1% formic acid and 5 mM ammonium formate, was run from 95% A to 20% A in 4 minutes, then isocratic until 4.5 minutes, to come again to 95% A at 6 minutes and kept to 95% A for an additional period of 2 minutes (8-minutes elution period), at a flow rate of 0.2 mL/minute. MS analysis was performed in the negative ion mode using an MSE method that allows simultaneous detection of analytes through a low-energy function (full scan) and a high-energy function (collision energy) with ion partial fragmentation. All of the metabolites were detected as the $[\text{M}-\text{H}]^{-}$ ion except oxaloacetate, which was detected as the $[\text{M}-\text{H}_2\text{O}-\text{H}]^{-}$ ion. Following the UPLC-MS analysis, data were processed and analyzed to determine the concentration of the various metabolites under investigation.

10.2 Colorimetric assays

Intracellular concentration of succinate (SDH substrate) and fumarate (SDH product) were measured using the Colorimetric Assays Succinate Colorimetric Assay Kit and

Fumarate Assay Kit respectively. To conduct these assays, cells were first lysed using the buffers provided in the kits. For the succinate assay, the resulting lysates were then deproteinized using an Amicon® Ultra-0.5 centrifugal filter. Subsequently, the samples were then added to a 96-well plate, and the reactions were performed according to the manufacturer's instructions.

In the assay, the metabolites were determined by an enzyme reaction, producing a colorimetric product proportional to the amount of metabolite present. Upon completion of the reactions, the absorbance was measured at a wavelength of 450 nm using a VersaMax microplate reader. The concentration of succinate and fumarate was then calculated from standard curves of known compound concentration.

11. Cytokine detection assay in macrophages

The concentrations of cytokines IL-1 β , IL-6, IL-10, IFN- β and TNF- α in macrophage culture supernatants were determined using enzyme-linked immunosorbent assay (ELISA) kits. These assays employ the quantitative sandwich enzyme immunoassay technique wherein a specific pair of antibodies, namely the capture and detection antibodies, bind to their respective cytokine antigens present in the test samples.

In all experiments 3×10^5 macrophages was seeded in a 24-well plate per well one day before starting the experiment. Macrophages were stimulated with 100 ng/mL LPS for 8 hours and supernatants were collected for cytokines measurements. When indicated, cells underwent preincubation with the SDH inhibitor DMM (16 mM) for either 1 hour or 7 days before the addition of LPS.

Next, ELISA 96-well plates were coated overnight with the capture antibody at a concentration of 2 μ g/mL. The following day, the wells were incubated with block buffer for 1 hour to prevent any unspecific interactions. Next, the test samples were loaded onto the microwells along with a standard dilution series. Detection of the cytokines was achieved by the addition of a 1 μ g/mL concentration of the detection antibody. Afterwards, Avidin-HRP-conjugate was added for reaction for 30 minutes. Next, the ABTS liquid substrate was added to each well and incubate for color

development. The intensity of the color signal was measured at a wavelength of 405 nm using a VersaMax microplate reader with background subtraction at 650 nm.

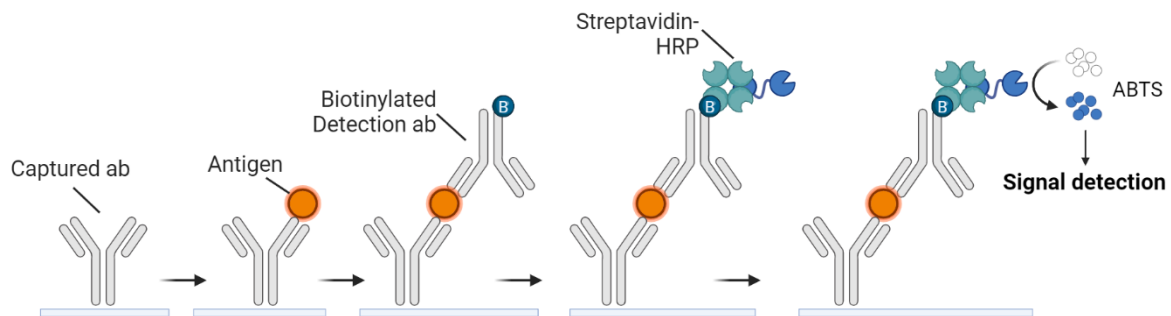


Figure 17: Generalized scheme of a sandwich ELISA protocol. Source: Self-elaborated with BioRender.

12. NO detection assay in RAW 264.7 macrophages

In this assay, nitrite is measured in cell culture supernatants using the Griess reagent. This measurement provides a surrogate marker and quantitative indicator of NO production. Macrophages, at a density of 3×10^5 cells/well, were seeded into each well of a 24-well plate and were allowed to adhere for approximately 24 hours before stimulation. Stimulation was achieved with LPS at a concentration of 100 ng/mL in phenol red-free DMEM media to avoid colorimetric interference. Following 24 hours of LPS stimulation, supernatants were collected for nitrite determination.

The collected culture supernatants were then subjected to the Griess reaction according to the instructions of the Griess Reagent Kit. Aliquots of 50 μ L of culture supernatants and nitrite standards were added to corresponding wells of a 96-well flat bottom plate. Next, 50 μ L of Sulfanilamide solution (Griess Reagent I) was added to all the wells. The plate was then incubated at room temperature for 5 minutes. Post incubation, 50 μ L of N-(1-Naphthyl)ethylenediamine dihydrochloride solution (Griess Reagent II) was added to each well. The plate was mixed and further incubated at room temperature for 5-10 minutes. The color change was measured spectrophotometrically using a VersaMax microplate reader set at a wavelength of 548 nm. The measured absorbance corresponded to the nitrite concentration

present in the sample, providing for an accurate estimate of NO production in the macrophages.

13. Seahorse XF assay in RAW 264.7 macrophages

Cellular metabolic profiling of RAW 264.7 macrophages was assessed using the Seahorse Extracellular Flux Analyzer to measure OCR and ECAR, representative of mitochondrial respiration and glycolysis, respectively.

RAW 264.7 macrophages were seeded at a density of 4×10^4 cells per well in a Seahorse XFp 8-well cell culture plate or 6×10^4 cells per well in a 24-well plate format. They were then incubated at 37 °C with 5% CO₂ overnight to allow cell adherence. The next day, the culture medium was replaced with Seahorse XF Base Medium supplemented with 2 mM L-glutamine, 1 mM sodium pyruvate, and 10 mM glucose. The cells were then incubated for 1 hour at 37 °C in a CO₂-free incubator to allow media temperature and pH equilibration.

13.1 Measure mitochondrial function

The Seahorse XF Cell Mito Stress Test Kit was used to measure essential parameters of mitochondrial function according to the manufacturer's instructions. The Seahorse XFp sensor cartridge was hydrated overnight with Seahorse XF Calibrant at 37 °C in a non-CO₂ incubator. On the day of the assay, the injection ports of the sensor cartridge were loaded with oligomycin, carbonyl cyanide 4-(trifluoromethoxy) phenyl-hydrazone (FCCP), and rotenone/antimycin A to final concentrations of 2.6 μM, 1 μM, and 1 μM respectively.

Bioenergetic analysis was performed using the Seahorse XF HS mini 8-well extracellular flux analyzer. The assay followed the *XF Cell Mito Stress Test Acute Injection* protocol. After obtaining baseline measurements, the cells were sequentially exposed to oligomycin, FCCP, and rotenone/antimycin A, with a mix-wait-measure cycle being repeated after each injection.

OCR and ECAR were automatically calculated and recorded by the Seahorse XFp software. Following the assay, cells were lysed and protein concentration was

determined using a BCA Protein Assay kit. All OCR and ECAR values were normalized to total cellular protein.

Results were analyzed using Wave software to determine parameters of mitochondrial function, including basal respiration, ATP-linked respiration, proton leak, maximal respiration, reserve capacity, and non-mitochondrial respiration.

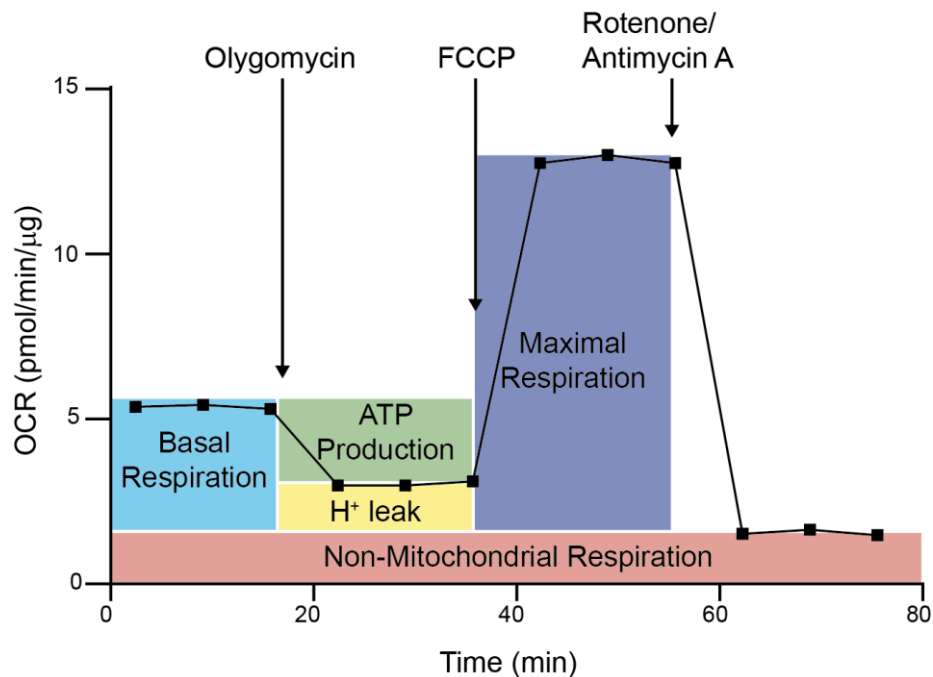


Figure 18: Schematic illustration of metabolic parameters assessed in the Seahorse Cell Mito Stress test. Source: Self-elaborated.

13.2 ATP production rate determination

The ATP production rate in RAW 264.7 macrophages was assessed using the Seahorse XFp Real-Time ATP rate assay Kit, which distinguishes the ATP produced during glycolysis from that obtained after mitochondrial respiration thanks to the serial addition of 1.5 μM oligomycin and the rotenone/antimycin A 0.5 μM each. The ATP production rate was measured using the Seahorse XFe24 Extracellular Flux Analyzer, with ATP rate measurements made every 8.5 minutes for a total of three measurements. ATP production rates were calculated based on the changes in OCR and ECAR induced by oligomycin and rotenone/antimycin A injection.

To start, basal OCR and ECAR were measured. Then, oligomycin was injected to inhibit ATP synthesis in mitochondria, leading to a decrease in OCR and an increase in ECAR due to a shift towards glycolysis. The changes in OCR and ECAR following oligomycin injection were used to calculate the rate of mitochondrial ATP production. Subsequently, rotenone/antimycin A were injected to inhibit both mitochondrial respiration and ATP synthesis. This caused a further increase in ECAR, representing the maximum glycolytic capacity of the cells. The change in ECAR following rotenone/antimycin A injection was used to calculate the rate of glycolytic ATP production. By summing up the ATP production rates from both mitochondrial respiration and glycolysis, the total cellular ATP production rate was determined.

The analysis of ATP production rates was performed using Wave software. To normalize the ATP production rate values, cells were stained with 4',6-diamidino-2-phenylindole (DAPI) and the number of cells was counted using a Cytation 5 Cell Imaging Multi-Mode Reader. Cell count was used to adjust the ATP production rate values. The ATP production rates were reported in pmoles per minute per cell (pmol/min/cells).

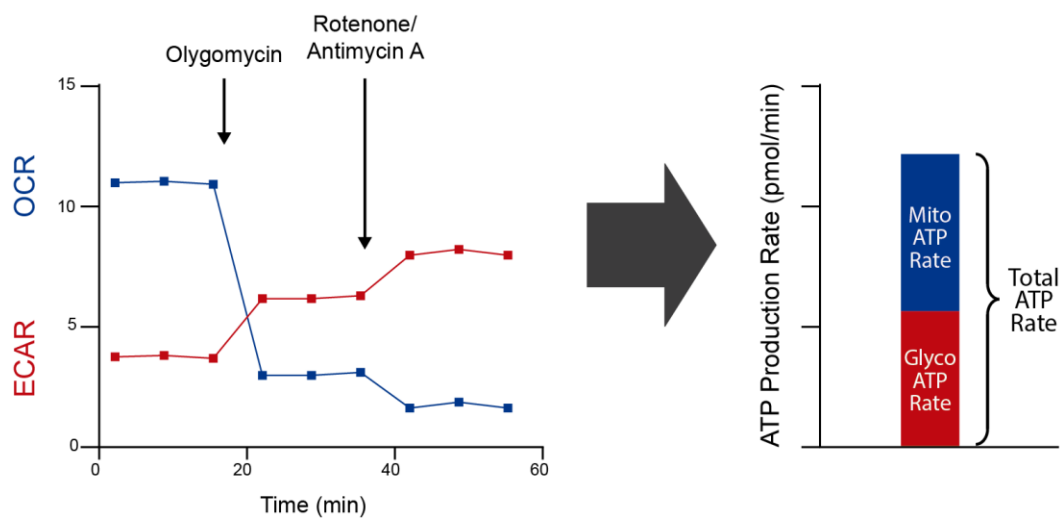


Figure 19: Representative scheme of Agilent Seahorse XF Real-Time ATP Rate Assay.
Source: Self-elaborated.

14. Electron transport chain (ETC) activities

Activities of the respiratory chain complexes in cells were measured spectrophotometrically using the method of Bujan *et al.*¹¹⁶. Two 100 mm dishes of confluent cells were detached, washed with ice-cold PBS and collected by centrifugation at 800 xg for 5 minutes. Pellets were resuspended in 300 μ L homogenization buffer (mannitol buffer). The mannitol buffer pH 7.2 consisted of 225 mM D-mannitol, 75 mM sucrose, 10 mM Tris-HCl and 0.1 mM EDTA. The cell suspension was sonicated twice for 5 seconds at 200 watts in an ice bath. Cell homogenates were maintained in the ice bath prior to the spectrophotometric enzyme assays.

14.1 CI Activity

CI activity was assayed by monitoring the oxidation of NADH at 340 nm with decylubiquinone, a hydrophilic analogue of ubiquinone (coenzyme Q₁₀), as the electron acceptor. The reaction mixture consisted of 20 mM phosphate buffer (pH 7.4), 1 mg/mL BSA, 1 mM EDTA, 1 mM sodium azide, 200 μ M NADH, and 100 μ M decylubiquinone. The decrease in absorbance was measured for 3 minutes and the slope of the linear portion of the curve was used to calculate the enzymatic activity.

14.2 CII Activity

CII activity was determined by monitoring the reduction of the artificial electron acceptor 2,6-dichlorophenol-indophenol (DCPIP) at 600 nm in the presence of succinate via the coenzyme Q₁₀ analog decylubiquinone. The reaction mixture contained 25 mM phosphate buffer (pH 7.5), 2 mg/mL BSA, 20 mM succinate, 1 mM KCN and 50 μ M DCPIP. The slope of the linear portion of the absorbance change over two minutes was used to measure enzymatic activity.

14.3 CIII Activity

CIII activity was assessed by monitoring the reduction of cytochrome c at 550 nm in the presence and absence of antimycin (12.5 mg/mL), a specific inhibitor of respiratory CIII. The reaction mixture consisted of 100 mM phosphate buffer (pH 7.5), 1 mM KCN, 0.25 mM EDTA, 50 μ M cytochrome c and 200 μ M decylubiquinol.

The increase in absorbance was measured over 3 minutes and a value for the enzymatic activity was obtained from the slope of the linear portion of the curve. The specific CIV activity is obtained by subtracting the antimycin-insensitive activity from the total activity.

14.4 CIV Activity

CIV activity was examined by the oxidation of reduced cytochrome c at 550 nm. The reaction mixture consisted of 52 mM phosphate buffer (pH 7) and 0.1 mM reduced cytochrome c. The decrease in absorbance was measured for 3 minutes and the slope of the linear portion of the curve was used to calculate enzymatic activity.

14.5 Citrate Synthase (CS) Activity

CS activity was used to normalize OXPHOS complexes activities. The CS is an enzyme found in the citric acid cycle and its activity is often used as a marker for the total amount of active mitochondria. The assay is performed in a reaction mixture containing 100 mM Tris-HCl buffer (pH 8.1), 0.1% Triton X-100, 0.5 mM oxaloacetate, 0.1 mM 5,5'-dithiobis-2-nitrobenzoic acid (DTNB), and 0.3 mM Acetyl CoA. The rate of formation of the thiolate anion of CoA (CoA-SH), detectable at an absorbance of 412 nm, is directly proportional to the CS activity. Measurements were taken every minute for five minutes, and the enzymatic activity was calculated based on the slope of the linear portion of the curve.

15. Statistical analysis

All statistical analysis was performed using GraphPad Prism software. For analyses involving multiple groups, Analysis of Variance (ANOVA) was employed, followed by *post hoc* assessment using Tukey's multiple comparison test. In scenarios where only two independent groups were compared, statistical significance was determined through either the Unpaired Student's t-test (two-tailed) or the Mann-Whitney U test (two-tailed), based on the data distribution. Values of $p < 0.05$ were considered statistically significant. In the graphical representation of the results, each data point represents a unique biological replicate. The data are representative

of at least three independent experiments. Unless specified otherwise, data are conveyed as the mean \pm standard error of the mean (SEM).





Results



Results

Chapter 1: Generation of RAW 264.7 *Ndufs4*^{-/-}, *Sdha*^{-/-} and *Sdhb*^{-/-} lines

Ndufs4, *Sdhb* and *Sdha* are subunits crucial for the function of CI and CII of the ETC, playing an important role in cellular energy production. ETC is important not only for energy metabolism, but also for processes as diverse as ROS production and apoptosis signaling. In addition, the role of the ETC is critical in macrophage function and their immunological response. Consequently, the generation of murine macrophages RAW 264.7 cell lines with targeted KO of these genes provides a robust experimental system to investigate the impact on cellular metabolism, immune responsiveness and overall cellular homeostasis.

This chapter therefore aims to describe the methodological approach used to generate the RAW 264.7 *Ndufs4*^{-/-}, *Sdha*^{-/-} and *Sdhb*^{-/-} cell lines using the CRISPR-Cas9 HITI gene editing method. This genetic modification serves as a precursor to downstream functional studies, thereby creating a cellular model for investigating the multiple roles of the ETC in the broader context of immune system functionality.

1. Generation of plasmids for gene editing of RAW 264.7 cells

The methodology used to generate the RAW 264.7 KO cell lines was based on the Cas9-induced HITI strategy, an advanced genome editing technique designed to overcome the limitations of traditional HDR methods. This strategy allows targeted DNA integration without the need for a homologous template, relying instead on NHEJ for DNA repair.

Two specialized plasmids were used for the HITI strategy: the targeting plasmid and the donor plasmid. The targeting vector encodes the Cas9 nuclease and a gRNA that targets the first exon of the genes (*Ndufs4*, *Sdha* and *Sdhb*). In addition, the

donor plasmid carries an exogenous DNA sequence flanked by gRNA target sequences that facilitates its own integration into the genomic DNA following Cas9 mediated cleavage. The insertion of this sequence serves to disrupt and inactivate the targeted gene while also providing a selection marker for the identification of successfully edited cells.

1.1 pX330+gRNA plasmids

To construct the pX330+gRNA plasmids, gRNAs inserts were generated after forward and reverse oligonucleotides (CL1-6) annealing, and ligated into to the pX330 vector (**Figure 20**). Successful insertion was then confirmed by PCR using a primer specific to the vector (CL19) and a primer containing the gRNA sequences for each target gene (CL2 for *Ndufs4*, CL4 for *Sdha*, and CL6 for *Sdhb*) (**Figure 21A**). Sanger sequencing validated the cloned gRNAs sequences and the absence of mutations (**Figure 21B**).

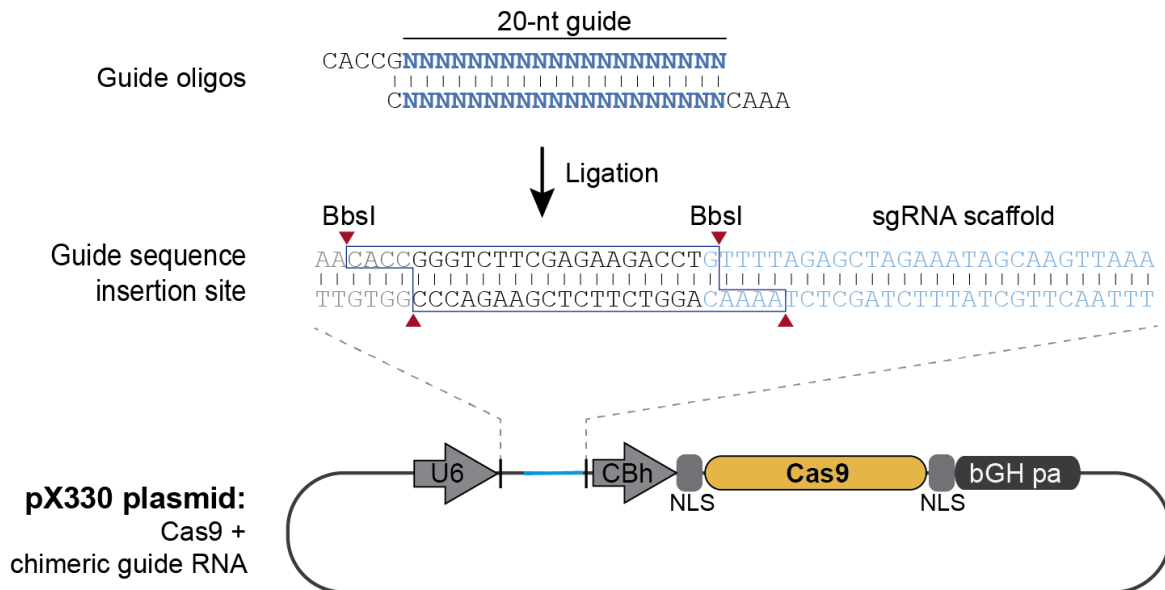


Figure 20: Diagram illustrating the insertion of guide RNA sequences into a plasmid (pX330) carrying the Cas9 gene and sgRNA backbone. Top strand guides (in blue) are designed with specific end sequences that enable them to connect into the pX330 vector at the BbsI restriction sites. After pX330 is digested with BbsI, these sites are replaced by the new guide sequences through direct ligation.

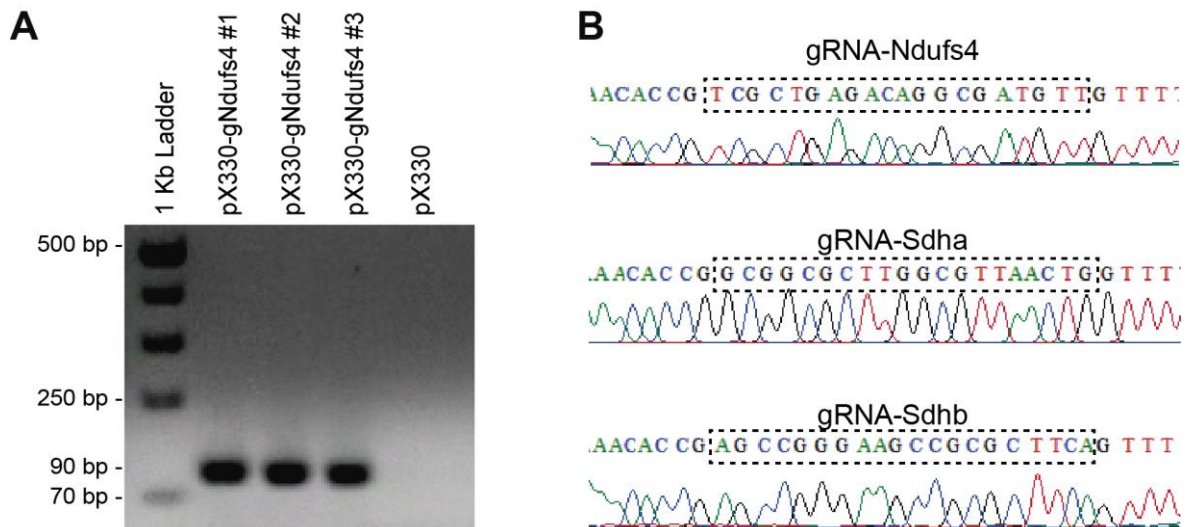


Figure 21: (A) Example of results from the colonies verification PCR of the pX330+gRNA plasmids ligation. pX330 plasmid used as negative control. (B) Sanger sequencing of the plasmid pX330+gRNA .

1.2 pBSBlast+gRNA plasmids

The HITI method was used to overcome the difficulty of selecting successfully edited cells from unedited cells, a common problem with conventional CRISPR/Cas9 editing techniques that typically requires additional selection steps. As mentioned before, the editing using the HITI system required a second plasmid containing a blasticidin resistance gene flanked by the gRNA target sequence. The blasticidin resistance gene disrupts the gene of interest upon integration into genomic DNA following a Cas9-induced double-strand break, facilitating targeted gene knockout. For each gene, an appropriate fragment was generated by PCR using two special primers (CL7-12). As shown in **Figure 22**, the primer pair hybridized at their 3' ends to the flanking regions of the blasticidin resistance cassette in the pBS-Blast plasmid. The remaining bases of the primer sequences correspond to the gRNA target sequence including the PAM sequence, the cut site for the Sall or BamHI enzymes, and at the 5' end of the cassette, a region corresponding to termination codons located in different reading frames.

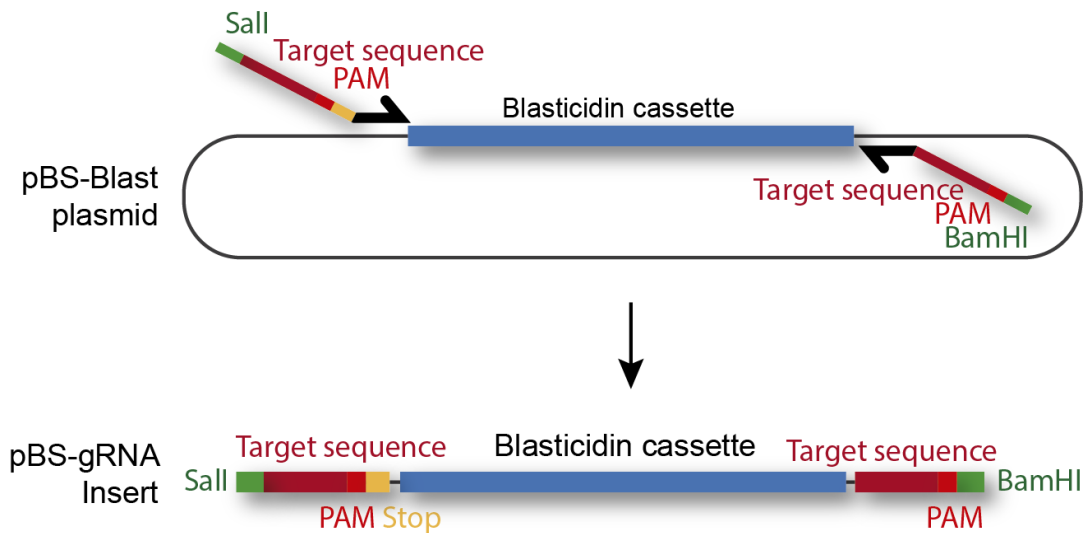


Figure 22: PCR scheme illustrating the generation of the blasticidin cassette flanked by the target sequence.

The products of the PCR, containing blasticidin resistance gene flanked by the gRNA target sequence, were analyzed by agarose gel electrophoresis (**Figure 23A**). It can be seen that a single fragment has been amplified, and the resulting products have an appropriate size of 1668 bp, corresponding to the blasticidin cassette flanked by the primer sequence.

Once the fragment was purified, it was ligated into the pBluescript II-based vector and amplified to obtain the corresponding pBSBlast+gRNA plasmids. Comparable to the pX330+gRNA plasmid, positive colonies were selected through PCR verification using the same primers that were used to obtain the fragment to be cloned. The result obtained after agarose gel electrophoresis shows that all selected colonies contained the recombinant plasmid of interest, with the 1668 bp band corresponding to the blasticidin cassette flanked by the primer sequences (**Figure 23B**).

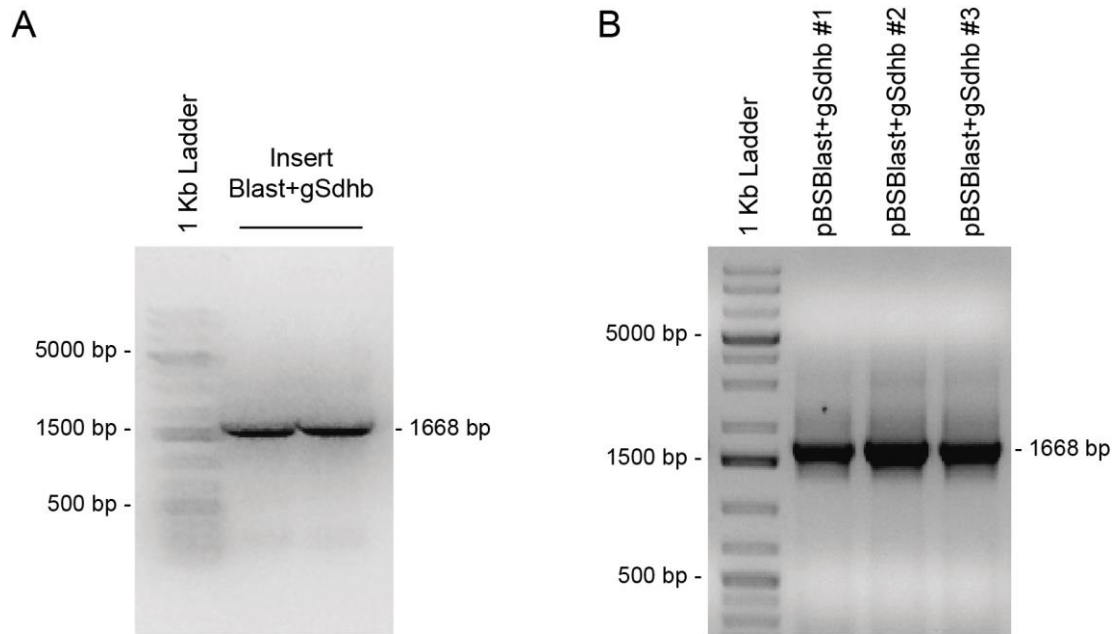


Figure 23: (A) Example of PCR to generate the blasticidin cassette flanked by the target sequence and (B) PCR to verify correct ligation of the pBSBlast+gRNA plasmids.

After purifying the plasmid, the correct incorporation of the Cas9/gRNA target sequences at the ends of the blasticidin cassette was confirmed by Sanger sequencing. As observed in **Figure 24**, all ends contain the gRNA sequence and the PAM sequence.

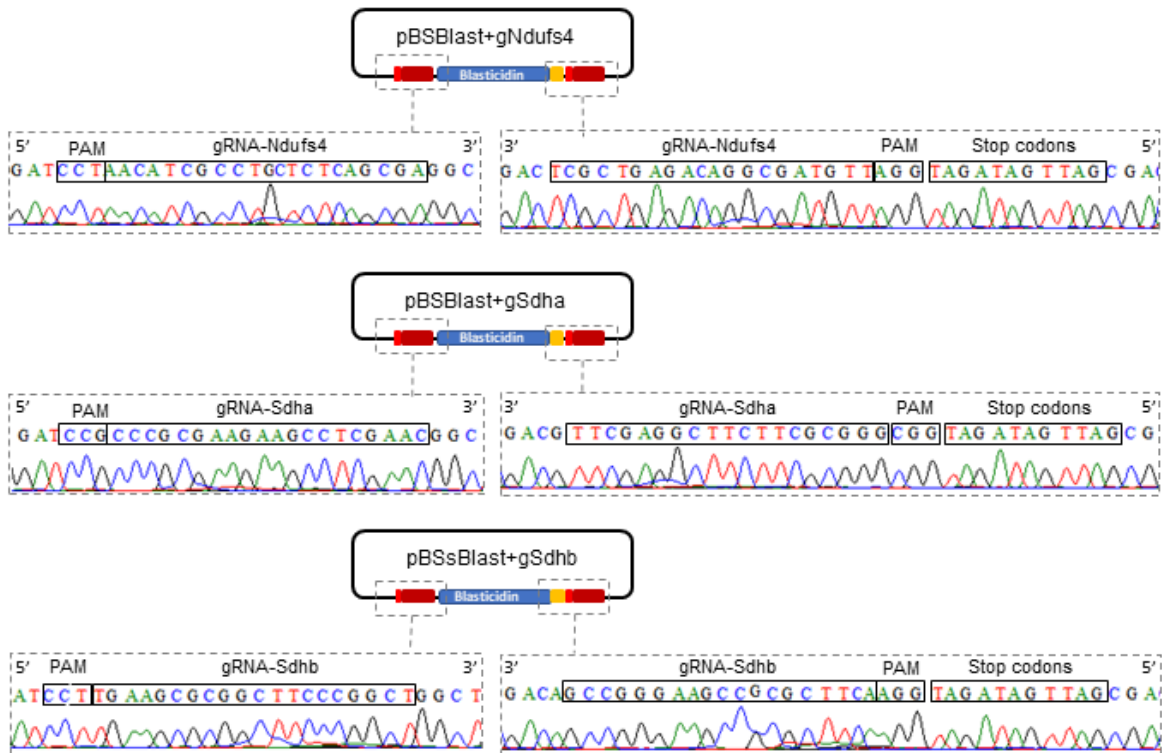


Figure 24: pBSBlast+gRNA plasmid schematic and sequencing results of the indicated areas.

2. Generation of RAW 264.7 KO cells for *Ndufs4*, *Sdha*, and *Sdhb*

Upon obtaining the two components of the CRISPR/Cas HITI system, the pBSBlast+gRNA and pX330+gRNA plasmids, they were co-transfected into RAW 264.7 cells via lipofection. As previously mentioned, cells that incorporated the selection plasmid were selected using blasticidin. The optimal blasticidin concentration for selection was determined through a resistance curve against varying concentrations of the antibiotic. Daily microscopic observations indicated that a minimum concentration of 2 $\mu\text{g}/\text{mL}$ of blasticidin resulted in 100% cell death by the 5th day. Therefore, this concentration was chosen to use post-transfection.

Following transfection, a limiting dilution was performed and plates were incubated for approximately two weeks. After this period, wells showing growth of a single cell colony were selected and analyzed by PCR to determine whether gene modification had occurred on-target or off-target (**Figure 25A**). In this analysis, the incorporation

of the blasticidin cassette was determined using a primer pair specific for genomic regions flanking the target sequence, which allowed to determine whether an insertion had occurred at the Cas9 cut site. Analysis of the PCR products showed that several of the clones had the insertion at the correct target site (**Figure 25B-C**). This confirmed the successful gene modification for *Ndufs4*, *Sdhb*, and *Sdha* in RAW 264.7 cells.

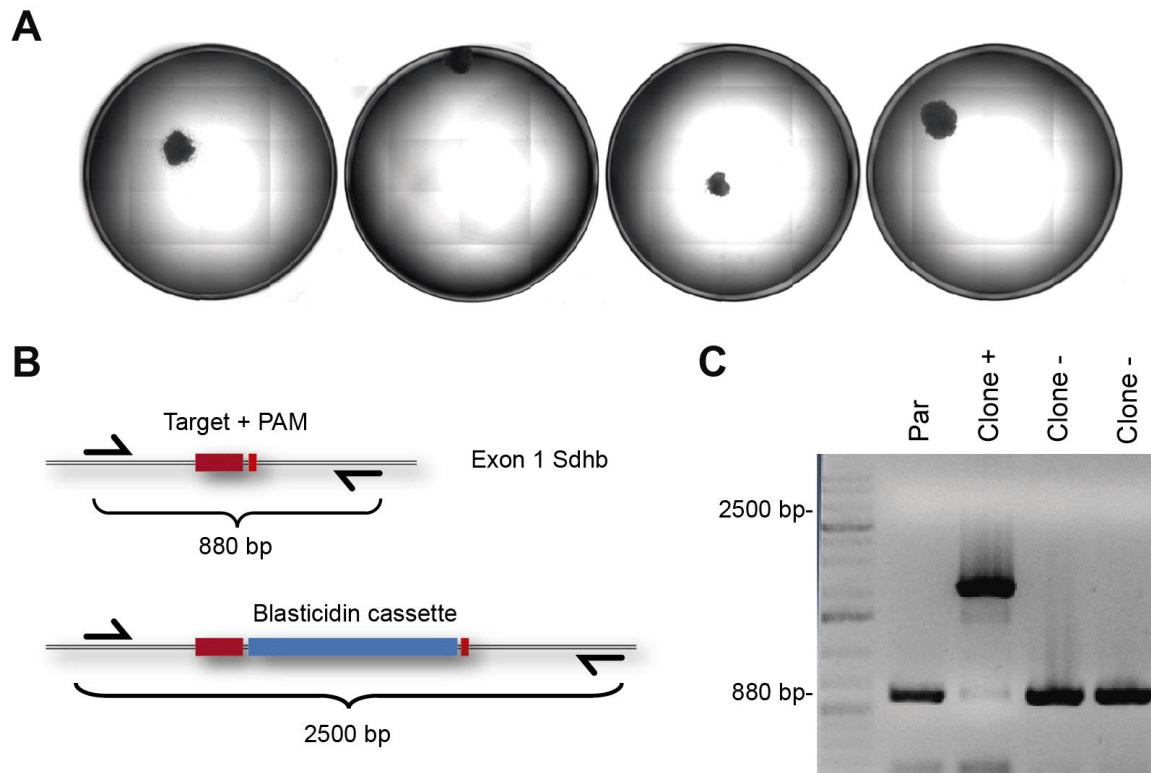


Figure 25: Clone selection. (A) Representative photographs examples of individual wells containing the growth of isolated single cell colonies. (B) Schematic shows the unedited *Sdhb* gene locus, its modification with the donor vector, the location of primers used for PCR and the corresponding sizes of the amplifications. (C) PCR Analysis for target insertion verification. Gel electrophoresis image illustrates an example of specific insertion at the target site in one of the clones.

To further validate the gene inactivation, Western blot analysis was performed to confirm the absence of protein in the edited cells. The results showed the absence of *Ndufs4*, *Sdhb*, and *Sdha* proteins in the respective modified cells, corroborating the PCR results (**Figure 26**). Interestingly, the absence of *Sdha* was observed to

lead to the disappearance of Sdhb in the modified cells, while the levels of Sdha remained intact in *Sdhb*^{-/-} cells.

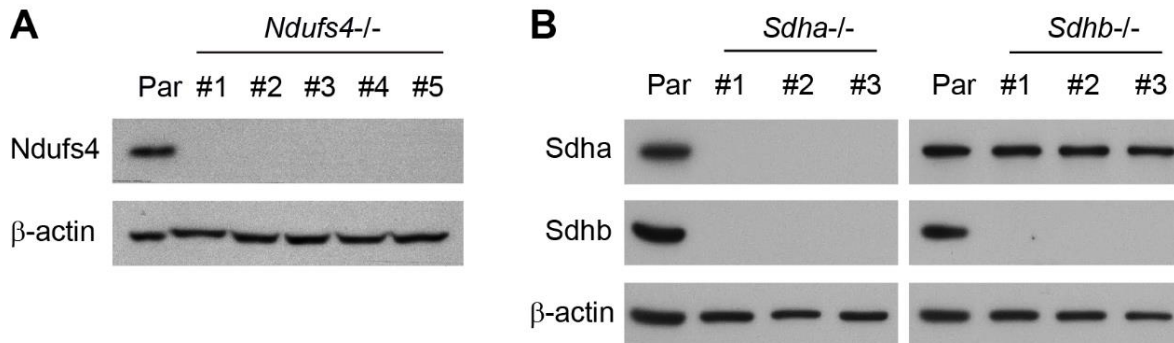


Figure 26: Western blotting analysis of KO cell lines. (A) Parental and *Ndufs4*^{-/-} RAW 264.7 cells western blot for *Ndufs4*, with β-actin as the loading control. The clones for *Ndufs4* were specifically named *Ndufs4*^{-/-}, followed by a serial number. (B) . Western blotting for *Sdha*, *Sdhb*, and β-actin of parental (Par) *Sdha*^{-/-} and *Sdhb*^{-/-} RAW 24.7 cells, where the clones for *Sdha* were named *Sdha*^{-/-} and the clones for *Sdhb* were named *Sdhb*^{-/-}, each followed by a serial number.

Finally, the clones that had been successfully modified were subjected to Sanger sequencing to check for genetic modifications around the editing target site (**Table 5**). These modifications were a direct result of the cuts made by the CRISPR/Cas9 system on the gene of interest. All the observed changes had a common effect: disrupting the reading frame of the gene. This disruption of the reading frame led to KO genes, resulting in their inability to be expressed.

Chapter 2: Role of CI in macrophage respiration and effector functions

The immunological profile of macrophages is linked to their mitochondrial functions, particularly those related to the ETC. The previous chapter focused on the generation of RAW 264.7 cell lines with targeted gene KO of *Ndufs4*. The *Ndufs4* gene is located on chromosome 13, contains five exons and encodes the accessory NADH dehydrogenase [ubiquinone] iron-sulfur protein 4 (*Ndufs4*) of CI, also known as the 18 kDa subunit, which plays an important role in CI assembly and activity^{102,117,118}.

The primary goal of this chapter is the characterization of the *Ndufs4*^{-/-} RAW 264.7 murine macrophage cell line as a model system, with specific focus on investigating the consequences of *Ndufs4* deficiency on mitochondrial functions. In particular, the effects on mitochondrial respiration and the formation of respirasome, will be investigated. In addition, this chapter aims to elucidate the impact of *Ndufs4* deficiency on macrophage effector functions including a detailed analysis of changes in cytokine profiles, critical for modulating immune responses, as well as changes in the phagocytic capacity of macrophages. These parameters are essential for a macrophage's ability to clear pathogens, present antigens and modulate tissue homeostasis.

1. Impact on ETC activities

The study began by examining the impact of *Ndufs4* absence on mitochondrial respiratory functions, focusing on the activities of the ETC. Spectrophotometric measurements were taken in mitochondria-enriched preparations of *Ndufs4*^{-/-} cells, and these results were subsequently normalized to the respective citrate synthase (CS) activity (**Figure 27A**).

The findings revealed a significant decrease in CI activity in the *Ndufs4*^{-/-} cells, registering only 56% of that in the control cells. This pronounced reduction in CI activity underscores the critical role that *Ndufs4* plays in the NADH dehydrogenase activity of CI. Conversely, no significant differences were detected in the activities of ETC complexes II-IV between *Ndufs4*^{-/-} and control cell lines (**Figure 27B**).

Furthermore, the reduction of CI activity in *Ndufs4*^{-/-} cells remained consistent whether the CI activity was normalized to the activities of CII and CIV or to CS (**Figure 27C**). This consistent reduction further emphasizes the specific impairment of CI activity due to the absence of *Ndufs4*.

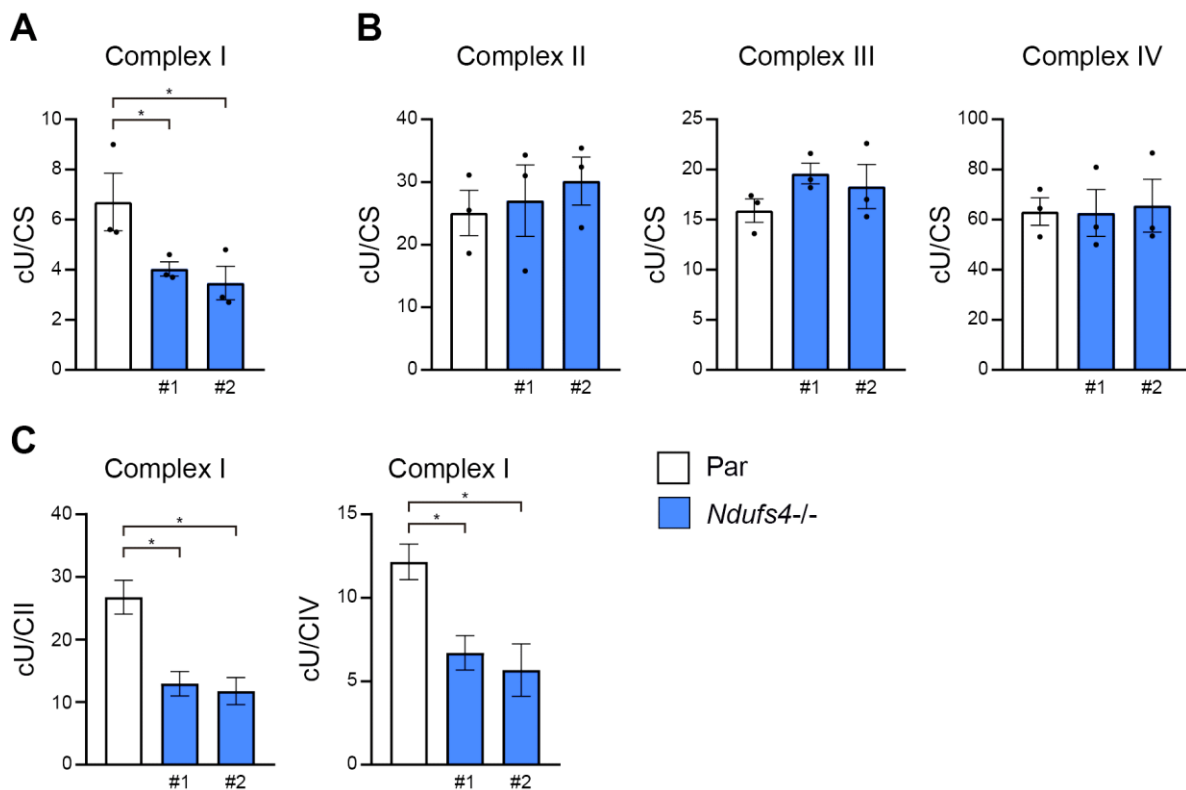


Figure 27: Assessment of mitochondrial complexes activity in *Ndufs4*^{-/-} macrophages. (A-B) Activities of ETC complexes I-IV, assayed spectrophotometrically and normalized to CS activity in mitochondria isolated from parental (Par) and *Ndufs4*^{-/-} RAW 264.7 cells. (C) Comparative representation of CI activity, displayed as CI/CII in the left panel and CI/CIV in the right panel. The statistical significance is displayed as follows: *, P < 0.05; **, P < 0.01; ***, P < 0.005; ****, P < 0.001, ANOVA test. Each point represents a biological replicate. Data are shown as the mean \pm SEM.

2. Evaluation of mitochondrial respiratory profile

The mitochondrial respiratory profile of *Ndufs4*^{-/-} macrophages was further investigated to understand the specific impact of *Ndufs4* deficiency on various aspects of respiration. The OCR served as a key metric, and its measurement was carried out both before and after the sequential addition of oligomycin (an ATP synthase inhibitor), FCCP (a proton ionophore), and rotenone (a CI inhibitor) (**Figure 28A**).

In the *Ndufs4*^{-/-} macrophages, the study revealed lower levels of basal respiration, highlighting a decrease in the metabolic activity of the cells. This was accompanied by significantly lower levels of maximal respiration and ATP production compared to control cells (**Figure 28B**). Collectively, these observations indicated a global decay in the electron flux through ETC and energy conversion within the mitochondria.

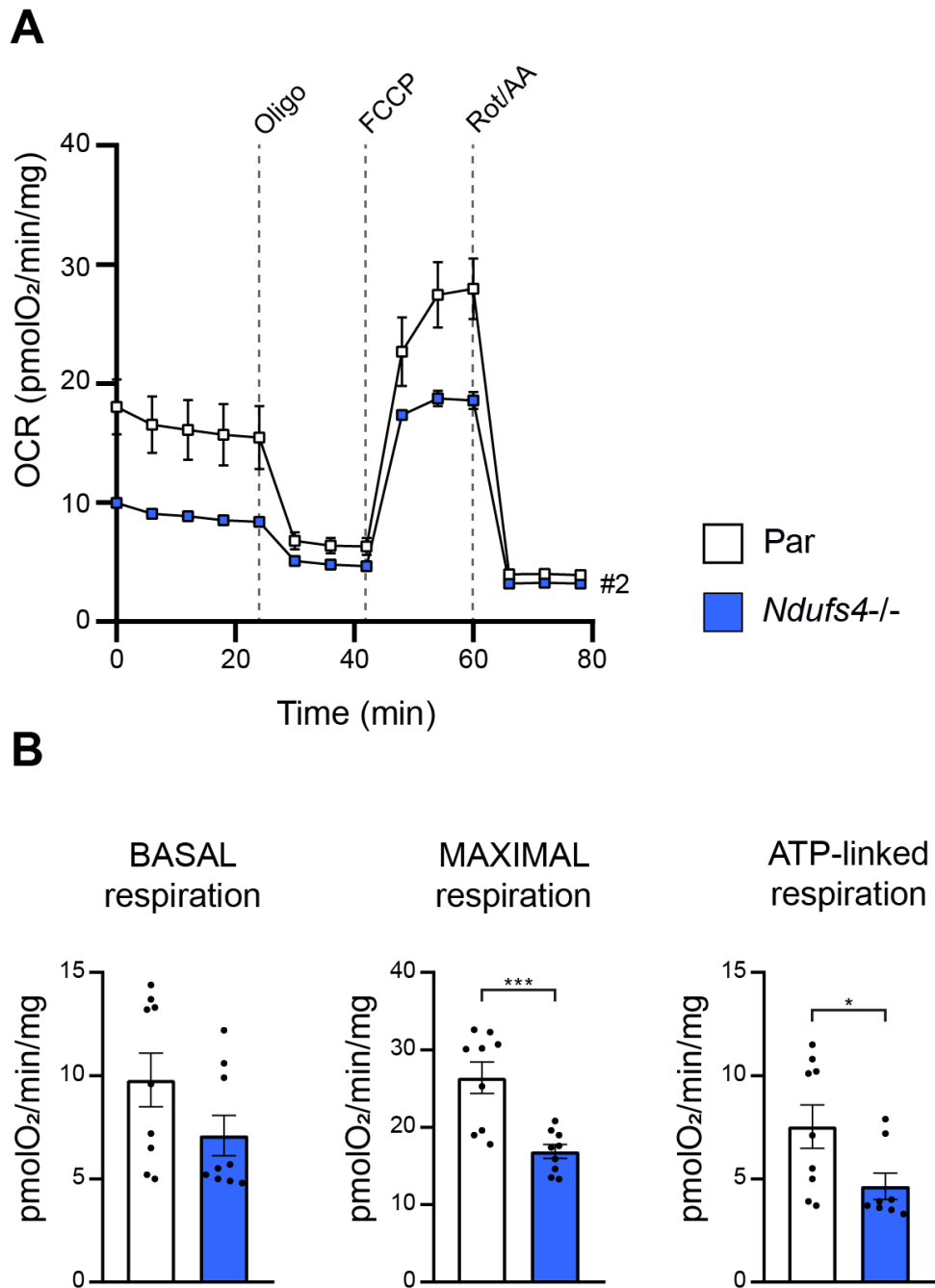


Figure 28: OCR in *Ndufs4*^{-/-} RAW 264.7 sublines. (A) Measurement of OCR under basal conditions and following the sequential addition of specific compounds: oligomycin at 2.6 μ M, FCCP at 1 μ M, and a combination of rotenone (Rot) and antimycin A (AA) at 1 μ M. (B) Graphical representation of basal respiration, maximal respiration, and ATP production. OCR values were normalized against mg of protein. The statistical significance is displayed as follows: *, $P < 0.05$; **, $P < 0.01$; ***, $P < 0.005$; ****, $P < 0.001$, Mann-Whitney U-test. Each point represents a biological replicate. Data are shown as the mean \pm SEM.

3. Changes in mitochondrial function

Analysis of *Ndufs4*^{-/-} cells was extended to determine additional alterations in mitochondrial function as a result of the absence of *Ndufs4*. *Ndufs4*^{-/-} cells were found to have increased basal levels of MitoSOX-derived fluorescence, indicating an increase in mitochondrial ROS levels (**Figure 29A**). However, this increase was not associated with a significant reduction in their MMP (**Figure 29B**), suggesting that the overall integrity of the mitochondrial membrane remained intact despite the oxidative changes.

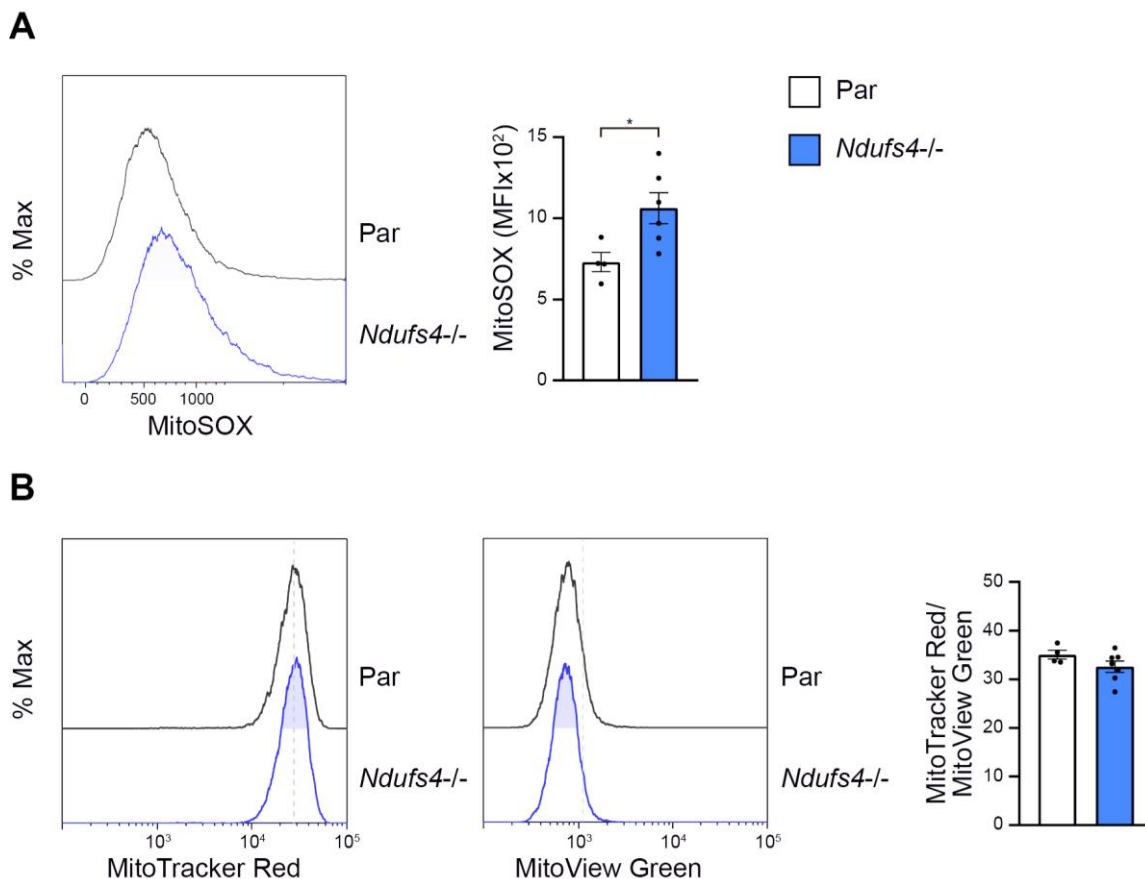


Figure 29: Analysis of mitoROS levels and MMP in *Ndufs4*^{-/-} macrophages. (A) Flow cytometry histograms of MitoSOX staining (left) and a graph displaying mean fluorescence intensity (MFI) values, reflecting relative mitoROS levels (right). (B) Features representative flow cytometry histograms (left) of MitoTracker Red CMXRos and MitoView Green staining, along with a graph showing the ratio of MMP (MitoTracker Red) to mitochondrial mass (MitoView Green), enabling a precise determination of potential differences per unit of mitochondrial mass (right). The statistical significance is displayed as follows: *, P < 0.05; **, P < 0.01; ***, P < 0.005; ****, P < 0.001, two-tailed t-test. Each point represents a biological replicate. Data are shown as the mean \pm SEM.

Interestingly, despite these alterations in mitochondrial parameters, *Ndufs4*^{-/-} macrophages proliferated normally and showed no obvious signs of apoptosis when cells were cultured in complete DMEM containing glucose (**Figure 30A**). However, when glucose was replaced by galactose in the media, the proliferation of the KO cell line was significantly impaired (**Figure 30B**).

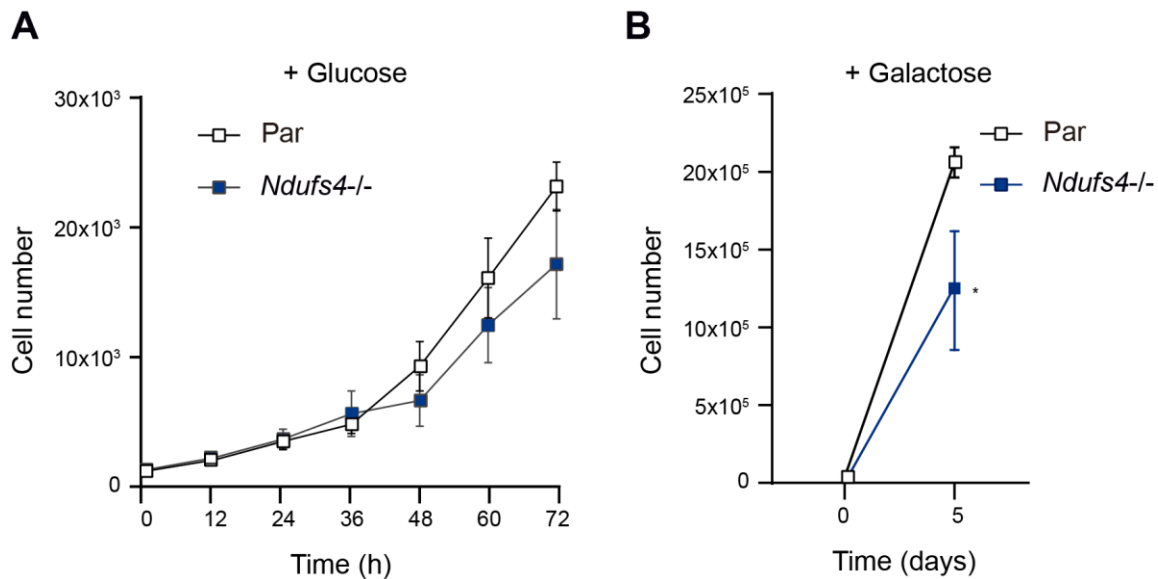


Figure 30: Effect of *Ndufs4* absence in macrophage proliferation. (A) Parental and *Ndufs4*^{-/-} RAW 264.7 cells (1,000 cells per well) were seeded on 96-well plates, and cultured in complete DMEM. (B) Parental and *Ndufs4*^{-/-} RAW 264.7 cells (40,000 cells per well) were plated on 6-well plates. Cells were cultured in media containing galactose in the complete absence of glucose. The number of viable cells was measured at specified time intervals. The graph shows the mean of individual biological replicates \pm standard deviation (SD).

4. Stability of CI subunits in *Ndufs4*^{-/-} macrophages

In the absence of NDUF54, the stability of two CI subunits close to NDUF54, namely NDUFV1 (N module) and NDUF9 (Q module), was also investigated. These subunits' protein levels were analyzed in *Ndufs4*^{-/-} macrophages. As shown in **Figure 31**, the levels of NDUFV1 and NDUF9 were similar to those observed in parental cells. This indicates that the absence of NDUF54 did not cause any changes in the stability of these CI subunits.

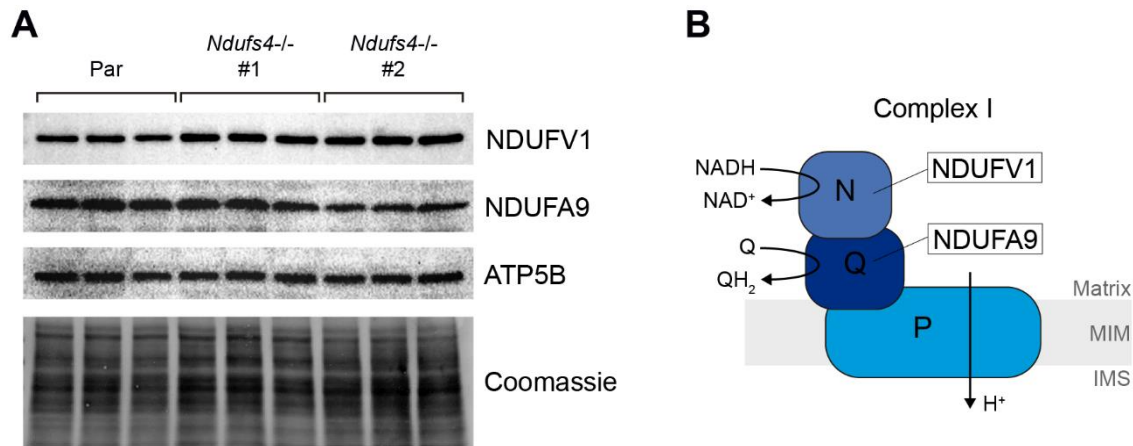


Figure 31: Detection of CI subunits in *Ndufs4*^{-/-} macrophages. (A) Western blot for NDUFV1 (N module) and NDUFA9 (Q module), with ATP5B and Coomassie staining used as loading controls. (A) Schematic representation of CI, highlighting the specific functions of the modules: The N module containing an NADH oxidation site, the Q module containing a ubiquinone reduction site, and the P module involved in proton-pumping activity. The positions of NDUFV1 and NDUFA9 are indicated. IMM: inner mitochondrial membrane. IMS: intermembrane space.

5. Analysis of distribution pattern of free ETC complexes and SCs

A detailed analysis of the distribution pattern of free ETC complexes and SCs was then performed using 1D BN-PAGE, followed by Western blot analyses with specific antibodies against NDUFA9 (CI), core 2 (CIII), COX5a (CIV) and ATP5A (CV).

The analysis revealed that *Ndufs4*^{-/-} cell lines lacked fully assembled free CI and CI-containing SCs (SC I + III₂ + IV_n, SC I + III₂). This finding highlights the particular influence that the absence of NDUFS4 has on the assembly process. Interestingly, the lack of fully assembled SCs was accompanied by a significant accumulation of lower molecular weight SCs. This accumulation suggests the presence of partially assembled SCs (**Figure 32**) and reflects a potential interruption or inhibition in the assembly process in the absence of NDUFS4.

The study also observed higher levels of CIII₂ and CIV₂ compared to control cells. This observation might represent a compensatory mechanism or an altered distribution within the respiratory chain complexes.

Finally, no significant differences were found in the monomer or dimer levels of CV, reinforcing that the absence of NDUF54 specifically affected certain components without altering the entire mitochondrial respiratory machinery.

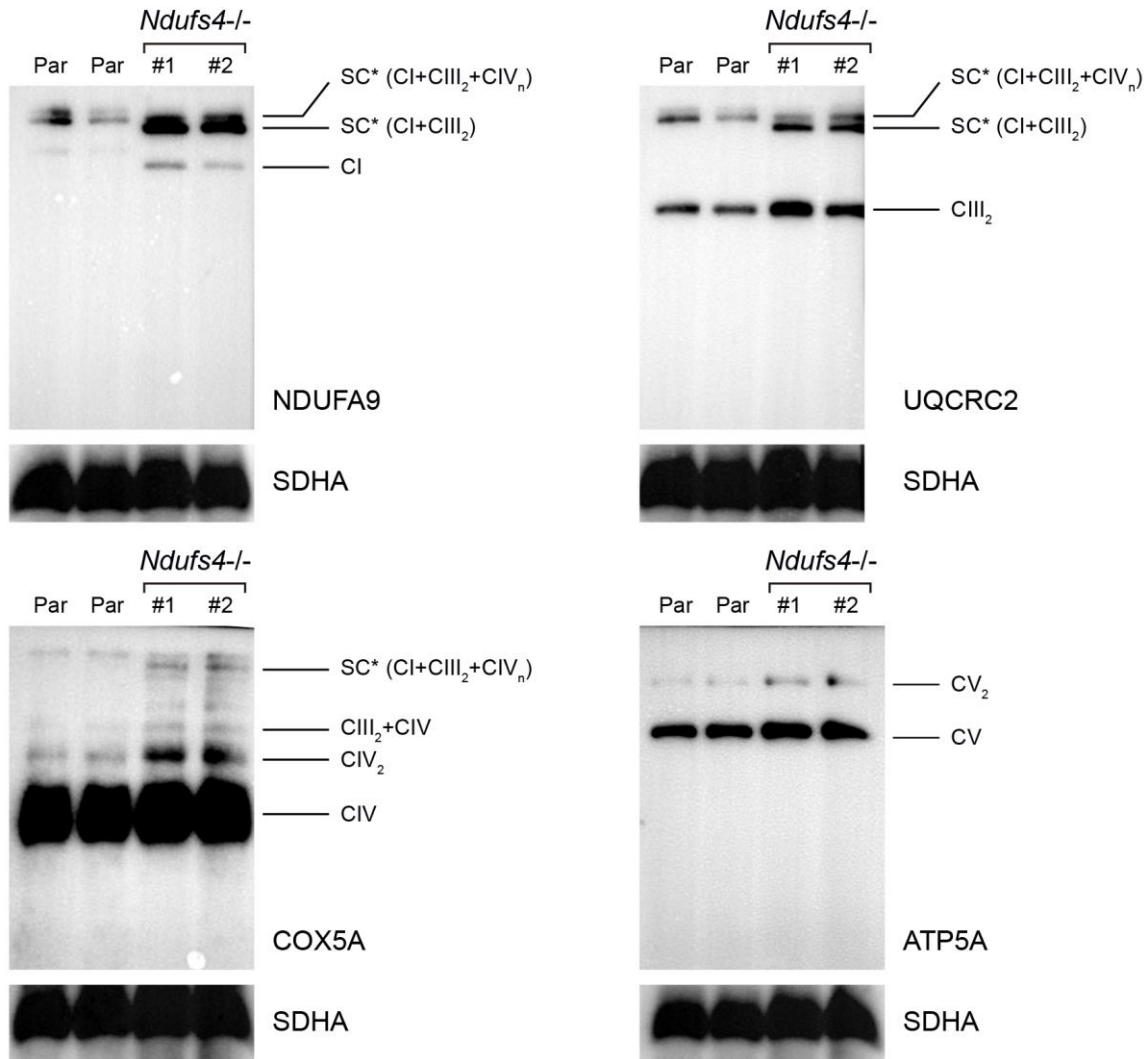


Figure 32: Respirasome assembly in *Ndufs4*^{-/-} macrophages. 1D-BNE showing OXPHOS complexes I to IV (CI-CIV) and SCs. Western blot analysis was performed using antibodies against CI (NDUFA9), CIII (UQCRC2), CIV (COX5A), and CV (ATP5A). Asterisks (*) indicate lower molecular weight SC. Loading control, CII subunit SDHA.

6. CI Activity assessment in *Ndufs4*^{-/-} Cells by In-Gel Activity (IGA) assay

The assessment of CI activity in *Ndufs4*^{-/-} cells was also performed using an IGA assay. The results were visualized by the appearance of purple bands in the native

gels, indicating NADH dehydrogenase activity of CI. While free CI and CI-containing SCs were visualized in mitochondrial extracts from parental cells, they were undetectable in *Ndufs4*^{-/-} cells (**Figure 33**). This demonstrated that partially assembled CI, either alone or bound to CIII, lacks in-gel enzymatic activity when *Ndufs4* is absent.

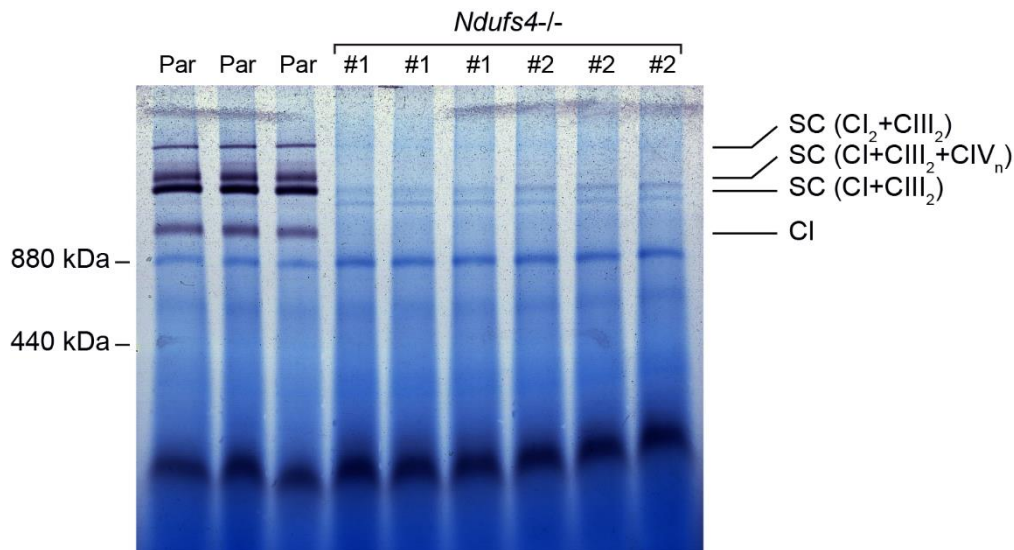


Figure 33: CI activity in *Ndufs4*^{-/-} as assessed by IGA. Native gels were incubated with NADH (as a substrate), and nitro blue tetrazolium (NBT, as the electron acceptor). CI activity is shown in purple.

7. *Ndufs4* controls macrophage effector functions

The following study was conducted to determine the effects of *Ndufs4* deficiency on macrophages, focusing on the impact of *Ndufs4* on both the expression of inflammatory mediators and the functional capacity of immune cells to respond to microbial challenges.

7.1 Impact of *Ndufs4* absence on the cytokine profile

The impact of *Ndufs4* absence on the cytokine profile of LPS-challenged macrophages was characterized by examining changes in pro-inflammatory and anti-inflammatory cytokines both at the mRNA and protein levels.

Analysis of *Ndufs4*^{-/-} cells revealed an increase in IL-6 transcript levels compared to parental cells, as shown in **Figure 34A**. The expression levels of other pro-inflammatory cytokines, such as IL-1 β and TNF- α , remained unaltered in KO cell lines. Conversely, the absence of *Ndufs4* led to a decrease in IL-10 transcripts in *Ndufs4*^{-/-} cells compared to parental cells.

Examination of cytokine protein abundance provided additional insight into the observed transcriptional changes (**Figure 34B**). IL-6 secretion by *Ndufs4*^{-/-} macrophages was found to be significantly higher than in control cells, which correlated well the increased transcript levels. IL-10 production was found to be deficient in *Ndufs4*^{-/-} macrophages, which was consistent with the observed decrease in transcript levels.

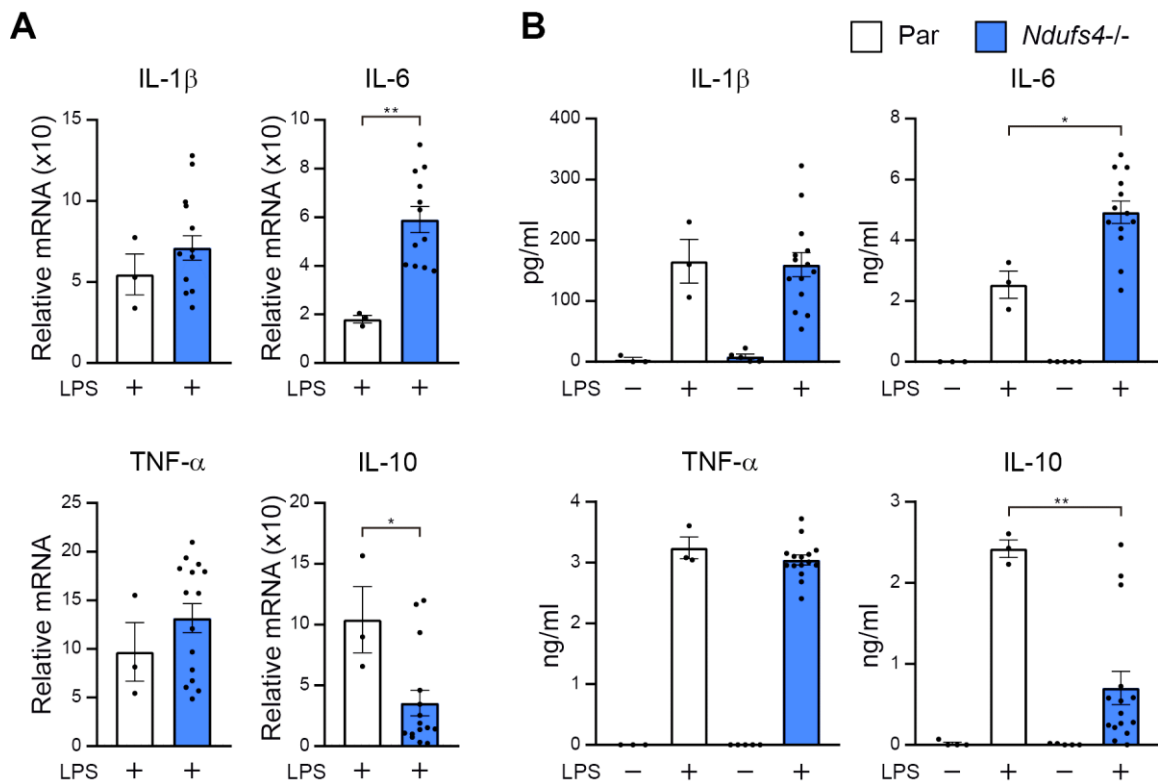


Figure 34: Cytokine profile of *Ndufs4*^{-/-} macrophages. Parental (Par) and *Ndufs4*^{-/-} RAW 264.7 cells were left untreated or treated with LPS (100 ng/ml). (A). Cells were collected 4 hours after LPS treatment for quantification of cytokine transcripts (IL-1 β , TNF- α , IL-6 and IL-10) using q-PCR, expressed as fold increases versus untreated parental cells. (B) Supernatants were collected 8 hours after LPS treatment for measurement of cytokine (IL-1 β , TNF- α , IL-6 and IL-10) concentrations by ELISA. The statistical significance is

displayed as follows: *, $P < 0.05$; **, $P < 0.01$; ***, $P < 0.005$; ****, $P < 0.001$, two-tailed t-test. Each point represents a biological replicate. Data are shown as the mean \pm SEM.

7.2 Impact of *Ndufs4* absence on phagocytic capacity

In addition to changes in cytokine expression, the phagocytic capacity of *Ndufs4*^{-/-} macrophages was investigated. This was measured by both mean fluorescence intensity (MFI) and the percentage of phagocytic positive cells (FITC+ cells). As shown in **Figure 35**, a marked increase in the phagocytosis of FITC-labeled HKEC was observed in *Ndufs4*^{-/-} cells compared to parental cells.

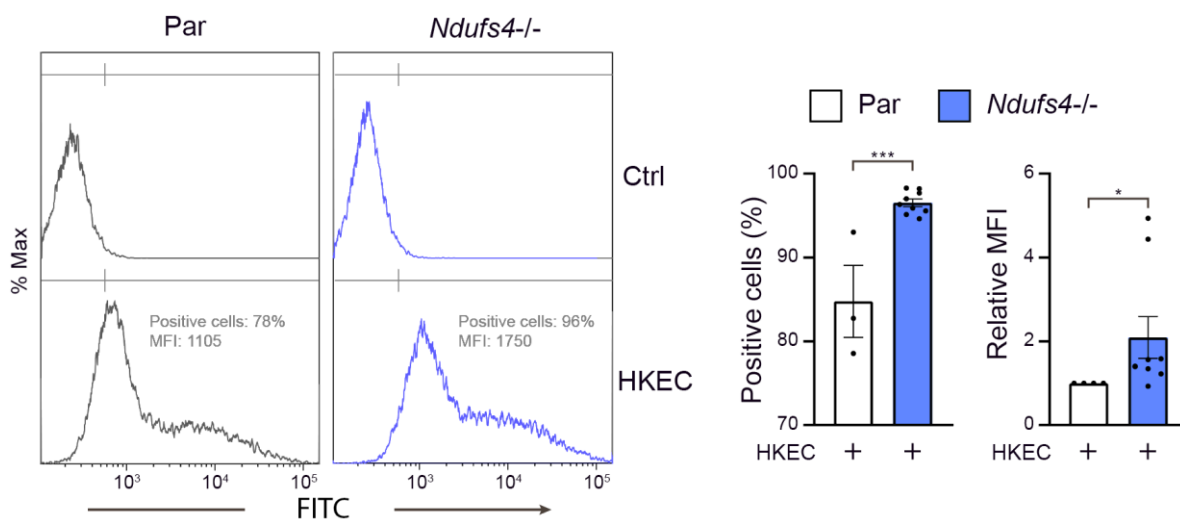


Figure 35: Flow cytometry analysis of phagocytosis of *Ndufs4*^{-/-} macrophages. Left panel: Representative flow cytometry plots showing the phagocytosis of FITC-labeled heat-killed *E. coli* (HKEC) by parental (Par), *Ndufs4*^{-/-} RAW 24.7 cells. Right panel: graph representing % of fluorescent cells and mean fluorescence intensity (MFI) values corresponding to the observed phagocytic activity. The statistical significance is displayed as follows: *, $P < 0.05$; **, $P < 0.01$; ***, $P < 0.005$; ****, $P < 0.001$, two-tailed t-test. Each point represents a biological replicate. Data are shown as the mean \pm SEM.



Chapter 3: Role of SDH/CII in macrophage respiration and effector functions

Using CRISPR/Cas9-based gene editing technology, *Sdha*^{-/-} and *Sdhb*^{-/-} RAW 264.7 murine macrophage cell lines were generated and served as the primary experimental models for this chapter, together with the use of DMM, a well-known inhibitor of CII. The *Sdha* and *Sdhb* genes are essential for the function of SDH/CII, an enzyme complex bound to the IMM which plays a significant role in both the Krebs cycle and the ETC. These genes are located on chromosomes 13 and 4 respectively, and encode two major subunits of the SDH/CII complex. The *Sdha* gene encodes the flavoprotein subunit, which harbors the catalytic site for the oxidation of succinate, while the *Sdhb* gene encodes the iron-sulfur subunit, a critical component in the electron transfer pathway.

This chapter aims to elucidate not only the immediate cellular changes induced by the absence of *Sdha* and *Sdhb*, but also the subsequent changes in downstream signaling pathways. Particular emphasis will be placed on elucidating the changes in respiratory profiles, alterations in metabolite levels and variations in effector mechanisms, including cytokine production and phagocytic capabilities, which are expected to add novel insights to the current understanding of the role of the mitochondrial ETC in macrophage biology.

1. Characterization of *Sdha*^{-/-} and *Sdhb*^{-/-} macrophages

1.1 Enzymatic activity assessment

First, CII activity was assessed in the newly generated *Sdha*^{-/-} and *Sdhb*^{-/-} macrophage cell lines. The activity was assessed by measuring electron transfer from succinate to the synthetic electron acceptor DCPIP via decylubiquinone, a

coenzyme Q10 analogue. A significant decrease in SDH/CII activity was observed in both *Sdha*^{-/-} and *Sdhb*^{-/-} macrophage cell lines (**Figure 36A**).

1.2 Succinate and fumarate levels

As the SDH enzyme catalyzes the oxidation of succinate to fumarate, it was crucial to study the levels of these metabolites as they are the substrate and the product of the enzyme, respectively. Cellular levels of these metabolites were analyzed using colorimetric assays, revealing significant changes indicative of impaired SDH/CII activity. To begin with, elevated levels of succinate were found in both *Sdha*^{-/-} and *Sdhb*^{-/-} macrophage cell lines when compared to the parental cells, as shown in **Figure 36B**. On the other hand, decreased levels of fumarate were observed in both *Sdha*^{-/-} and *Sdhb*^{-/-} macrophage cell lines when compared with the parental cells, as shown in **Figure 36B**. No significant differences were observed between *Sdha*^{-/-} and *Sdhb*^{-/-} macrophage cell lines, suggesting that free *Sdha* in *Sdhb*^{-/-} macrophages is unable to oxidize succinate.

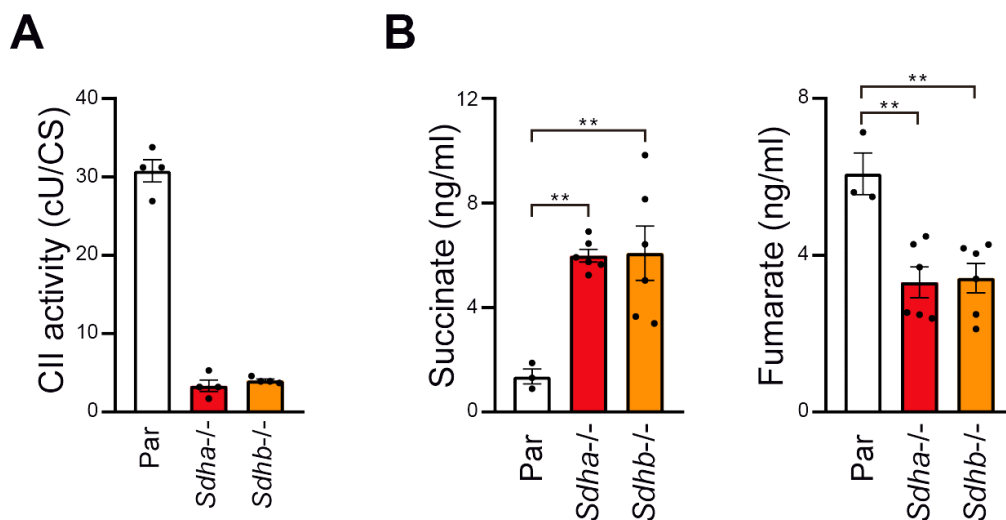


Figure 36: (A) Spectrophotometric activity of CII, normalized to citrate synthase (CS) activity, in mitochondria isolated from parental (Par), *Sdha*^{-/-}, and *Sdhb*^{-/-} RAW 264.7 cells. (B) Quantification of cellular levels of succinate and fumarate in extracts from indicated RAW 264.7 sublines. Statistical significance noted: *, P <0.05; **, P <0.01; ***, P <0.005; ****, P <0.001, ANOVA test. Each point represents a biological replicate. Data are shown as the mean \pm SEM.

1.3 Mitochondrial respiratory profile assessment

1.3.1 Basal and maximal respiration capacities

SDH/CII is not only involved in the TCA cycle through the oxidation of succinate to fumarate, but also plays a key role in the ETC. The oxidation of succinate is closely linked to the reduction of ubiquinone, a key step in mitochondrial respiration. Therefore, the effect of *Sdha* and *Sdhb* deficiency on macrophage respiration was investigated. The mitochondrial respiratory profile of both *Sdha*^{-/-} and *Sdhb*^{-/-} macrophages was analyzed, including both LPS-treated and untreated samples.

Oxygen consumption rate (OCR) was evaluated before and after the serial addition of the following specific agents: oligomycin (an ATP synthase inhibitor), FCCP (a H⁺ ionophore) and rotenone (a CI inhibitor). The results showed that, as expected, LPS-treated parental macrophages exhibited reduced basal and maximal respiratory capacities compared to untreated parental macrophages (**Figure 37**). Interestingly, a drastic reduction of basal and maximal respiratory capacities, with nearly residual values, was observed in both untreated and LPS-treated *Sdha*^{-/-} and *Sdhb*^{-/-} macrophages.

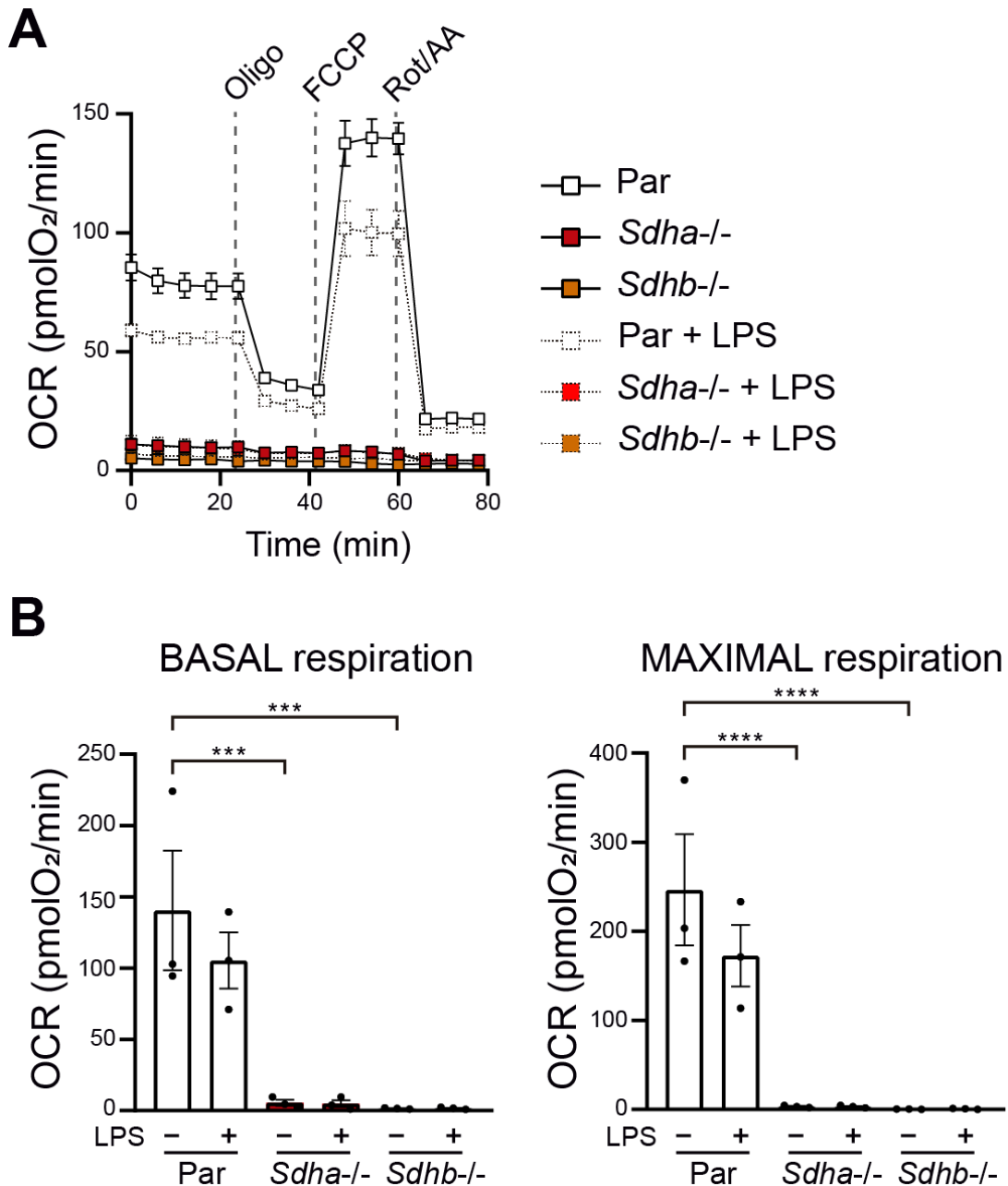


Figure 37: Evaluation of OCR in RAW 264.7 Sublines. (A) Parental (Par), *Sdha*^{-/-}, and *Sdhb*^{-/-} cells measurement of OCR under basal conditions and following the sequential addition of specific compounds: oligomycin at 2.6 μ M, FCCP at 1 μ M, and a combination of rotenone (Rot) and antimycin A (AA) at 1 μ M. (B) Graphical representation of basal respiration and maximal respiration. When indicated, cells were preincubated during 4 hours with 200 ng/mL of LPS prior to the assays. The statistical significance is displayed as follows: *, P < 0.05; **, P < 0.01; ***, P < 0.005; ****, P < 0.001, ANOVA test. Each point represents a biological replicate. Data are shown as the mean \pm SEM.

1.3.2 ATP production rate

LPS-treated parental cells exhibited increased glycolytic ATP synthesis compared to untreated parental cells, while mitochondrial ATP production was slightly decreased. In contrast, a similar analysis in mutant cells showed a halving of total ATP production relying exclusively on glycolysis, as shown in **Figure 38**, consistent with the observed respiratory changes. These findings underscore the profound impact of the absence of *Sdha* and *Sdhb* on mitochondrial respiratory profiles and energy synthesis mechanisms in macrophages.

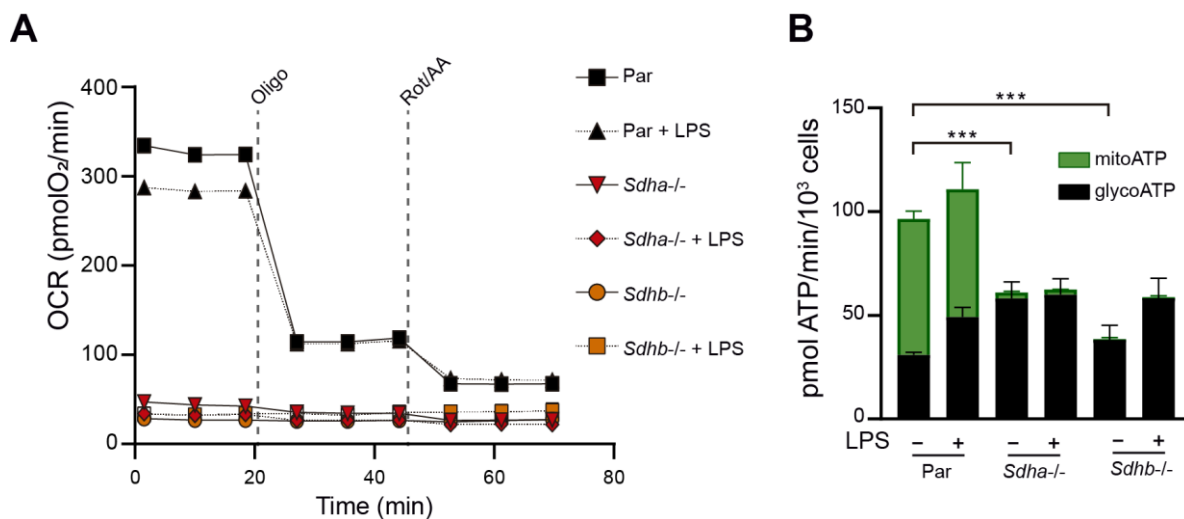


Figure 38: Quantification of ATP production in parental (Par), *Sdha*^{-/-}, and *Sdhb*^{-/-} RAW 264.7 cells using Seahorse XF real-time ATP rate assay. (A) A kinetic profile of OCR measurements. (B) Metabolic flux analysis, displaying the quantification of both mitochondrial ATP production and glycolytic ATP production. When indicated, cells were preincubated during 4 hours with 100 ng/mL of LPS prior to the assays. ATP rate values were normalized to cell number. Statistical significance noted: *, P < 0.05; **, P < 0.01; ***, P < 0.005; ****, P < 0.001, ANOVA test. Data are shown as the mean of 3 biological replicates ± SEM.

1.4 ROS production and mitochondrial dysfunction

The following assays were performed to further investigate the relationship between changes in mitochondrial respiratory profile and ROS production and mitochondrial dysfunction.

1.4.1 LPS-induced MitoROS levels

To better understand ROS dynamics in *Sdha*^{-/-} and *Sdhb*^{-/-}, the mitochondrial-specific ROS indicator, MitoSOX, was used to measure the superoxide levels within the mitochondria of living cells. It was observed that the basal levels of mitoROS were significantly elevated in *Sdha*^{-/-} and *Sdhb*^{-/-} macrophages compared to the parental control cells (**Figure 39**). Upon stimulation with LPS, an increase in mitoROS was observed in both parental and KO cells. Notably, the increase in mitoROS after LPS stimulation was comparable between *Sdha*^{-/-} and *Sdhb*^{-/-} macrophages, indicating that deletion of either subunit had a similar effect on mitoROS levels. These results suggest that SDH/CII may not be a major contributor to mitoROS production in LPS-activated macrophages. However, this observation could be potentially eclipsed by the pronounced mitoROS production resulting from mitochondrial dysfunction or its synthesis via alternative pathways outside of the ETC.

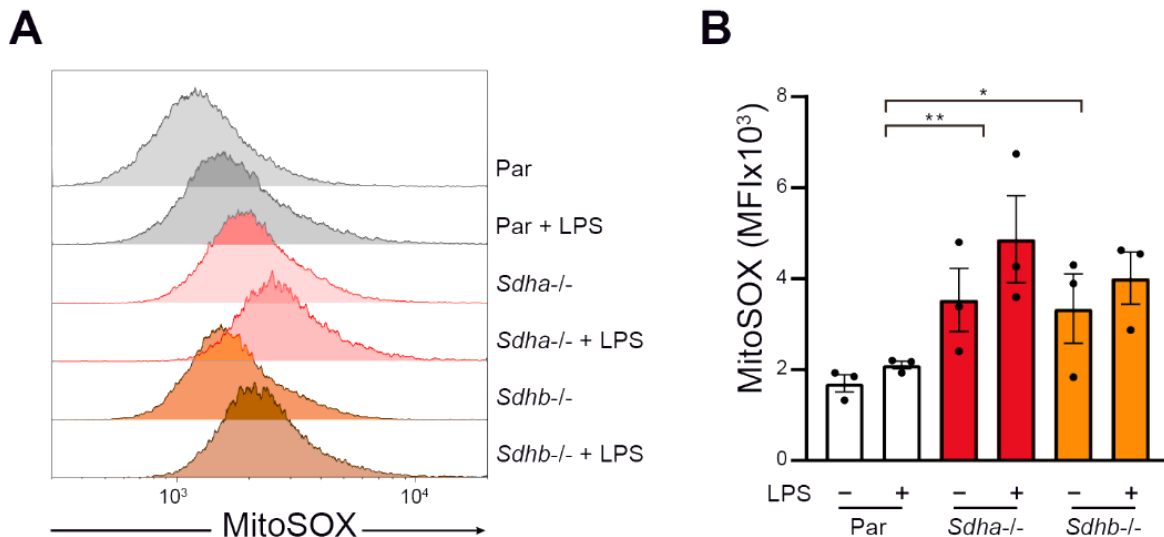


Figure 39: (A) Representative flow cytometry histograms of MitoSOX staining. (B) Graph showing mean fluorescence intensity (MFI) values corresponding to the observed mitochondrial ROS levels in parental (Par), *Sdha*^{-/-}, and *Sdhb*^{-/-} RAW 264.7 cells. When indicated, cells were preincubated during 30 minutes with 100 ng/mL of LPS prior to the assays. Statistical significance noted: *, P <0.05; **, P <0.01; ***, P<0.005; ****, P<0.001, ANOVA test. Each point represents a biological replicate. Data are shown as the mean \pm SEM.

1.4.2 Dysfunctional mitochondria

With regard to mitochondrial integrity, a dual-staining approach using MitoTracker Green (a mitochondrial mass dye) and MitoTracker Red (a potential-dependent dye) was used to determine the percentage of dysfunctional mitochondria. Both untreated and LPS-treated *Sdha*^{-/-} and *Sdhb*^{-/-} macrophages showed an increased presence of dysfunctional mitochondria, characterized by high MitoTracker Green and low MitoTracker Red signals (**Figure 40**).

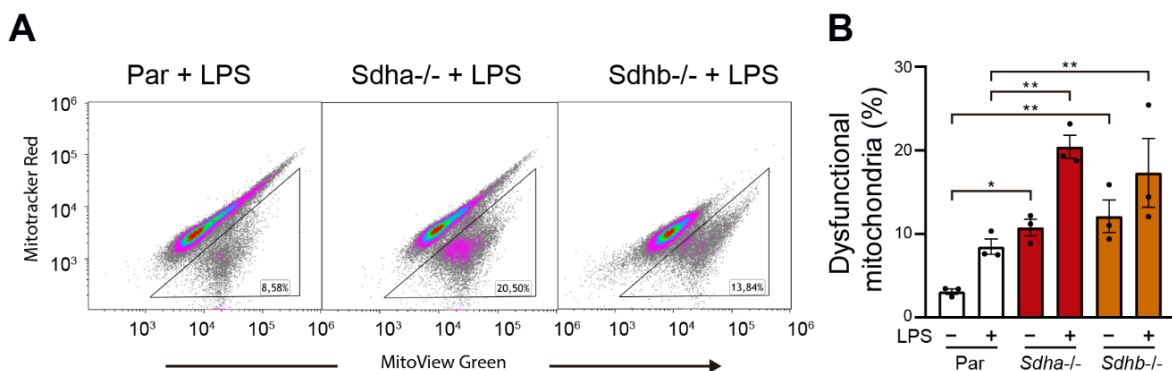


Figure 40: Mitochondrial dysfunction assay in *Sdha*^{-/-} and *Sdhb*^{-/-} cells. (A) Representative flow cytometry plots displaying the gating strategy for identifying cells with MitoTracker Green-high and MitoTracker Red-low staining, indicative of dysfunctional mitochondria. (B) Graph illustrating the percentage of dysfunctional mitochondria within parental (Par), *Sdha*^{-/-}, and *Sdhb*^{-/-} RAW 264.7 cells samples. When indicated, cells were preincubated during 30 minutes with 100 ng/mL of LPS prior to the assays. The statistical significance is displayed as follows: *, P <0.05; **, P <0.01; ***, P<0.005; ****, P<0.001, ANOVA test. Each point represents a biological replicate. Data are shown as the mean ± SEM.

1.5 Effect of *Sdha* and *Sdhb* deficiency on macrophage proliferation

Clear differences were observed when comparing the proliferation rate between the parental and the gene-deficient strains. Both *Sdha*^{-/-} and *Sdhb*^{-/-} macrophages showed a reduced proliferative rate compared to the parental cells (**Figure 41**). At 72 hours in cultured, the total number of KO cells was only approximately 30% of the values of parental cells, indicating that the deficiency in these two proteins has a dramatic negative effect on cell proliferation capacity.

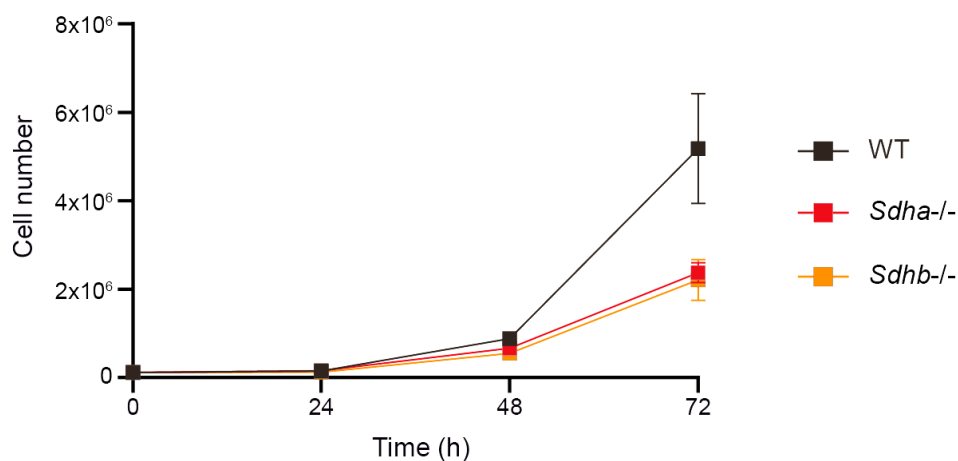


Figure 41: Effect of SDH/CII absence in macrophage proliferation. Parental, *Sdha*^{-/-} and *Sdhb*^{-/-} RAW 264.7 cells (120.000) were plated on 6-well plates. The number of viable cells was determined via Trypan blue staining at 0, 24, 48, and 72 h. Data are shown as the mean of 3 biological replicates \pm SEM

2. Role of SDH/CII in cytokine response

Cytokine secretion is pivotal to the inflammatory response of macrophages and plays a significant role in pathogen clearance, tissue repair, and modulation of immune responses. As alterations in mitochondrial proteins can significantly affect cellular metabolism and subsequent cellular functions, the role of *Sdha* and *Sdhb* in modulating cytokine responses upon stimulation becomes highly relevant. LPS stimulation was used to mimic bacterial infection in macrophages and trigger an array of cellular responses, including changes in cytokine secretion.

2.1 Genetic ablation of *Sdha* and *Sdhb* modulates cytokine response

First, the influence of genetic ablation of *Sdha* and *Sdhb* subunits on the cytokine secretion profile of macrophages was explored. *Sdha*^{-/-} or *Sdhb*^{-/-} cells exhibited a marked decrease in the secretion of IL-1 β after LPS-stimulation when compared to their parental cell counterparts (**Figure 42**). Intriguingly, this dampened secretion of IL-1 β was particularly more pronounced in *Sdhb*^{-/-} macrophages relative to the *Sdha*^{-/-} macrophages. In addition to these observations, qPCR data revealed a concomitant decrease in the expression of IL-1 β mRNA after LPS treatment. The differences between the KO lines were more pronounced for IL-1 β transcript expression than those observed for IL-1 β protein secretion.

Despite the alterations in IL-1 β secretion patterns, no significant alterations were observed in the secretion levels of other pro-inflammatory cytokines studied. Secretion levels of IL-6, IFN- β , and TNF- α were found to be similar in parental, *Sdha*^{-/-}, and *Sdhb*^{-/-} macrophages (**Figure 42**). Therefore, genetic ablation of *Sdha* and *Sdhb* appears to selectively affect both the secretion and transcription levels of IL-1 β , while leaving the secretion of other pro-inflammatory cytokines unaltered.

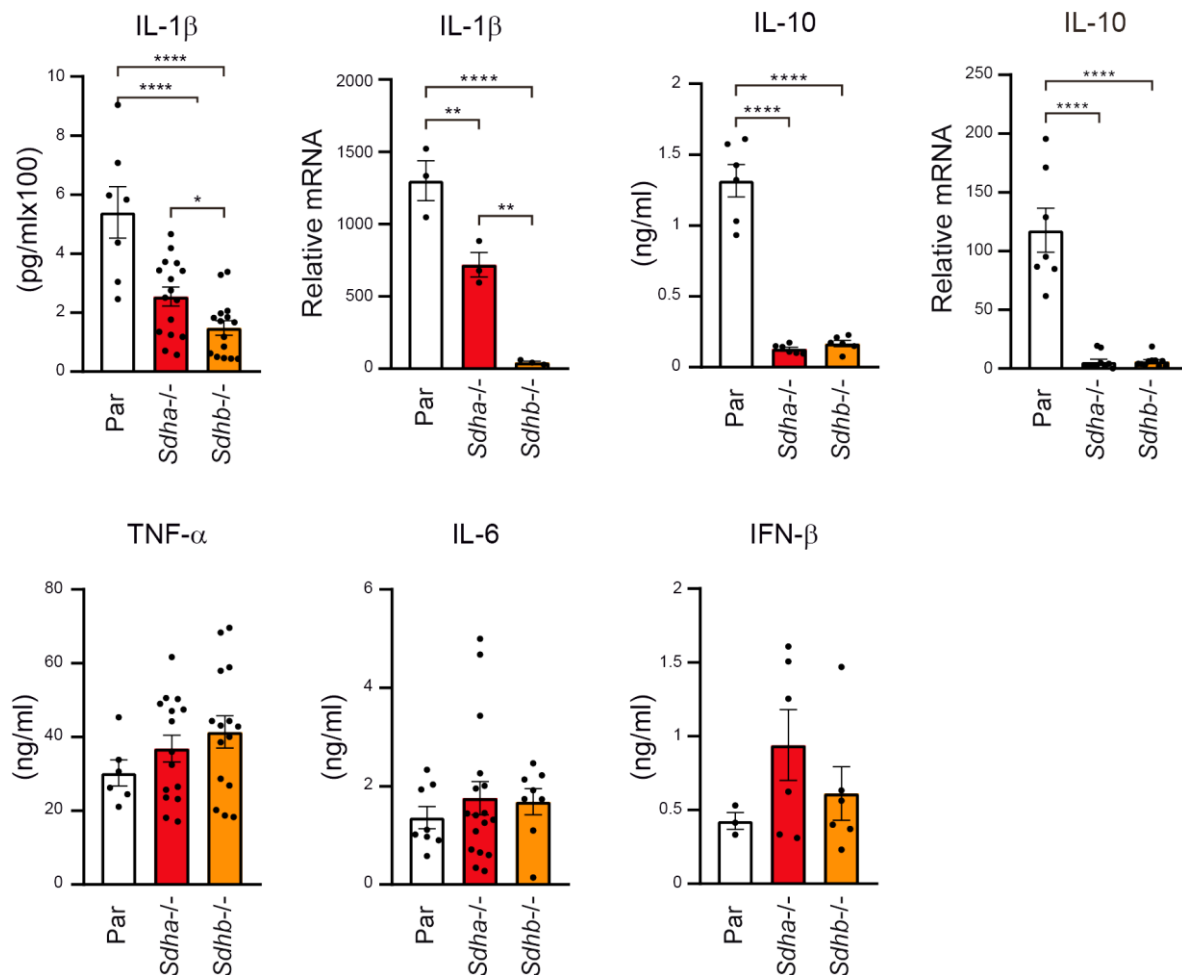


Figure 42: Cytokine profile of CII KO RAW 264.7 cell. Parental (Par), *Sdha*^{-/-}, and *Sdhb*^{-/-} RAW 264.7 cells were either left untreated (control, ctrl) or treated with LPS (100 ng/ml). Cells were collected 4 hours after LPS treatment for IL-1 β mRNA quantification by q-PCR, expressed as fold increases versus untreated parental cells. Supernatants were collected 8 hours after LPS treatment for cytokine measurements (IL-1 β , TNF- α , IL-6, and IL-10) by ELISA. Statistical significance noted: *, P < 0.05; **, P < 0.01; ***, P < 0.005; ****, P < 0.001, ANOVA test. Each point represents a biological replicate. Data are shown as the mean \pm SEM.

The anti-inflammatory cytokine IL-10 showed a limited secretion and was almost undetectable in the supernatants from LPS-activated *Sdha*^{-/-} and *Sdhb*^{-/-} macrophages (**Figure 42**). This effect was also observed in the expression of IL-10 mRNA after LPS treatment. Such a significant reduction in IL-10 levels suggests a critical role *Sdha* and *Sdhb* genes might play in the regulation of anti-inflammatory responses in macrophages.

2.2 The effect of pharmacological inhibition of *Sdha* on macrophage cytokine production

In addition to genetic approaches, pharmacological treatment with inhibitors, such as the competitive SDHA inhibitor DMM, offers an alternative strategy for understanding the role of CII in cell function. Additional experiments using DMM were proposed to determine the acute effects of *Sdha* inhibition on macrophage cytokine production.

As expected, experiments using DMM revealed its suppressive effect on IL-1 β , with a significant reduction in IL-1 β mRNA expression upon LPS treatment in both RAW 264.7 cell line and BMDMs (**Figure 43**). This effect was also observed in subsequent production and secretion of protein to the supernatant. However, the secretion of TNF- α was not affected by DMM.

Treatment with DMM also resulted in a decrease in IL-10 mRNA expression in LPS-treated BMDM. As an extension of the study, a long-term treatment with DMM was performed over a period of seven days. The results seemed to show a more pronounced decrease in IL-10 mRNA expression and protein secretion compared to a one-hour pretreatment. The duration of exposure to DMM therefore appears to have an effect on IL-10 levels, suggesting time-dependent metabolic adaptations as another underlying mechanism.

The cytokine profile in DMM-treated RAW 264.7 cells was also similar to that observed in DMM-treated BMDMs, confirming the use of RAW 264.7 cells as a reliable model for studying cytokine responses (**Figure 43**). It is worth noting that the deficient production of IL-10 in *Sdha*^{-/-} and *Sdhb*^{-/-} cells was much more severe

compared to the moderate decrease in IL-10 secretion by pharmacological intervention in BMDMs and parental RAW 264.7 cells.

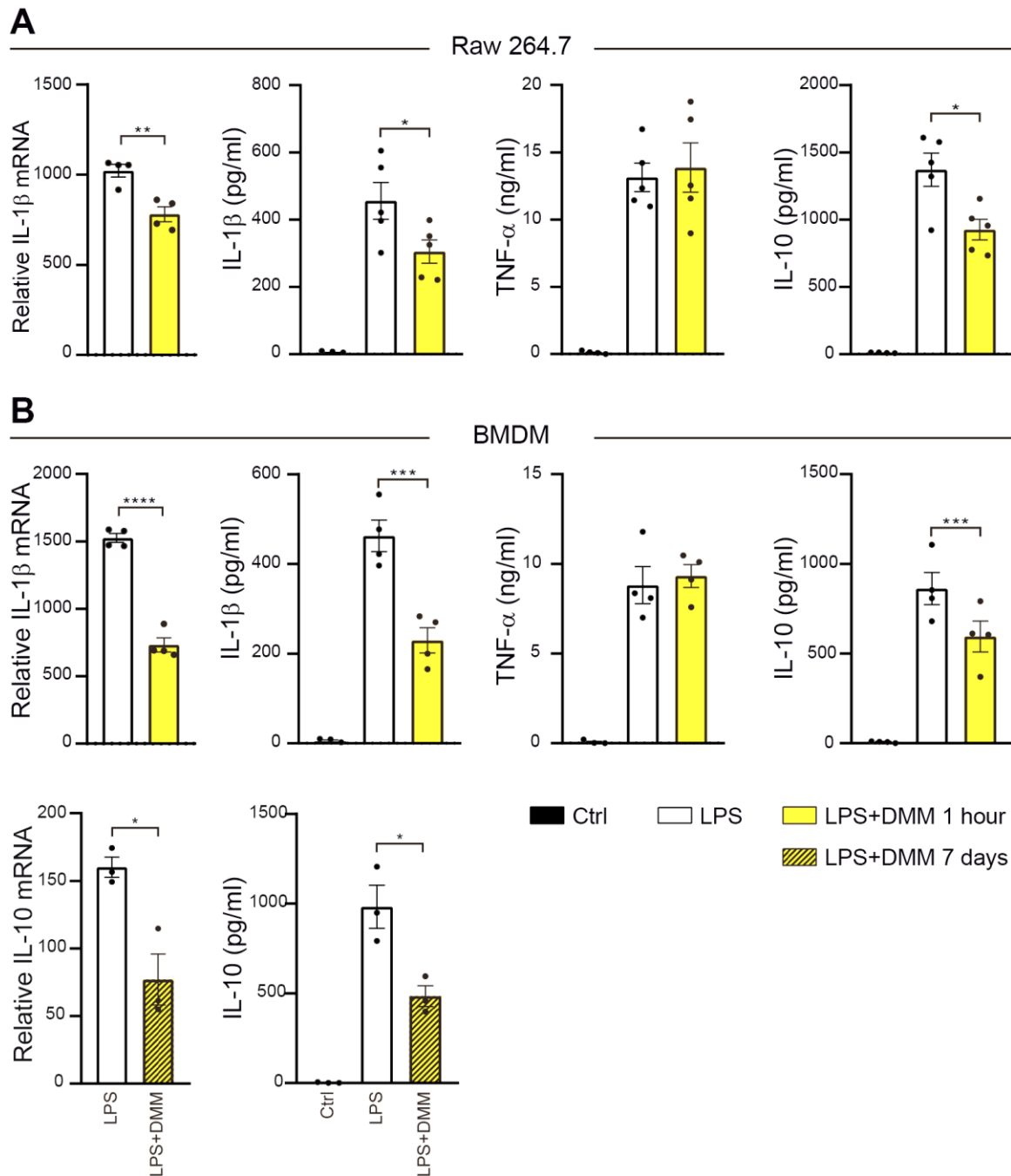


Figure 43: Cytokine profile of DMM treated cells. (A) Parental (Par) RAW 264.7 and (B) BMDMs cells were left untreated (control, ctrl) or treated with LPS (100 ng/ml). When indicated, cells were pretreated with DMM (16 mM) 1 hour before LPS stimulation. Cells were collected at 4 hours for IL-1 β and IL-10 mRNA quantification by q-PCR (expressed as fold increases vs. untreated parental cells). Supernatants were collected at 8 hours for cytokines (IL-1 β , TNF- α , and IL-10) measurements by ELISA. Impact of prolonged treatment

with *Sdha* inhibitor DMM on IL-10 production by BMDMs is shown. BMDMs were left untreated or treated with DMM (16 mM) for 7 days before LPS stimulation (100 ng/ml). Cells were collected at 4 hours after LPS for IL-10 mRNA quantification (expressed as fold increases vs. untreated cells), and supernatants were collected at 8 hours for IL-10 measurement by ELISA. The statistical significance is displayed as follows: *, $P < 0.05$; **, $P < 0.01$; ***, $P < 0.005$; ****, $P < 0.001$, ANOVA test. Each point represents a biological replicate. Data are shown as the mean \pm SEM.

To address whether the differences in IL-10 secretion were associated with varying degrees in mitochondrial respiratory capacities, we investigated the effects of DMM on RAW 264.7 cell respiration. Dose-response experiments, based on established effective concentrations of DMM to inhibit CII in macrophages^{104,107,119}, demonstrated a dose-dependent DMM-induced respiratory inhibition. OCR was significantly decreased under all experimental conditions (**Figure 44**). However, the degree of respiratory inhibition in DMM-treated cells was not as pronounced as in *Sdha*- and *Sdhb*-deficient cells (**Figure 37**). This difference in the degree of respiratory inhibition between the DMM-treated cells and the KO cells might explain the difference in the ability of these cells to produce the anti-inflammatory cytokine IL-10.

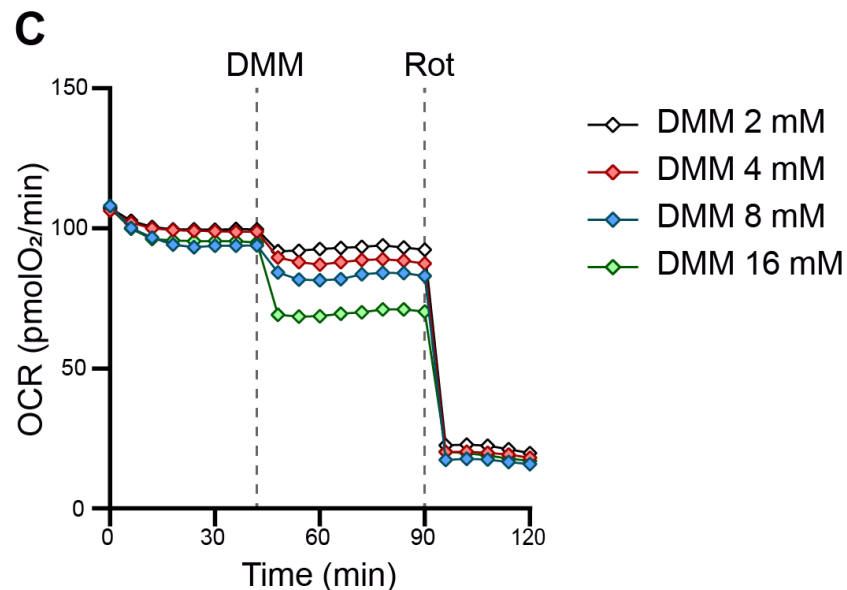


Figure 44: Effect of DMM on OCR in RAW 264.7 cells. Evaluation of OCR under basal conditions, followed by sequential introduction of DMM at specific concentrations as indicated, and the subsequent administration of rotenone (Rot) at a concentration of 1 μ M.

3. NO production

Macrophages represent a major source of the anti-inflammatory cytokine IL-10, and macrophages themselves respond to IL-10 in an autocrine manner^{120,121}. In fact, IL-10 is a known regulator of multiple macrophage effector functions, including the limitation of NO production, thus preventing NO-mediated suppression of OXPHOS²⁹. This is particularly relevant given the central role of NO as a mediator of macrophage antimicrobial and antitumor activities.

Figure 45A shows that *Sdha*^{-/-} and *Sdhb*^{-/-} macrophages expressed higher levels of iNOS compared to their parental lines after being stimulated with LPS. The increase in iNOS expression correlated with greater nitrite accumulation in the supernatants of the mutant cell lines, indicating increased NO production (**Figure 45B**). The considerable increase in NO production in these genetically modified cells, compared to the noticeable lack of IL-10 secretion, supports the link between autocrine IL-10 regulation and NO-mediated effects on mitochondrial respiration. However, the elevated iNOS levels in *Sdha* and *Sdhb* KO macrophages were only minimally dampened by IL-10 treatment (**Figure 45C**). The limited responsiveness to IL-10 suggests that SDH may be critical for the effective signaling via IL-10 receptor (IL-10R).

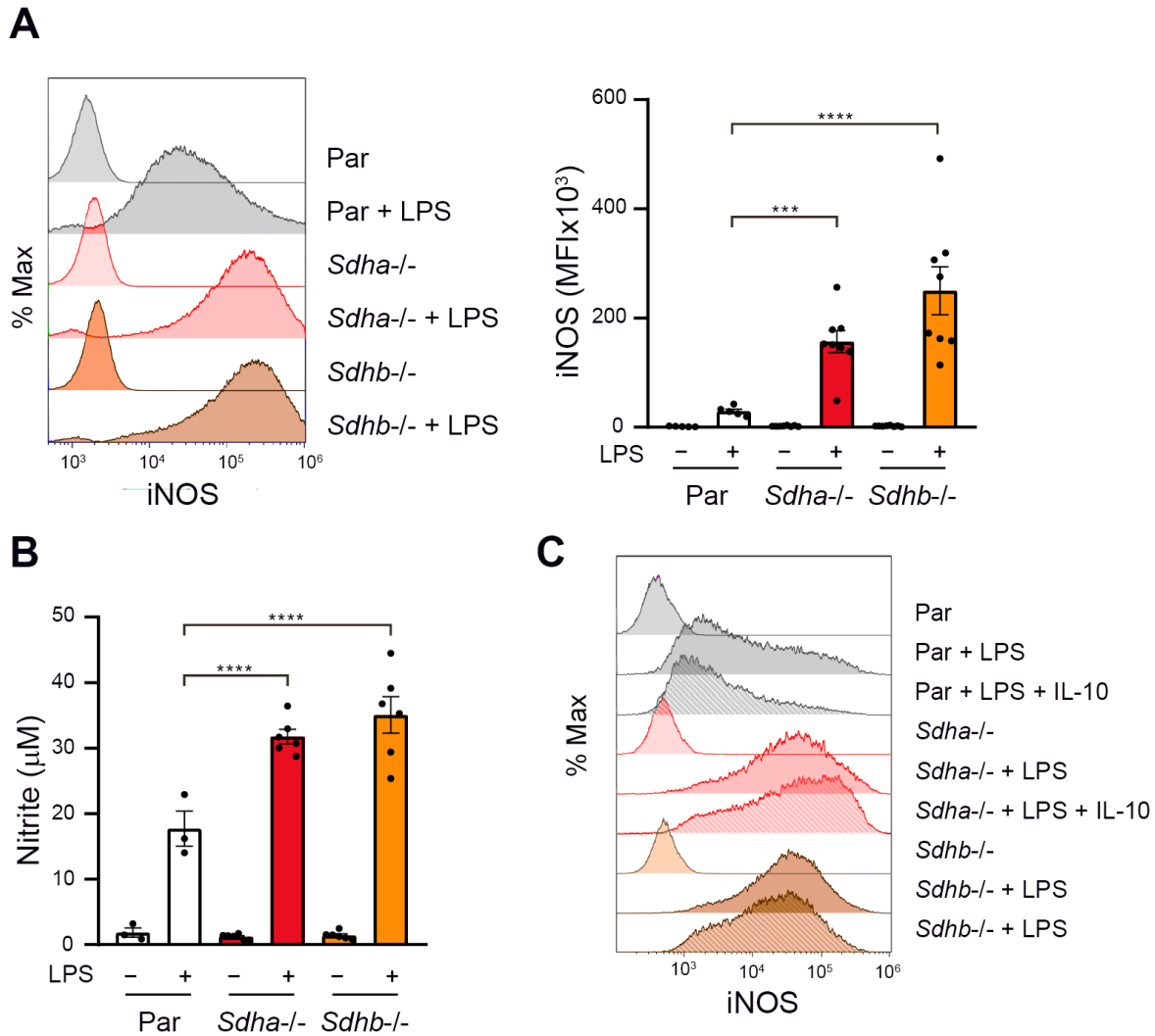


Figure 45: Examination of the role of *Sdha* and *Sdhb* in macrophages NO production. (A) Left panel shows representative flow cytometry histograms of inducible nitric oxide synthase (iNOS) staining; Right panel shows the corresponding iNOS mean fluorescence intensity (MFI) values. (B) Nitrite concentrations in the supernatants were quantified using the Griess assay; parental (Par), *Sdha*^{-/-}, and *Sdhb*^{-/-} RAW 264.7 cells either left untreated or treated with LPS at 100 ng/ml for a duration of 24 hours. (C) Additional flow cytometry histograms illustrate iNOS staining in parental, *Sdha*^{-/-}, and *Sdhb*^{-/-} RAW 264.7 cells. These cells were either untreated, treated solely with LPS (100 ng/ml), or co-treated with LPS and IL-10 at 10 ng/ml for 24 hours. Statistical significance noted: *, P < 0.05; **, P < 0.01; ***, P < 0.005; ****, P < 0.001, ANOVA test. Each point represents a biological replicate. Data are shown as the mean ± SEM.

4. Phagocytosis and bactericidal activity of macrophages without SDH/CII

To better understand the macrophage effector functions dependent on SDH/CII activity, macrophage phagocytic capacity and bactericidal activities were investigated. This was done to determine whether genetic changes associated with SDH/CII deficiency can lead to functional changes that directly impair macrophage ability to fight against bacterial infections.

4.1 Phagocytic activity

The phagocytic potential of the different macrophage sublines was assessed quantitatively by determining their capacity to engulf fluorescently labelled *E. coli* bacteria. The *Sdha*^{-/-} and *Sdhb*^{-/-} macrophages showed a significant increase in their ability to engulf bacteria compared to their parental counterparts, as evidenced by the mean fluorescence intensity data, which indicated a significant increase in the uptake of bacteria by these macrophage sublines (**Figure 46**). The results suggest that genetic ablation of SDH/CII might have primed the macrophages in a way that enhances their phagocytic potential.

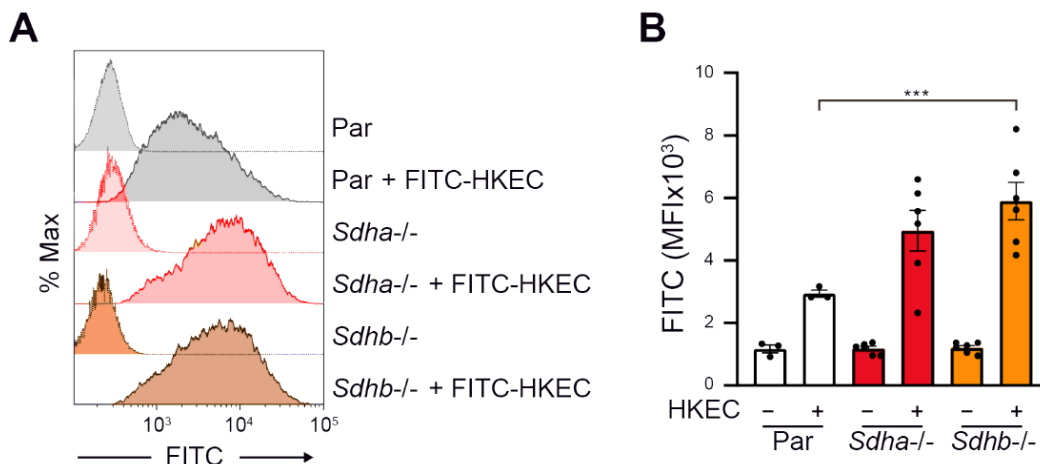


Figure 46: Flow Cytometry Analysis of Phagocytosis. (A) Flow cytometry plots showing the phagocytosis of FITC-labeled heat-killed *E. coli* (HKEC) by parental (Par), *Sdha*^{-/-} and *Sdhb*^{-/-} RAW 24.7 cells. (B) Graph that represents the mean fluorescence intensity (MFI) values corresponding to the observed phagocytic activity. The statistical significance is displayed as follows: *, P < 0.05; **, P < 0.01; ***, P < 0.005; ****, P < 0.001, ANOVA test. Each point represents a biological replicate. Data are shown as the mean \pm SEM.

4.2 Bactericidal activity

Given the enhanced bacterial uptake, it was important to investigate whether this improved phagocytosis also resulted in enhanced bactericidal activity. The gentamicin protection assay was used to quantify the bactericidal activity. This is a method designed to determine the survival rate of internalized bacteria following phagocytosis.

As shown in **Figure 47**, the number of surviving *E. coli* bacteria at time point 0 was significantly higher in *Sdha*^{-/-} and *Sdhb*^{-/-} macrophages compared to the parental cells. This observation was expected, as an increase in phagocytosis would naturally lead to a higher initial bacterial count. However, as the assay progressed, it became apparent that the bactericidal activity of the *Sdha*^{-/-} and *Sdhb*^{-/-} macrophages was similar to that of the parental macrophages. Thus, there was no evidence of an increase or decrease in the ability to eliminate the internalized bacteria over time.

Taken together, the data suggest that although the absence of SDH/CII enhances bacterial uptake by macrophages, it does not confer any additional advantage or disadvantage in their bactericidal potency.

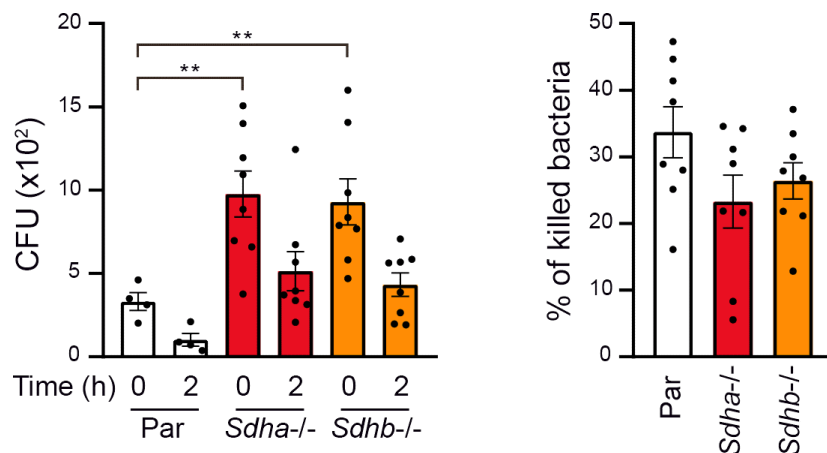


Figure 47: Assessment of Bactericidal Activity via Gentamicin Protection Assay. The left panel quantifies the colony forming units (CFU) of *E. coli* recovered at specific indicated time intervals, illustrating the kinetics of bacterial killing. The right panel provides a comparative analysis showing the relative percentage of bacterial cells killed at the 2-hour time point compared to the initial count at the 0-hour time point. The statistical significance is displayed as follows: *, $P < 0.05$; **, $P < 0.01$; ***, $P < 0.005$; ****, $P < 0.001$, ANOVA test. Each point represents a biological replicate. Data are shown as the mean \pm SEM.

5. Effects of SDH/CII deficiency on signaling pathways

The signaling pathways that could be regulated by *Sdha* and *Sdhb* were investigated. In particular, modulation of HIF-1 α levels, involvement of AMP-activated protein kinase (AMPK) and changes in STAT3 pathway were explored. This investigation aims to provide insights into the complex interplay between SDH/CII function and the intricate immune regulatory pathways.

5.1 The effect of the absence of SDH/CII on HIF-1 α levels

HIF-1 α plays a key role in cellular responses to stressors such as oxygen deprivation and energy deficiency. Even under normoxic conditions, succinate and mitoROS can drive HIF-1 α induction in macrophages. In turn, HIF-1 α plays a significant role in the production of IL-1 β . Succinate oxidation is an essential process for the induction of HIF-1 α , as demonstrated by the decrease in LPS-induced HIF-1 α expression and IL-1 β production when DMM is used¹⁰⁷.

Here, the impact of the absence of SDH on HIF-1 α was investigated. An evaluation was carried out to determine whether the absence of SDH/CII would have a similar effect on HIF-1 α levels. The results of this study showed a significant variation in HIF-1 α levels depending on the presence or absence of SDH/CII subunits. As expected from the experiments carried out with DMM, the expression levels of HIF-1 α were significantly reduced in macrophage cell lines that lacked the *Sdha* or *Sdhb* subunits (**Figure 48**). Remarkably, the reduced HIF-1 α expression correlated with decreased secretion of IL-1 β in the same cells, supporting the sequential relationship between SDH/CII function, HIF-1 α expression and pro-inflammatory cytokine secretion.

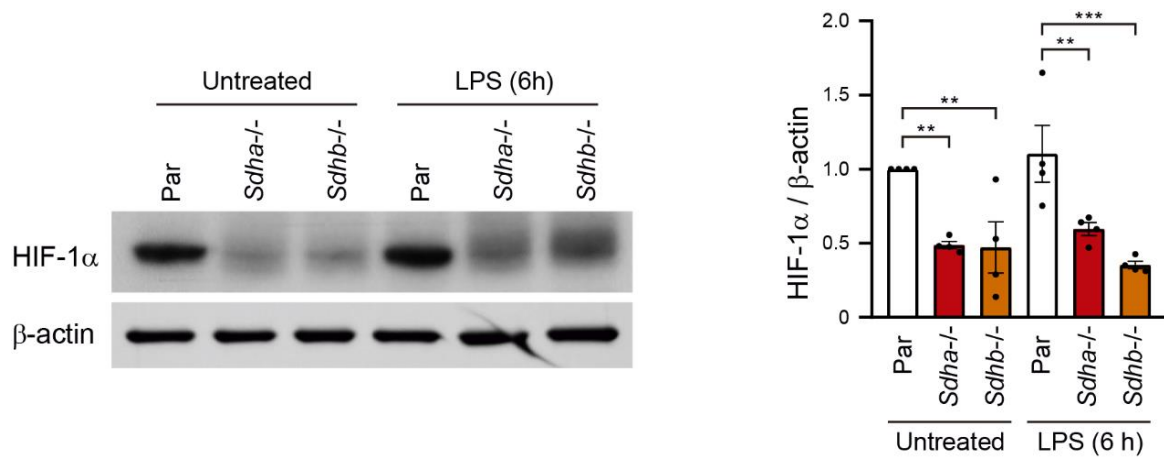
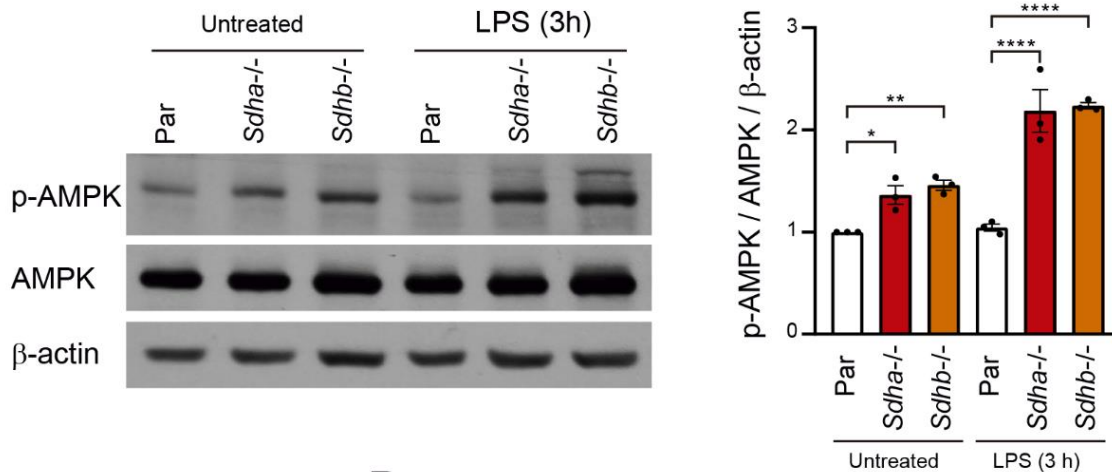


Figure 48: HIF-1 α analysis in RAW 264.7 cells. Western blot analysis of HIF-1 α and β -actin in parental (Par), *Sdha*^{-/-} and *Sdhb*^{-/-} cells incubated with LPS (100 ng/ml) at indicated times. Relative densitometric ratios displayed in right panel. Statistical significance noted: *, P <0.05; **, P <0.01; ***, P<0.005; ****, P<0.001, ANOVA test. Each point represents a biological replicate. Data are shown as the mean \pm SEM.

5.2 The role of AMPK in *Sdha*^{-/-} and *Sdhb*^{-/-} macrophages

Similar to HIF-1 α , AMPK is a well-known regulator of metabolic processes, particularly in cells that are undergoing energy starvation or specific stress conditions. The activation of AMPK occurs by phosphorylation at residue T172. The effects of the absence of SDH/CII on the activation of AMPK were examined in detail. LPS treatment induced AMPK phosphorylation in both *Sdha*^{-/-} and *Sdhb*^{-/-} cells leading to a significant increase in pAMPK levels post-treatment, as shown in **Figure 49A**. Compared to parental cells, the increased pAMPK levels in KO cells indicate a greater energy stress response in the absence of SDH/CII.

A



B

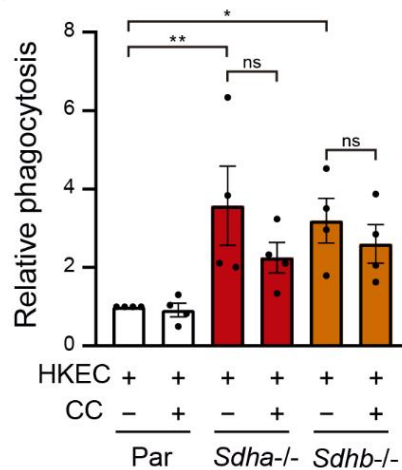


Figure 49: AMPKα analysis in RAW 264.7 cells. (A) Western blot examination of AMPKα pT172, AMPKα, and β-actin of parental (Par), *Sdha*^{-/-} and *Sdhb*^{-/-} RAW 24.7 cells post LPS incubation with LPS (100 ng/ml) at indicated times. (B) relative phagocytosis in cells incubated with Compound C (10 μM) or vehicle for 30 min prior to the phagocytosis assays. Statistical significance noted: Ns, not significant; *, P < 0.05; **, P < 0.01; ***, P < 0.005; ****, P < 0.001, ANOVA test. Each point represents a biological replicate. Data are shown as the mean ± SEM.

Considering AMPK's well-established role in regulating the phagocytic ability of immune cells, the logical next step was to investigate how the augmented AMPK activation in SDH/CII-deficient cells would underlie their increased phagocytic functions. To this purpose, compound C, a well-documented inhibitor of AMPK, was used to see if it could restore a parental phagocytic phenotype in the KO cells. Upon treatment with compound C, a slight decrease in the phagocytic activity against E.

coli was observed in *Sdha*^{-/-} and *Sdhb*^{-/-} cell lines. However, this phagocytic activity remained higher compared to the parental cell line, as shown in **Figure 49B**. These findings suggest that although AMPK phosphorylation contributes to the enhanced phagocytosis observed in the KO cells, it is not the only factor responsible for it.

5.3 Stat3 activation and altered IL-10 secretion

As previously mentioned, *Sdha*^{-/-} and *Sdhb*^{-/-} macrophages revealed a complete inability to secrete IL-10 after LPS treatment, and this decline in IL-10 secretion was accompanied by a corresponding decrease in the induction of IL-10 transcripts, as further demonstrated in **Figure 42**. IL-10 is a pivotal cytokine in the immune system due to its potent anti-inflammatory properties. Autocrine IL-10 plays an instrumental role in shaping the inflammatory status of LPS-activated macrophages, primarily through the Stat3 signaling cascade. Therefore, the Stat3 pathway was examined to determine how SDH/CII deficiency affects IL-10 dynamics and subsequent signaling.

Studies suggest that autocrine IL-10 is crucial for the phosphorylation of Stat3 at Y705 in macrophages treated with LPS. Experiments revealed that macrophages lacking IL-10 or treated with neutralizing antibodies against IL-10 or IL-10R did not undergo Stat3 Y705 phosphorylation when treated with LPS^{31,122}. The effectiveness of the 1B1.3a neutralizing monoclonal antibody has been demonstrated in preventing the phosphorylation of Stat3 at Y705 through targeting the IL-10R α subunit in RAW 264.7 parental cells, as shown in **Figure 50**.

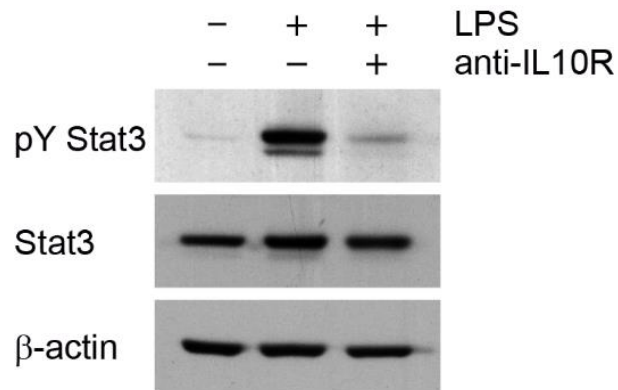


Figure 50: Effect of anti-IL-10R neutralizing antibody on tyrosine phosphorylation of Stat3 (Y705). RAW 264.7 cells were left untreated or treated with 100 ng/ml LPS. Where indicated, cells were preincubated with anti-IL10R (10 µg/ml) for 30 minutes prior to stimulation with LPS. Cells were harvested 6 hours after the addition of LPS and whole cell lysates were analyzed by Western blotting for Stat3 pY705, Stat3 and β-actin. Blots are Representative results of three independent experiments.

The activation of Stat3 is not only a result of stimulation of the IL-10 receptor. It is also involved in inducing IL-10 gene expression in macrophages and other immune cells including T and B cells. This dual role is achieved through the dimerization of Stat3, which is made possible by the reciprocal binding of its SH2 domain to the phosphorylated Y705 site. This phosphorylation event is vital for the nuclear translocation of Stat3 and its subsequent transcriptional activity.

Evaluation of the effect of SDH/CII deficiency on this pathway revealed that LPS-induced Stat3 Y705 phosphorylation, typically observed in parental RAW 264.7 cells, was severely inhibited in the *Sdha* and *Sdhb* KO lines, as shown in **Figure 51A**. The significant decrease in Stat3 pY705 levels when SDH/CII is absent highlights the potential role of this enzyme complex in regulating Stat3 activation and function.

In addition, the understanding of the modulatory role of SDH on the Stat3 signaling axis in macrophages was enlarged by experiments performed with BMDMs and DMM, an inhibitor of SDH. Specifically, BMDMs treated with DMM showed decreased Stat3 phosphorylation at the Y705 site following LPS stimulation compared to the untreated control (**Figure 51B**). This finding is consistent with the observations made in *Sdha* and *Sdhb* KO lines, thus confirming the central role of the SDH complex in regulating Stat3 activation.

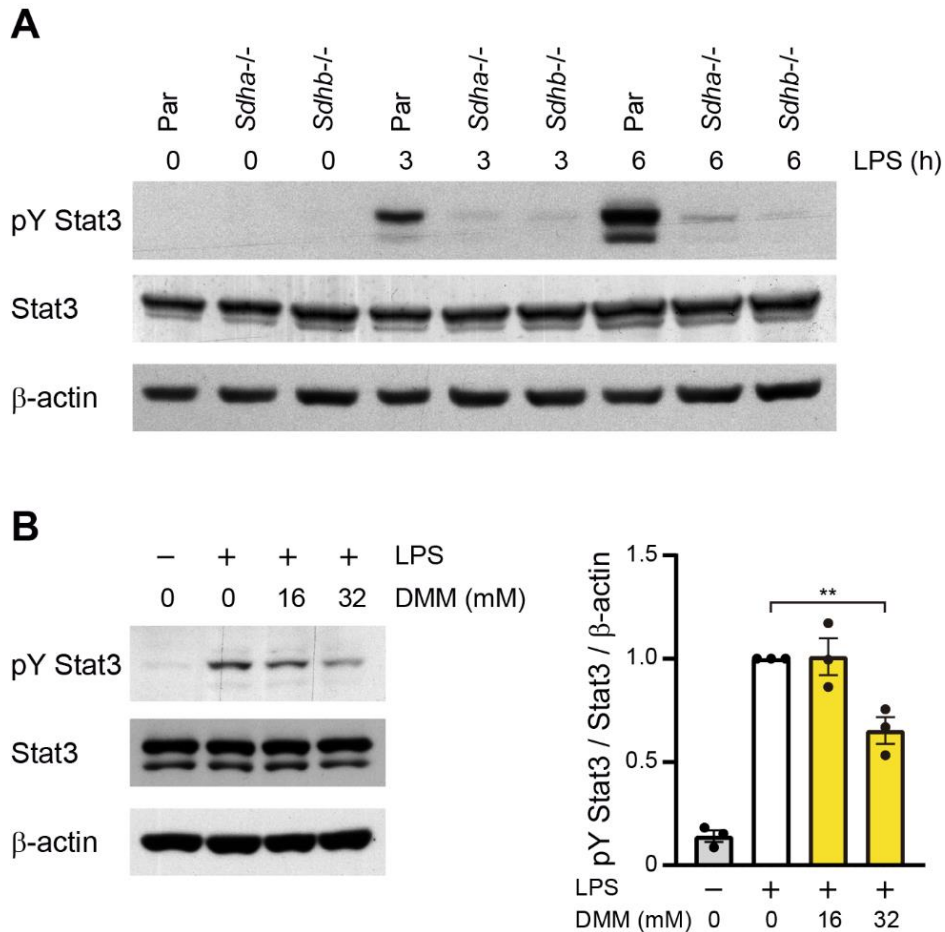


Figure 51: Role of *Sdha* and *Sdhb* in Stat3 phosphorylation. (A) Western blotting for Stat3 pY705, Stat3 and β -actin of parental (Par), *Sdha*^{-/-} and *Sdhb*^{-/-} RAW 24.7 cells treated with LPS (100 ng/ml) at indicated times. (B) Western blotting for Stat3 pY705, Stat3 and β -actin of BMDMs untreated or treated with DMM (16 mM or 32 mM) for 1 hour before stimulation with LPS (100 ng/ml) for 6 hours; relative densitometric ratios are shown in the lower right panel. Blots are Representative results of three independent experiments. Statistical significance noted: *, $P < 0.05$; **, $P < 0.01$; ***, $P < 0.005$; ****, $P < 0.001$, ANOVA test. Each point represents one biological replicate. Data are presented as mean \pm SEM.

Further experiments were conducted to investigate whether the reduced Stat3 Y705 phosphorylation was caused by the absence of IL-10 in the extracellular environment of KO cells. LPS-treated *Sdha*^{-/-} macrophages showed a partial recovery of Stat3 pY705 expression when supplemented with a high concentration (10 ng/ml) of exogenous IL-10. However, the same treatment did not produce any changes in the LPS-treated *Sdhb*^{-/-} macrophages, as described in **Figure 52A**. To determine whether IL-10 could also contribute to the modulation of Stat3 pY705 levels in *Sdha*^{-/-} macrophages at levels similar to those secreted by LPS-treated parental

cells (1 ng/ml), a further experiment was performed with varying doses of exogenous IL-10. Interestingly, the addition of IL-10 at a concentration of 1 ng/ml was found to be insufficient to restore Stat3 Y705 phosphorylation, as shown in **Figure 52B**. These results suggested that the reduced levels of IL-10 in the supernatants of LPS-treated *Sdha*^{-/-} macrophages were not the sole determinant responsible for the attenuated tyrosine phosphorylation of Stat3 in these cells.

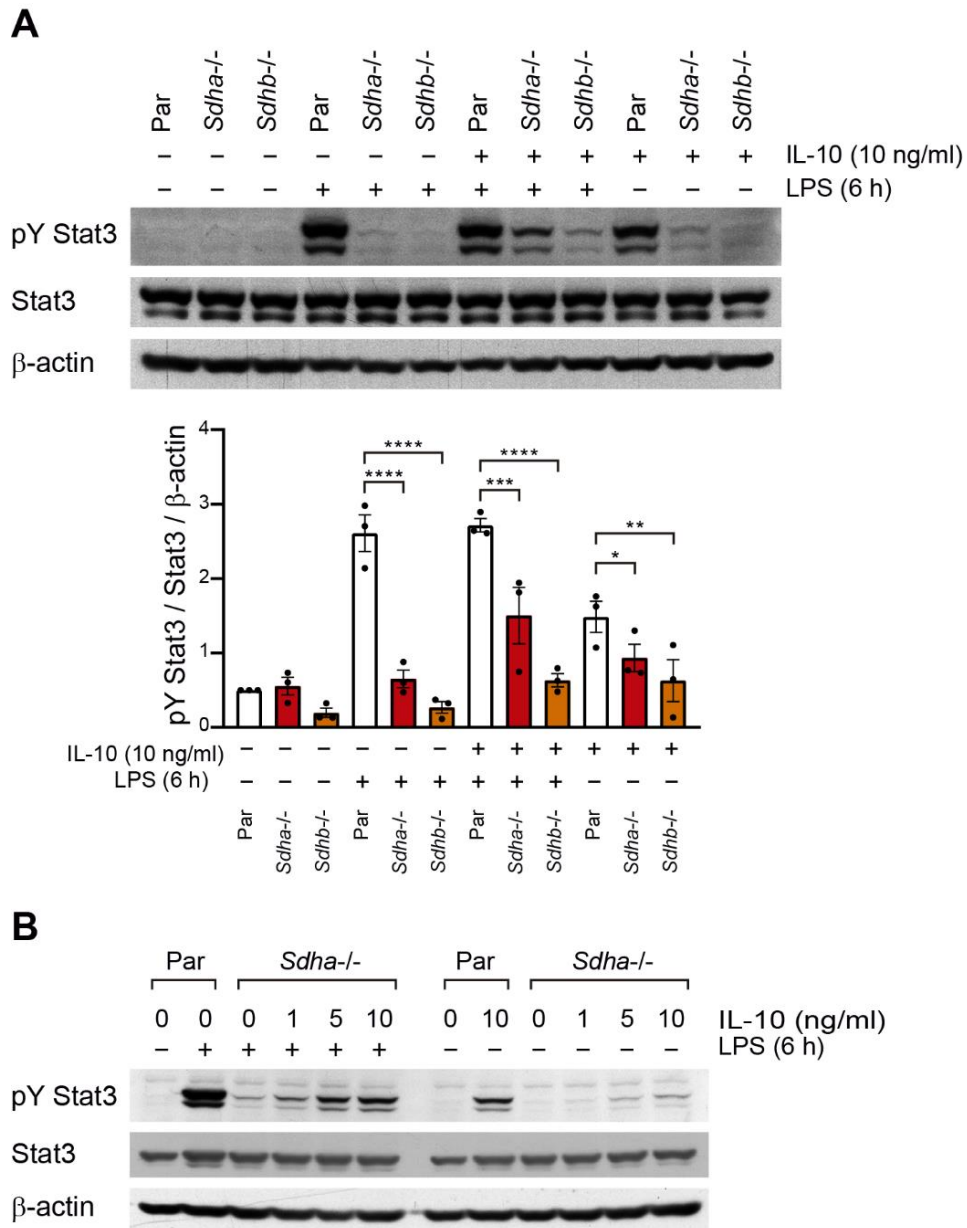


Figure 52: Autocrine effect of IL-10 in Stat3 phosphorylation. Western blot analysis of Stat3 pY705, Stat3 and β -actin. (A) Parental (Par), *Sdha*^{-/-} and *Sdhb*^{-/-} RAW 264.7 cells

were left untreated or treated with LPS (100 ng/ml) and/or IL-10 (10 ng/ml); Relative densitometric ratios displayed in bottom panel. (B) Parental (Par), *Sdha*^{-/-} RAW 264.7 cells were left untreated or treated with LPS (100 ng/ml) and/or IL-10 (1-10 ng/ml). Blots are Representative results of three independent experiments. Statistical significance noted: *, P <0.05; **, P <0.01; ***, P<0.005; ****, P<0.001, ANOVA test. Each point represents one biological replicate. Data are presented as mean ± SEM.

Furthermore, it is remarkable that in addition to its direct influence on IL-10 levels, the absence of SDH/CII manifested significant alterations in the transcripts of other anti-inflammatory Stat3 target genes, including Arg1, Socs3 and Bcl3, as shown in

Figure 53.

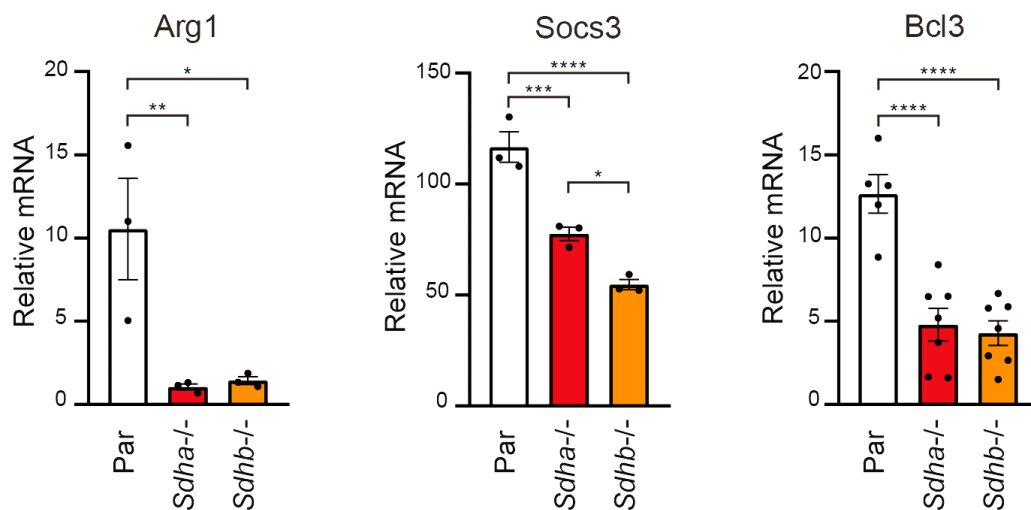


Figure 53: Role of the SDH complex in the Stat3 transcriptional program. q-PCR quantification of Arg1, Bcl3 and Socs3 mRNAs in parental (Par), *Sdha*^{-/-} and *Sdhb*^{-/-} RAW 264.7 cells treated with LPS (100 ng/ml) for 4 hours. Fold increases compared to untreated parental cells. Statistical significance noted: *, P <0.05; **, P <0.01; ***, P<0.005; ****, P<0.001, ANOVA test. Each point represents a biological replicate. Data shown as mean ± SEM.

5.4 Alternative phosphorylation of Stat3 protein

Stat3 activation can be modulated by multiple phosphorylation events. In addition to the extensively studied Y705 phosphorylation site, another important phosphorylation site is S727. In relation to transcriptional regulation, phosphorylation at the S727 site has been reported to affect the transcriptional potency of Stat3. It has been proposed that this modulation may occur through the control of interactions of Stat3 with other transcriptional cofactors. In addition, the functions of Stat3 are not limited to the nucleus. A subset of Stat3, once phosphorylated at the S727 site, can

localize to the mitochondria. Inside the mitochondria, this phosphorylated Stat3 enhances ETC activity and influences mitochondrial transcription, independent of its classical roles as a nuclear transcription factor ¹²³.

This alternative phosphorylation was also investigated to gain a better understanding of how the absence of SDH/CII affects the phosphorylation dynamics of Stat3. When LPS-induced Stat3 S727 phosphorylation was evaluated in the SDH/CII-deficient macrophages, a slight increase was observed in the *Sdha*^{-/-} and *Sdhb*^{-/-} cell lines compared to the parental macrophages. However, this increase was not significant, as shown in **Figure 54**. This observation contrasts with the pronounced decrease in Stat3 Y705 phosphorylation observed above, suggesting a differential modulation of these phosphorylation sites in response to the absence of SDH/CII. Taken together, these results indicate that while SDH/CII is critical for Stat3 phosphorylation at Y705, it does not have a modulatory role on phosphorylation at S727.

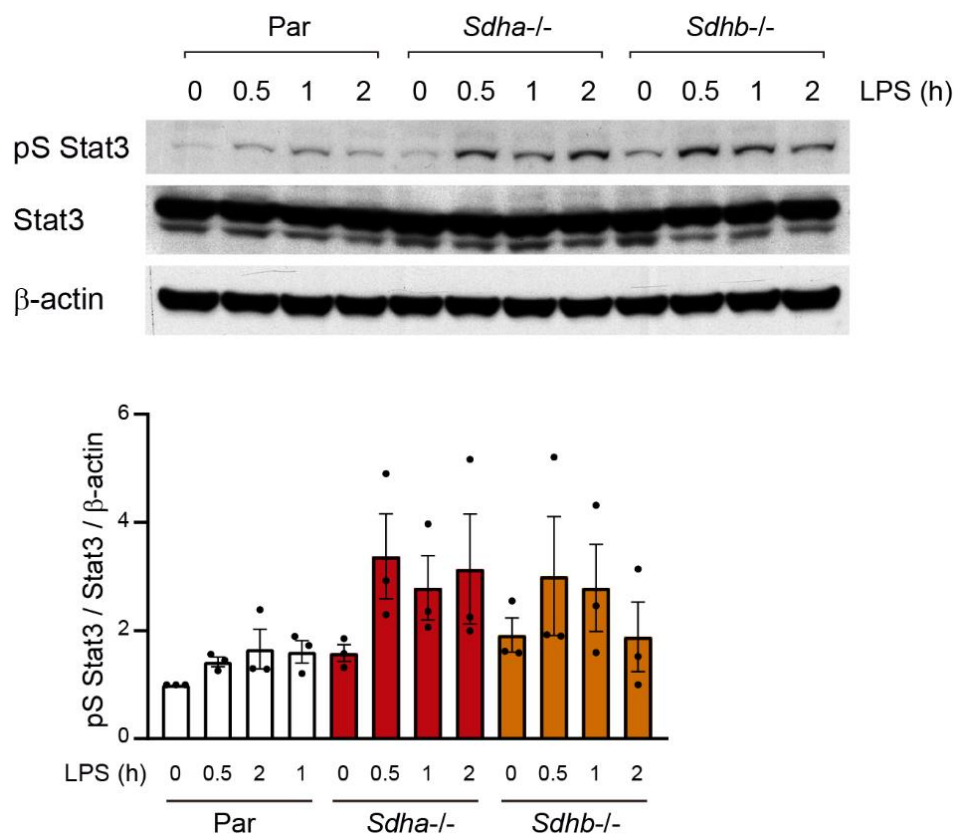


Figure 54: Role of *Sdha* and *Sdhb* in Stat3 alternative phosphorylation. Western blotting for Stat3 pY705, Stat3 and β -actin of parental (Par), *Sdha*^{-/-} and *Sdhb*^{-/-} RAW

24.7 cells treated with LPS (100 ng/ml) at indicated times; relative densitometric ratios are shown in the right panel. Blots are Representative results of three independent experiments. Each point represents one biological replicate. Data are presented as mean \pm SEM.

6. Changes in TCA metabolites in *Sdha*^{-/-} and *Sdhb*^{-/-} macrophages

The TCA cycle is at the core of cellular metabolism and serves as a central pathway linking diverse metabolic processes. In macrophages, alterations in the TCA cycle are increasingly recognized as critical players in defining cell function and phenotype. In particular, SDH/CII has emerged as a key component. Here, the changes in TCA metabolites in *Sdha*^{-/-} and *Sdhb*^{-/-} macrophages were explored as a potential link between SDH/CII and Y705 phosphorylation of Stat3.

6.1 Profiling of TCA metabolites by UPLC-MS

To gain a deeper understanding of the specific molecular aspects of this interaction, a wide-ranging profiling of TCA metabolites in both untreated and LPS-treated *Sdha*^{-/-} and *Sdhb*^{-/-} macrophages was performed using liquid chromatography technique coupled to mass spectrometry (UPLC-MS), with data presented in **Figure 55**.

Among the observations from the metabolite profile, an important finding was the marked reduction of itaconate in LPS-treated *Sdha*^{-/-} and *Sdhb*^{-/-} macrophages. Considering that itaconate is typically upregulated in LPS-activated macrophages¹²⁴, this decrease is particularly noteworthy. This decrease is likely to be attributed to the concomitant decrease in citrate levels.

Furthermore, malate levels were consistently decreased in the mutant macrophages, both under basal conditions and after LPS treatment. In contrast, there was a striking increase in succinate, which accumulated significantly in the mutant macrophages irrespective of their treatment status. In addition, an increase in lactate concentration in LPS-treated mutant macrophages indicates an enhanced glycolytic phenotype in these cells. This was accompanied by an apparent accumulation of oxaloacetate, suggesting a potential upregulation of anaplerotic pathways. Although not directly detectable in the UPLC-MS assay, the presence of

fumarate was confirmed at reduced levels in the mutant macrophages using a colorimetric assay, as shown in **Figure 36**.

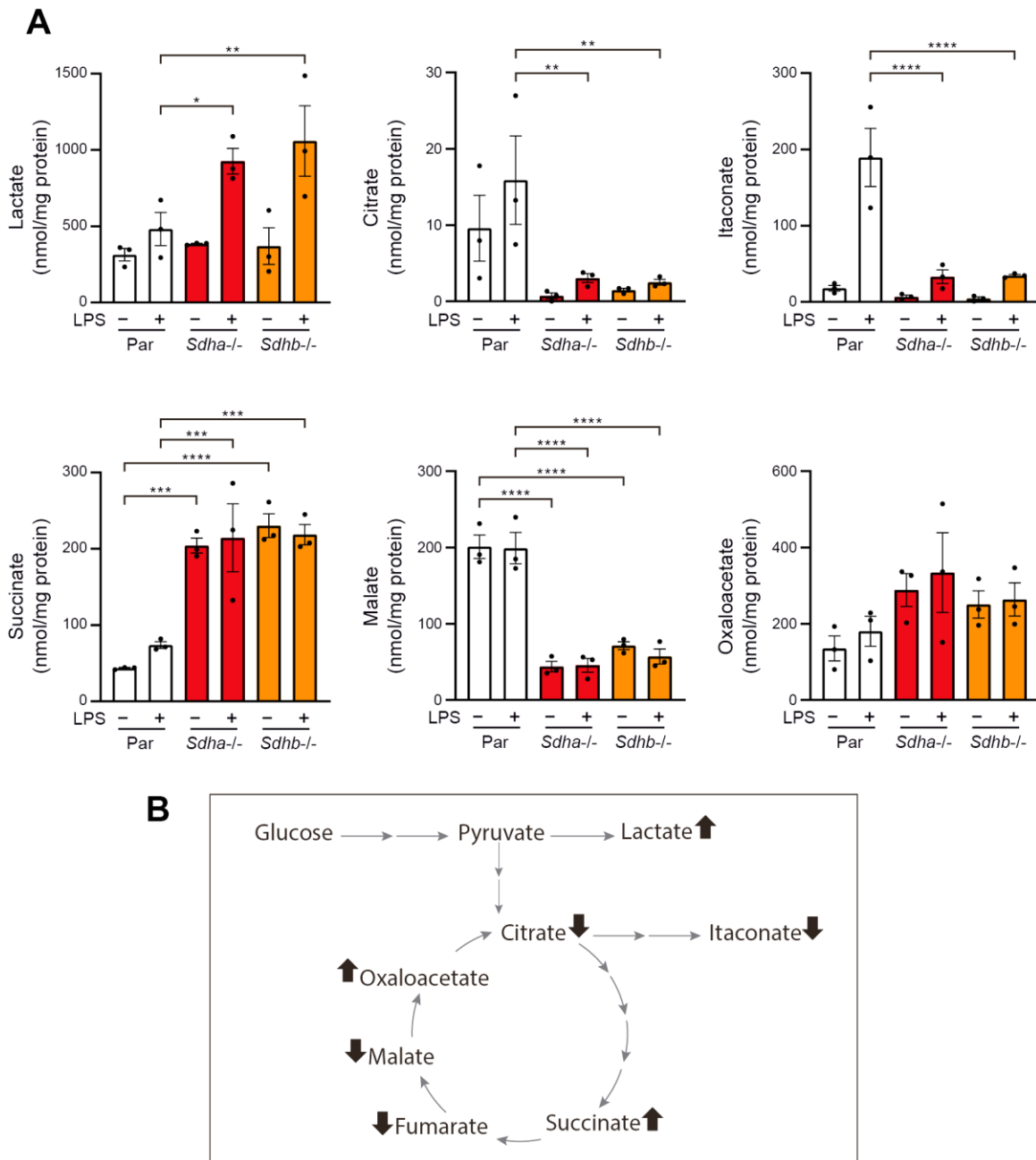


Figure 55: TCA cycle intermediates in RAW 264.7. (A) UPLC/MS analysis of lactate, citrate, itaconate, succinate, malate, and oxaloacetate from parental (Par), *Sdha*^{-/-} and *Sdhb*^{-/-} RAW 264.7 cells treated with LPS (100 ng/ml) for 24 hours. **(B)** Scheme of the effects of SDH/CII deficiency on key metabolites. Arrows show differences observed between KO and parental cells. Each point represents one biological replicate. Statistical significance noted: *, $P < 0.05$; **, $P < 0.01$; ***, $P < 0.005$; ****, $P < 0.001$, ANOVA test. Data shown as mean \pm SEM.

6.2 Impact of itaconate and fumarate on the Stat3 pY705 phenotype

The relevance of specific TCA metabolites, in particular itaconate and fumarate, as key players in the downregulation of inflammation and their potential implication in Stat3 Y705 phosphorylation was investigated. Given the reduced levels of these metabolites in *Sdha*^{-/-} and *Sdhb*^{-/-} macrophages, it was hypothesized that these metabolites could exert their influence in part through Stat3 Y705 phosphorylation. If confirmed, this association would provide a molecular basis for the observed lack of phosphorylation of Y705 in the mutant macrophages.

Mutant macrophages were treated with cell-permeable derivatives of these metabolites in order to empirically determine the potential modulatory effect of itaconate and fumarate on the pY705 phenotype. These derivatives were 4- octyl itaconate (OI) for itaconate and dimethyl fumarate (DMF) for fumarate. According to the experimental data shown in **Figure 56**, neither OI nor DMF showed efficacy in restoring the pY705 phenotype in *Sdha*^{-/-} and *Sdhb*^{-/-} macrophages. In contrast, exposure to these derivatives not only failed to rescue the pY705 phenotype in the mutant strains, but also induced a suppression of Stat3 Y705 phosphorylation in the parental macrophages upon LPS treatment. The data collected suggested two main conclusions: (i) These specific metabolites, itaconate and fumarate, play a crucial role in the regulation of Stat3 Y705 phosphorylation. (ii) The pY705 deficient phenotype observed in *Sdha*^{-/-} and *Sdhb*^{-/-} macrophages cannot be attributed to the reduced levels of itaconate and fumarate in these cells.

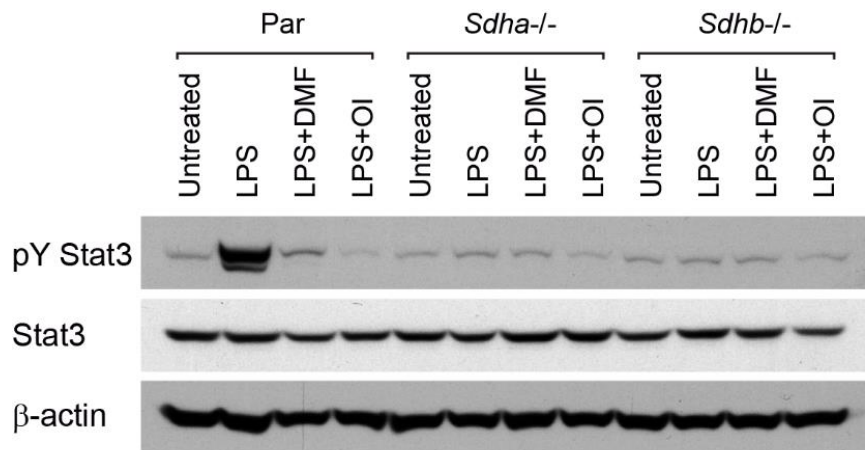


Figure 56: Effect of metabolites on Stat3 tyrosine phosphorylation in *Sdha*^{-/-} and *Sdhb*^{-/-} cells. Western blotting for Stat3 pY705, Stat3, and β -actin of parental (Par), *Sdha*^{-/-} and *Sdhb*^{-/-} RAW 24.7 cells that were left untreated or preincubated with DMF (25 μ M) and OI (125 μ M) for 3 hours before stimulation with LPS (100 ng/ml) for 6 hours. Representative results of three independent experiments.

7. MitoROS as a potential inhibitor of Stat3 Y705 phosphorylation

The influence of mitoROS on cellular processes, particularly in relation to Stat3 Y705 phosphorylation, remains a topic of considerable interest. Given the abundant evidence pointing to oxidative stress as a potent modulator of the DNA-binding and transcriptional functions of Stat3¹²⁵, the role of mitoROS in potentially inhibiting Stat3 phosphorylation at Y705 in *Sdha*^{-/-} and *Sdhb*^{-/-} macrophages was closely examined.

Previous observations, particularly in hepatoma cells, have shown that various oxidants can induce a decrease in Stat3 Y705 phosphorylation¹²⁶. Based on these observations, it was hypothesized that the lack of Stat3 Y705 phosphorylation in *Sdha*^{-/-} and *Sdhb*^{-/-} macrophages might be due to increased mitoROS levels. In order to test this hypothesis, a mitochondria-targeted ROS scavenger named mitoTEMPO was used to determine its potential efficacy in restoring the impaired Stat3 Y705 phosphorylation. As shown in **Figure 57**, MitoTEMPO appeared to be able to induce a partial recovery of Stat3 Y705 phosphorylation and this effect seemed to occur in a concentration-dependent manner. The results indicate an

important role for mitoROS in the regulation of Stat3 Y705 phosphorylation in LPS-activated *Sdha*^{-/-} and *Sdhb*^{-/-} macrophages.

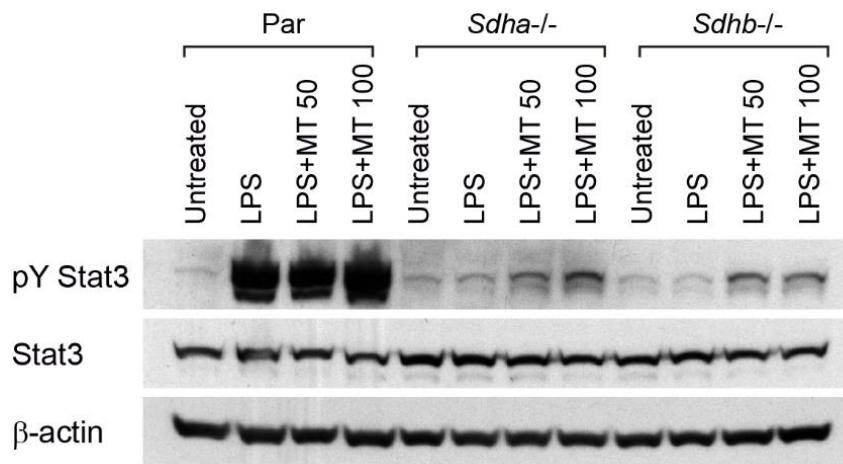


Figure 57: MitoROS scavenging's effect on Stat3 tyrosine phosphorylation in *Sdha*^{-/-} and *Sdhb*^{-/-} cells. Western blotting for Stat3 pY705, Stat3, and β -actin of parental (Par), *Sdha*^{-/-} and *Sdhb*^{-/-} RAW 24.7 cells that were left untreated or preincubated with MitoTEMPO (MT) (50 μ M or 100 μ M) for 3 hours before stimulation with LPS (100 ng/ml) for 6 hours. Representative results of three independent experiments.



Discussion



Discussion

Generation of cellular models and their importance

Metabolism and immune response are closely interrelated, with mitochondria, specifically the ETC complexes, playing a pivotal role in orchestrating this relationship^{127,128}. Earlier studies, with a predominant focus on CI, employed varied methodologies and systems, often leading to inconsistent results^{99,100,104,129}. The present research aimed to bridge the gap by developing KO cell lines corresponding to each mitochondrial complex. This homogenizes the study model, aiding in a clearer understanding of the role of individual complexes in regulating macrophage responses. The potential implications of such an understanding are vast, particularly in the context of immunological or metabolic disorders that currently present challenges in therapeutic management.

Utilizing the RAW 264.7 murine macrophage cell line, well-known for its use in innate immune response studies^{122,130,131}, this work has succeeded in generating cell lines deficient in vital constituents of mitochondrial complexes I and II, namely *Ndufs4*, *Sdha*, and *Sdhb* genes.

Advances in gene editing: The CRISPR/Cas9 HITI approach

Targeted gene editing has revolutionized the ability to study gene function. Techniques that allow targeted gene disruption and the assessment of the resulting cellular effects are of enormous relevance. The CRISPR/Cas9 has emerged as a powerful genome editing tool. It uses small RNA fragments to guide DNA cleavage at precise sites, offering speed and cost-effectiveness. Using the classic CRISPR/Cas system only, KO of a specific gene is relatively easy to achieve when mutations are generated in coding sequence through the NHEJ repair pathway. However, the disadvantage of this system is that not all cells lose expression of the target gene. It is therefore not easy to select the cells that have undergone the mutation, making it difficult to isolate KO clones from non-edited cells. The present

research used the CRISPR/Cas9 HITI, an innovative adaptation of the classic technique pioneered by Suzuki¹¹⁵. This method uses the CRISPR/Cas9 system to cut both the target gene and a donor vector. The subsequent blunt-end breaks can be repaired via the NHEJ pathway, culminating in the incorporation of a donor insert and disruption of the target gene. Incorporation of an antibiotic resistance cassette into this donor insert facilitates post-editing cellular selection, increasing efficiency compared to the conventional CRISPR/Cas9 approach. In summary, the use of HITI and carefully designed plasmids provides a robust and efficient system for targeted gene disruption.

In this work, an abbreviated post-transfection procedure was implemented. Instead of a stepwise approach with successive cell culture and isolation steps, a direct limiting dilution was performed after transfection due to the increased efficiency of the method. This more efficient process provided monoclonal cells ready for analysis. The increased efficiency of the method also eliminated the need to repeat the process with heterozygous cells, as homozygous mutant clones were obtained in a single experiment. Several PCR assays were performed to confirm the specific insertions, and Western blot and sequencing techniques further confirmed the gene disruption.

Mitochondrial dysfunction in *Ndufs4*^{-/-} macrophages

The evidence of the role of *Ndufs4* in macrophage functions and CI assembly presented in this work not only consolidates previous findings, but also provides new insights into mitochondrial biochemistry and immune metabolism. *NDUFS4* has been shown to play a key role in the final steps in CI assembly¹³²⁻¹³⁴. In the absence of *NDUFS4*, as has been observed in patient fibroblasts, there is a marked lack of fully assembled CI, leading to the appearance of partially assembled CI^{101,102,135,136}. This deficit is also accompanied by a marked reduction in the assembly of the SCs CI+CIII₂+CIV and CI+CIII₂, as well as an accumulation of lower molecular weight SCs¹³⁷. Consistent with previous studies, the present study confirmed that *Ndufs4*^{-/-} macrophages lack fully assembled free CI and CI-containing SCs (CI+CIII₂+CIV, CI+CIII₂). Interestingly, a residual CI activity of approximately 50%

was observed in *Ndufs4*^{-/-} macrophages when assessed by conventional spectrophotometric methods. This is consistent with previous studies where some CI activity was found in patient samples with mutations in *NDUFS4* despite the absence of fully assembled CI^{101,117,138–140}. Similarly, in *Ndufs4*^{-/-} mice, different tissues like the pancreas, kidney, liver, lung, brain, heart, and muscle showed a clear lack of fully assembled CI and CI-containing SCs^{102,141}. When measured with spectrophotometric assays, there was a marked decrease in CI activity in these tissues, although the extent of the decrease varied among tissues. For example, residual activity was only 9 % in the lungs and up to 44 % in the heart¹⁴¹. The residual CI activity in the *Ndufs4*^{-/-} macrophages suggests a possible compensatory mechanism, which should be investigated in more detail. However, using in-gel activity assay (IGA) measurements, no CI activity was detected in extracts derived from *Ndufs4*^{-/-} macrophages. This difference between the CI activity determined by the IGA assay and the spectrophotometric assay has been documented in previous studies^{102,137,141}. Spectrophotometric assays assess rotenone-sensitive NADH oxidation, but the rotenone-insensitive NADH oxidation prevalent in most cell types may compromise the sensitivity of the assay¹³⁸.

As expected, OCR, a measure of cellular respiration, was altered in *Ndufs4*^{-/-} macrophages. Interestingly, the proliferation of *Ndufs4*^{-/-} cells was not significantly affected when these cells were cultured in standard media supplemented with glucose. However, when the glucose was replaced by galactose, a significant impairment of cell proliferation was observed. This is remarkable because galactose forces cells to switch their energy production from substrate-level phosphorylation (a faster, less efficient way to make ATP that occurs outside the mitochondria) to mitochondrial oxidative phosphorylation, a more efficient and oxygen-dependent process that occurs inside the mitochondria using the ETC¹⁴². The impaired proliferation in galactose media correlates well with the ETC dysfunction observed in *Ndufs4*^{-/-} cells. This suggests that these cells have difficulty adapting to a more demanding energy production process due to their mitochondrial dysfunction.

In addition, an increase in the level of mitoROS was observed in the *Ndufs4*^{-/-} macrophages. This finding was initially surprising, as CI is known to be the main site of mitoROS production, and yet in the KO cells, both the assembly and the functionality of CI were severely reduced¹⁴³. However, it is consistent with previous findings that oxidative stress is a consequence of CI dysfunction^{144,145}, suggesting that other mitochondrial sites or mechanisms may contribute to the elevated mitoROS levels during ETC dysfunction. This observation is in line with previous works using other *Ndufs4*^{-/-} cell models, where elevated levels of mitoROS were also reported^{100,146}. Notably, despite the aforementioned abnormalities, the MMP was maintained in *Ndufs4*^{-/-} macrophages. This is probably due to the compensatory actions of the CIII and CIV proton pumps, which help to maintain MMP even when CI activity is impaired.

***Ndufs4* controls macrophage effector functions**

In this work it was observed that *Ndufs4*^{-/-} macrophage RAW 264.7 cells produced more of the pro-inflammatory cytokine IL-6 and less of the anti-inflammatory cytokine IL-10 than controls when challenged with LPS. This observation is consistent with previous research where palmitic acid, which like LPS acts through the TLR4 receptor, led to higher levels of inflammatory gene expression in bone marrow-derived macrophages from *Ndufs4*^{-/-} mice compared to those from wild-type mice¹⁰⁰. However, different results were obtained when using CI inhibitors, specifically metformin and rotenone. These CI inhibitors were found to decrease levels of the pro-inflammatory cytokine pro-IL-1 β and increase levels of the anti-inflammatory cytokine IL-10 in LPS-activated macrophages⁹⁹. Metformin was also shown to reduce LPS-induced lung inflammation in mice by decreasing the production of IL-1 β and IL-6⁹⁸. The differences in results between genetic and chemical models of CI inhibition suggest that the extent and nature of CI perturbation has a significant impact on macrophage behavior. Differences in the extent to which CI activity is inhibited may explain the conflicting results between studies using different models. These findings highlight the critical role of CI in balancing inflammatory and anti-inflammatory responses. Investigating the effects of genetic

deletion of different CI subunits on CI activity, and how this affects macrophage respiration, may provide important insights to explain its functions.

In addition, the *Ndufs4*^{-/-} macrophage RAW 264.7 cells displayed enhanced phagocytic capacity. This is consistent with previous findings indicating that rotenone, a CI inhibitor, enhances non-opsonic phagocytosis of bacteria¹⁴⁷. The enhanced phagocytic capacity, together with the altered cytokine production profiles in *Ndufs4*^{-/-} macrophages, highlights the interrelated nature of mitochondrial function, in particular CI activity, with macrophage responses.

SDH/CII deficiency and macrophage bioenergetics

With regard to SDH/CII, this study identifies previously unknown roles for SDH/CII in macrophage metabolic phenotype and effector functions using *Sdha* and *Sdhb* deficient macrophages.

The results of this study demonstrated that the absence of *Sdha* and *Sdhb* dramatically impairs the basal respiratory process in macrophages. Comparable results have been obtained from studies using different SDH knockout cell models, including *Sdhb*^{-/-} murine kidney cells¹⁴⁸, *SDHB*^{-/-} human kidney cells¹⁴⁹, *SDHB*^{-/-} human breast cancer cells¹⁵⁰ and *SDHA*^{-/-} human leukemia cells¹⁵¹. Both *Sdha*^{-/-} macrophages, lacking detectable levels of *Sdhb*, and *Sdhb*^{-/-} macrophages, with unaltered *Sdha* expression, showed analogous bioenergetic patterns. This suggests a non-significant role for uncoupled *Sdha* in mitochondrial bioenergetics.

More remarkably, no significant phenotypic differences were observed between *Sdha*^{-/-} and *Sdhb*^{-/-} macrophages in terms of HIF-1 α protein levels and growth rates. Notably, *Sdha*^{-/-} macrophages exhibited a behavior similar to that of *Sdhb*^{-/-} macrophages, leading to significantly reduced HIF-1 α expression levels, in contrast to findings in cancer cell lines of various origins where free *Sdha* induces an increase in HIF-1 α expression in the absence of *Sdhb* and promotes cell growth¹⁵². This suggests that the proposed mechanism for HIF-1 α stabilization by free SDHA in tumors with mutations in the SDHB, SDHC and SDHD subunits may not be accurate.

SDH/CII and key signalling pathways

With regard to HIF-1 α , previous studies have shown that high concentrations of succinate help stabilize HIF-1 α and then induce the production of IL-1 β in LPS-activated macrophages^{106,107}. However, the metabolism of succinate by SDH is a critical aspect of its pro-inflammatory effect, as demonstrated by the use of the *Sdha* inhibitor DMM¹⁰⁷. The results of this thesis confirm that high levels of succinate alone are not sufficient to increase HIF-1 α levels and trigger IL-1 β production but require its oxidation by SDH. This implicates both *Sdha* and *Sdhb* upstream of the master regulator HIF-1 α .

Focusing on the second master regulator downstream of SDH, AMPK, previous reports have highlighted its role in enhancing macrophage phagocytic capacity¹⁵³. The present study demonstrates that the hyperactivation of AMPK is a fundamental factor underlying the enhanced phagocytic capacity observed in *Sdha*^{-/-} and *Sdhb*^{-/-} macrophages. The anti-inflammatory properties of AMPK have been well documented in a range of cell types, including macrophages and epithelial cells¹⁵⁴. In macrophages, AMPK is critical for IL-10 production and acquisition of the M2 phenotype¹⁵⁴. However, despite AMPK hyperactivation, *Sdha*^{-/-} and *Sdhb*^{-/-} macrophages showed an inability to secrete IL-10. This suggests that the SDH/CII target molecule that restricts IL-10 production is downstream of the AMPK pathway, highlighting the complex interplay between metabolic regulators in determining macrophage functionality and immune responses.

The observed inability to produce IL-10 stands out as the most pronounced cytokine phenotype in *Sdha*^{-/-} and *Sdhb*^{-/-} macrophages. Interestingly, although treatment with DMM resulted in a reduction in LPS-induced IL-10 production, the extent of this reduction was much less pronounced. This discrepancy may be due to the lesser degree of respiratory impairment in cells in which SDH/CII is only inhibited by DMM, in contrast to the more severe respiratory impairment observed in knockout cells. Alternatively, the difference may reflect metabolic adaptations resulting from the long-term absence of SDH in knockout cells, culminating in reduced IL-10 production. This notion is further supported by the observation that prolonged DMM

treatment of 7 days resulted in a greater decrease in IL-10 production compared to only 1 hour of pre-treatment.

The IL-10 findings appear to contradict previous studies using chemical inhibitors of SDHA, which have documented either an increase^{104,107} or a slight decrease¹¹⁹ in IL-10 expression. It is important to acknowledge that the use of chemical inhibitors versus genetic models has historically yielded different, sometimes contradictory, results in different cellular pathways. For example, as mentioned above, while chemical inhibition of CI prevents the production of the pro-inflammatory cytokine IL-1 β ⁹⁹, genetic deletion of the CI subunit *Ndufs4* is associated with a pro-inflammatory macrophage phenotype. These contrasting observations underscore the importance of using a combination of genetic and chemical methods when attempting to dissect protein function.

This study further explores the molecular mechanisms responsible for the observed deficiency in IL-10 production in *Sdha*^{-/-} and *Sdhb*^{-/-} macrophages. The results show that the SDH/CII complex is crucial in enabling LPS-induced phosphorylation of Stat3 at Y705, which in turn facilitates its binding to target sequences on the IL-10 promoter, thereby promoting transcription¹⁵⁵. It is also shown that the SDH/CII complex plays a necessary role in IL-10-induced Stat3 Y705 phosphorylation. The importance of autocrine IL-10 in attenuating LPS-induced inflammatory responses in macrophages has been established primarily through its ability to switch the metabolic phenotype from aerobic glycolysis to OXPHOS^{29,31,156}. At the molecular level, IL-10 promotes OXPHOS by accelerating the degradation of ROS-generating mitochondria via Stat3 activation, as well as increasing the activity of SDH/CII by upregulating *Arg2*¹⁵⁶. In addition, IL-10 inhibits iNOS, thereby reducing NO-mediated OXPHOS suppression²⁹. As expected, the low presence of IL-10 in the culture supernatants of LPS-challenged *Sdha*^{-/-} and *Sdhb*^{-/-} macrophages correlated with increased iNOS expression. This is consistent with a previous study documenting IL-10-mediated Stat3 activation as a suppressor of NO synthesis¹⁵⁷. However, the addition of IL-10 barely restored the elevated iNOS levels in *Sdha*^{-/-} and *Sdhb*^{-/-} macrophages.

Focusing on the serine phosphorylated variant of Stat3 (pS727), a slight but significant increase in its levels was observed in LPS-activated *Sdha*^{-/-} and *Sdhb*^{-/-} macrophages. The biological role and mechanism of action of Stat3 pS727 remains controversial. Some researchers suggest that Stat3 pS727 is essential for enhancing the transcriptional activity of Stat3, while others argue that it acts to downregulate its activity^{158–161}. Interestingly, previous reports have suggested that Stat3 pS727 can enter the mitochondria, interact with complexes I and II, and enhance the activities of both complexes in pro-B cells¹⁶². This work provides new evidence that Stat3 serine phosphorylation is independent of tyrosine phosphorylation and CII integrity. However, the small increase in Stat3 pS727 levels in LPS-activated *Sdha*^{-/-} and *Sdhb*^{-/-} macrophages may indicate the mitigation of potential negative feedback exerted by both CII activity and Y705 phosphorylation on S727 phosphorylation.

In addition, this work provides further evidence for a link between oxidative stress and Stat3 activity and supports the notion that anti-inflammatory macrophages require intact mitochondria for their function¹⁶³. Reduction of mitoROS was observed to partially restore Stat3 Y705 phosphorylation in LPS-activated *Sdha*^{-/-} and *Sdhb*^{-/-} macrophages. This partial recovery was expected given that it is not likely that mitoTEMPO treatment would adequately and completely reverse the broad spectrum of molecular alterations (e.g. epigenetic modifications, post-translational adjustments) that result from chronic oxidative stress.

Moreover, the results demonstrate that the reduced levels of itaconate and fumarate in *Sdha*^{-/-} and *Sdhb*^{-/-} macrophages do not contribute to the pY705 phenotype. The study also shows that the cell-permeable derivatives OI and DMF, when used at standard concentrations^{164,165}, significantly reduce Stat3 Y705 tyrosine phosphorylation in LPS-treated parental cells. Previous studies on itaconate and fumarate have focused on their anti-inflammatory properties, with particular emphasis on their ability to inhibit IL-1 β secretion^{164–166}. Notably, itaconate has been shown to inhibit the HIF-1 α /IL-1 β pathway, in part through its inhibitory effect on SDH activity¹⁶⁷.

In summary, these findings elucidate a pivotal role of macrophage functionality for SDH/CII that extends beyond its known function within the ETC. This role is mediated through the sophisticated modulation of metabolic pathways, signaling molecules, and transcription factors. Mechanistic insights include the alteration of macrophage bioenergetics, which has broad implications for multiple signaling cascades. In particular, this alteration directly affects the stabilization of HIF-1 α and the subsequent secretion of IL-1 β . Furthermore, hyperactivation of AMPK is shown to significantly enhance phagocytic capabilities, illustrating a complex regulatory mechanism that balances energy sensing with innate immune function. The proposed model also implies the role of the oxidative stress response as a modulator of Stat3 phosphorylation, which affects the production of IL-10. Taken together, these findings provide a refined understanding of the metabolic regulatory pathways that underlie macrophage effector functions.

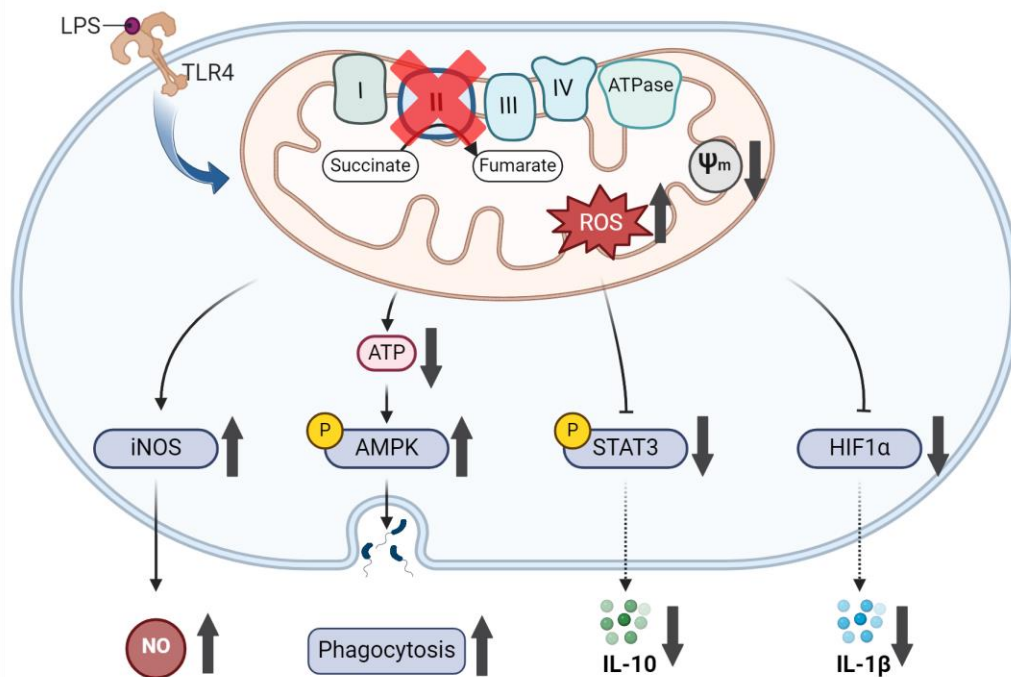


Figure 58: The graphic summary depicts a mechanistic model in which activation of macrophages by LPS through the TLR4 receptor leads to several downstream effects that are altered in the absence of CII.

Limitations of this study and future perspectives

This study provides valuable insights into the role of ETC, particularly CI and CII, in macrophage function. However, it is important to highlight limitations that warrant further discussion.

While the RAW 264.7 cell line and BMDM serve as validated tools to explore the phenotypes of mature macrophages *in vitro*, further investigations using animal models, such as macrophage-specific KO mice targeting ETC subunits, are essential to validate our findings and to understand the implications of ETC dysfunction in disease contexts.

Moreover, it is critical to recognize the ongoing challenge of CRISPR/Cas9 off-target effects¹⁶⁸. To mitigate these effects, several independent KO cell clones have been generated and tested. However, it is important to note that the control cells in the experiments were parental RAW 264.7 cells and did not undergo the same treatments as the KO cells, potentially compromising their suitability as ideal controls from a rigorous point of view. Different control cells carrying non-targeting sgRNA and a blasticidin cassette will be generated and used in future experiments.

In addition, prolonged culture of ETC KO cells may induce metabolic and epigenetic adaptations. The development of new cells that allow for conditional ablation of *Ndufs4*, *Sdha*, and *Sdhb* could help reveal the direct effects of protein depletion and avoid masking by long-term adaptations.

Finally, another limitation is that it was possible to analyze the function of free *Sdha* but not the impact of isolated *Sdha* deficiency. This is because *Sdhb* KO cells express free *Sdha*, whereas *Sdha* KO cells simultaneously lose *Sdhb*. Therefore, the possibility that the *Sdha* KO phenotype is largely due to the absence of *Sdhb* cannot be excluded. Future research should seek to distinguish between the specific functions and contributions of each gene to the observed phenotypes. In addition, further exploration of the relationship between the stability of *Sdha* and *Sdhb* and their relationship with other ETC subunits is critical to understanding the intricate dynamics within the mitochondrial respiratory chain and its impact on cellular processes.

Towards potential therapeutic applications

This study has deepened the understanding of how mitochondrial functions and macrophage responses interact, but it also invites further investigation into the molecular details of these relationships. One interesting possibility is to use this knowledge for new treatments. For example, manipulating the activity of mitochondrial complexes could be a viable approach to modulate macrophage responses in diseases where inflammation plays a critical role, such as autoimmune diseases or chronic inflammatory conditions. However, there are challenges to overcome. The complex ways in which mitochondria interact within cells need to be better understood. Also, a combination of genetic and chemical methods is needed to get a clearer picture of how cells and molecules work together in immune and metabolic responses.

Targeting the ETC for therapy is promising, but a careful balance needs to be found between the benefits and the risks of disrupting important cell functions. The anti-diabetic drug metformin, which is known to inhibit CI, is a good example of this approach. In addition to its ability to regulate glucose levels, it also reduces inflammation, which is particularly beneficial in type 2 diabetes mellitus, where IL-1 β damages pancreatic cells¹⁶⁹. The anti-inflammatory effects of metformin are also seen in conditions such as lupus, colitis, arthritis, psoriasis and obesity. Exactly how it works, whether through complex I inhibition or other means, is still under investigation. Another potential target is SDH/CII. The inhibitor DMM has shown promise in reducing inflammation in macrophages and protecting against oxidative damage in models of heart and liver injury^{170,171}. However, more research is needed to confirm its safety and efficacy in humans and to explore similar compounds for the treatment of inflammatory diseases.

In conclusion, the results of this study should pave the way for the development of new therapeutic strategies targeting the mitochondrial ETC as well as their testing in newly generated macrophage KO models.





Conclusions



Conclusions

1. KO macrophage cell models were successfully generated for key subunits of ETC complexes I and II.
2. Ndufs4 is critical for CI assembly in macrophages.
3. The Ndufs4^{-/-} macrophages exhibit altered cytokine production, with an increase in the proinflammatory cytokine IL-6 and a decrease in the anti-inflammatory cytokine IL-10. They also exhibit increased phagocytic capacity.
4. The absence of Sdha and Sdhb in macrophages dramatically impairs their respiratory capacity. Therefore, these cells rely primarily on glycolysis for ATP production. This metabolic shift is accompanied by increased levels of mitoROS, NO and dysfunctional mitochondria.
5. The absence of Sdha and Sdhb in macrophages leads to a decrease in HIF-1 α expression and IL-1 β production in response to LPS. In addition, the phagocytic capacity of KO cells is increased, but the bactericidal activity is comparable to that of parental macrophages.
6. Sdha and Sdhb are essential for LPS-induced production of IL-10 in macrophages, a potent negative feedback regulator of macrophage inflammatory response.
7. The absence of Sdha and Sdhb in macrophages leads to increased AMPK phosphorylation in response to energy stress. Notably, the persistence of high phagocytic activity in these cells after AMPK inhibition suggests that other factors contribute to the enhanced phagocytic phenotype.
8. The absence of Sdha and Sdhb inhibits LPS-induced Stat3 Y705 phosphorylation, which is important for IL-10 transcription. This inhibition is partly due to the excessive accumulation of mitoROS in these KO cells.
9. The absence of Sdha and Sdhb inhibits IL-10-mediated Stat3 Y705 phosphorylation, which is a critical molecular mechanism for the role of IL-10 as an inhibitor of the macrophage inflammatory response.



References

1. Spits, H. & Di Santo, J. P. The expanding family of innate lymphoid cells: regulators and effectors of immunity and tissue remodeling. *Nat Immunol* **12**, 21–27 (2011).
2. Newman, S. L., Mikus, L. K. & Tucci, M. A. Differential requirements for cellular cytoskeleton in human macrophage complement receptor- and Fc receptor-mediated phagocytosis. *Journal of immunology* **146**, 967–974 (1991).
3. Lukacs, G. L., Rotstein, O. D. & Grinstein, S. Phagosomal acidification is mediated by a vacuolar-type H(+)-ATPase in murine macrophages. *J Biol Chem* **265** **34**, 21099–21107 (1990).
4. Flannagan, R. S., Jaumouillé, V. & Grinstein, S. The cell biology of phagocytosis. *Annu Rev Pathol* **7**, 61–98 (2012).
5. Rosales, C. & Uribe-Querol, E. Phagocytosis: A Fundamental Process in Immunity. *Biomed Res Int* **2017**, (2017).
6. Aderem, A. & Underhill, D. M. Mechanisms of phagocytosis in macrophages. <https://doi.org/10.1146/annurev.immunol.17.1.593> **17**, 593–623 (2003).
7. Underhill, D. M. & Ozinsky, A. Phagocytosis of Microbes: Complexity in Action. <https://doi.org/10.1146/annurev.immunol.20.103001.114744> **20**, 825–852 (2003).
8. Greenberg, S. & Grinstein, S. Phagocytosis and innate immunity. *Curr Opin Immunol* **14**, 136–145 (2002).
9. Murray, P. J. *et al.* Macrophage activation and polarization: nomenclature and experimental guidelines. *Immunity* **41**, 14–20 (2014).
10. El Kasmi, K. C. *et al.* Toll-like receptor-induced arginase 1 in macrophages thwarts effective immunity against intracellular pathogens. *Nat Immunol* **9**, 1399–1406 (2008).

11. Buxadé, M. *et al.* Gene expression induced by Toll-like receptors in macrophages requires the transcription factor NFAT5. *Journal of Experimental Medicine* **209**, 379–393 (2012).
12. Brubaker, S. W., Bonham, K. S., Zanoni, I. & Kagan, J. C. Innate immune pattern recognition: a cell biological perspective. *Annu Rev Immunol* **33**, 257–290 (2015).
13. Akira, S., Uematsu, S. & Takeuchi, O. Pathogen recognition and innate immunity. *Cell* **124**, 783–801 (2006).
14. Takeuchi, O. & Akira, S. Pattern recognition receptors and inflammation. *Cell* **140**, 805–820 (2010).
15. Krausgruber, T. *et al.* IRF5 promotes inflammatory macrophage polarization and TH1-TH17 responses. *Nat Immunol* **12**, 231–238 (2011).
16. Kim, T. W. *et al.* Anti-Inflammatory Mechanisms of Koreanaside A, a Lignan Isolated from the Flower of *Forsythia koreana*, against LPS-Induced Macrophage Activation and DSS-Induced Colitis Mice: The Crucial Role of AP-1, NF- κ B, and JAK/STAT Signaling. *Cells* 2019, Vol. 8, Page 1163 **8**, 1163 (2019).
17. Yu, Q. *et al.* Resokaempferol-mediated anti-inflammatory effects on activated macrophages via the inhibition of JAK2/STAT3, NF- κ B and JNK/p38 MAPK signaling pathways. *Int Immunopharmacol* **38**, 104–114 (2016).
18. Tugal, D., Liao, X. & Jain, M. K. Transcriptional Control of Macrophage Polarization. *Arterioscler Thromb Vasc Biol* **33**, 1135–1144 (2013).
19. Sica, A., Erreni, M., Allavena, P. & Porta, C. Macrophage polarization in pathology. *Cell Mol Life Sci* **72**, 4111–4126 (2015).
20. Mantovani, A. *et al.* The chemokine system in diverse forms of macrophage activation and polarization. *Trends Immunol* **25**, 677–686 (2004).

21. Curfs, J. H. A. J., Meis, J. F. G. M. & Hoogkamp-Korstanje, J. A. A. A primer on cytokines: sources, receptors, effects, and inducers. *Clin Microbiol Rev* **10**, 742–780 (1997).
22. Kany, S., Vollrath, J. T. & Relja, B. Cytokines in Inflammatory Disease. *Int J Mol Sci* **20**, (2019).
23. Dinarello, C. A. Immunological and inflammatory functions of the interleukin-1 family. *Annu Rev Immunol* **27**, 519–550 (2009).
24. Parameswaran, N. & Patial, S. Tumor Necrosis Factor- α Signaling in Macrophages. *Crit Rev Eukaryot Gene Expr* **20**, 87 (2010).
25. Scheller, J., Chalaris, A., Schmidt-Arras, D. & Rose-John, S. The pro- and anti-inflammatory properties of the cytokine interleukin-6. *Biochimica et Biophysica Acta (BBA) - Molecular Cell Research* **1813**, 878–888 (2011).
26. Fernando, M. R., Reyes, J. L., Iannuzzi, J., Leung, G. & McKay, D. M. The Pro-Inflammatory Cytokine, Interleukin-6, Enhances the Polarization of Alternatively Activated Macrophages. *PLoS One* **9**, e94188 (2014).
27. Ananieva, O. *et al.* The kinases MSK1 and MSK2 act as negative regulators of Toll-like receptor signaling. *Nat Immunol* **9**, 1028–1036 (2008).
28. Danne, C. *et al.* A Large Polysaccharide Produced by *Helicobacter hepaticus* Induces an Anti-inflammatory Gene Signature in Macrophages. *Cell Host Microbe* **22**, 733-745.e5 (2017).
29. Baseler, W. A. *et al.* Autocrine IL-10 functions as a rheostat for M1 macrophage glycolytic commitment by tuning nitric oxide production. *Redox Biol* **10**, 12 (2016).
30. Sanin, D. E., Prendergast, C. T. & Mountford, A. P. IL-10 Production in Macrophages Is Regulated by a TLR-Driven CREB-Mediated Mechanism That Is Linked to Genes Involved in Cell Metabolism. *The Journal of Immunology* **195**, 1218–1232 (2015).

31. Ip, W. K. E., Hoshi, N., Shouval, D. S., Snapper, S. & Medzhitov, R. Anti-inflammatory effect of IL-10 mediated by metabolic reprogramming of macrophages. *Science (1979)* **356**, 513–519 (2017).
32. Munder, M., Eichmann, K. & Modolell, M. Alternative Metabolic States in Murine Macrophages Reflected by the Nitric Oxide Synthase/Arginase Balance: Competitive Regulation by CD4+ T Cells Correlates with Th1/Th2 Phenotype. *The Journal of Immunology* **160**, 5347–5354 (1998).
33. Haschemi, A. *et al.* The sedoheptulose kinase CARKL directs macrophage polarization through control of glucose metabolism. *Cell Metab* **15**, 813–826 (2012).
34. Warburg, O., Wind, F. & Negelein, E. The metabolism of tumors in the body. *J Gen Physiol* **8**, 519 (1927).
35. Galván-Peña, S. & O'Neill, L. A. J. Metabolic reprogramming in macrophage polarization. *Front Immunol* **5**, (2014).
36. Shapouri-Moghaddam, A. *et al.* Macrophage plasticity, polarization, and function in health and disease. *J Cell Physiol* **233**, 6425–6440 (2018).
37. Williams, N. C. & O'Neill, L. A. J. A Role for the Krebs Cycle Intermediate Citrate in Metabolic Reprogramming in Innate Immunity and Inflammation. *Front Immunol* **9**, 1 (2018).
38. Huang, S. C. C. *et al.* Cell-intrinsic lysosomal lipolysis is essential for alternative activation of macrophages. *Nature Immunology 2014 15:9* **15**, 846–855 (2014).
39. Tavakoli, S., Zamora, D., Ullevig, S. & Asmis, R. Bioenergetic Profiles Diverge During Macrophage Polarization: Implications for the Interpretation of 18F-FDG PET Imaging of Atherosclerosis. *J Nucl Med* **54**, 1661 (2013).
40. Vats, D. *et al.* Oxidative metabolism and PGC-1beta attenuate macrophage-mediated inflammation. *Cell Metab* **4**, 13–24 (2006).

41. Rodríguez-Prados, J.-C. *et al.* Substrate fate in activated macrophages: a comparison between innate, classic, and alternative activation. *J Immunol* **185**, 605–614 (2010).
42. Tan, Z. *et al.* Pyruvate dehydrogenate kinase 1 participates in macrophage polarization via regulating glucose metabolism. *J Immunol* **194**, 6082 (2015).
43. Huang, S. C. C. *et al.* mTORC2-IRF4 mediated metabolic reprogramming is essential for macrophage alternative activation. *Immunity* **45**, 817 (2016).
44. Wang, F. *et al.* Glycolytic Stimulation is not a Requirement for M2 Macrophage Differentiation. *Cell Metab* **28**, 463 (2018).
45. Wculek, S. K. *et al.* Oxidative phosphorylation selectively orchestrates tissue macrophage homeostasis. *Immunity* **56**, 516-530.e9 (2023).
46. Bailey, J. D. *et al.* Nitric Oxide Modulates Metabolic Remodeling in Inflammatory Macrophages through TCA Cycle Regulation and Itaconate Accumulation. *Cell Rep* **28**, 218 (2019).
47. Lackey, D. E. & Olefsky, J. M. Regulation of metabolism by the innate immune system. *Nat Rev Endocrinol* **12**, 15–20 (2016).
48. Covarrubias, A. J., Aksoylar, H. I. & Horng, T. Control of macrophage metabolism and activation by mTOR and Akt signaling. *Semin Immunol* **27**, 286–296 (2015).
49. Biswas, S. K. & Mantovani, A. Orchestration of metabolism by macrophages. *Cell Metab* **15**, 432–437 (2012).
50. Stehling, O., Wilbrecht, C. & Lill, R. Mitochondrial iron-sulfur protein biogenesis and human disease. *Biochimie* **100**, 61–77 (2014).
51. Chandel, N. S. Mitochondria as signaling organelles. *BMC Biol* **12**, 34 (2014).

52. Rizzuto, R., De Stefani, D., Raffaello, A. & Mammucari, C. Mitochondria as sensors and regulators of calcium signalling. *Nat Rev Mol Cell Biol* **13**, 566–578 (2012).
53. Harbauer, A. B., Zahedi, R. P., Sickmann, A., Pfanner, N. & Meisinger, C. The protein import machinery of mitochondria—a regulatory hub in metabolism, stress, and disease. *Cell Metab* **19**, 357–372 (2014).
54. Tait, S. W. G. & Green, D. R. Mitochondria and cell death: outer membrane permeabilization and beyond. *Nat Rev Mol Cell Biol* **11**, 621–632 (2010).
55. Ellenrieder, L. *et al.* Dual Role of Mitochondrial Porin in Metabolite Transport across the Outer Membrane and Protein Transfer to the Inner Membrane. *Mol Cell* **73**, 1056-1065.e7 (2019).
56. Lemasters, J. J. Modulation of mitochondrial membrane permeability in pathogenesis, autophagy and control of metabolism. *J Gastroenterol Hepatol* **22 Suppl 1**, (2007).
57. Cooper, G. M. Bioenergetics and Metabolism - Mitochondria, Chloroplasts, and Peroxisomes. (2000).
58. Schultz, B. E. & Chan, S. I. Structures and Proton-Pumping Strategies of Mitochondrial Respiratory Enzymes. <https://doi.org/10.1146/annurev.biophys.30.1.23> **30**, 23–65 (2003).
59. Capaldi, R. A. & Aggeler, R. Mechanism of the F(1)F(0)-type ATP synthase, a biological rotary motor. *Trends Biochem Sci* **27**, 154–160 (2002).
60. Dimroth, P., von Ballmoos, C. & Meier, T. Catalytic and mechanical cycles in F-ATP synthases. Fourth in the Cycles Review Series. *EMBO Rep* **7**, 276–282 (2006).
61. Abrahams, J. P., Leslie, A. G. W., Lutter, R. & Walker, J. E. Structure at 2.8 Å resolution of F1-ATPase from bovine heart mitochondria. *Nature* **370**, 621–628 (1994).

62. Rizwan, M., Rasheed, H. Al & Tarjan, G. Succinate Dehydrogenase Complex: An Updated Review. *Arch Pathol Lab Med* **142**, 1564–1570 (2018).
63. Wiedemann, N., Frazier, A. E. & Pfanner, N. The protein import machinery of mitochondria. *J Biol Chem* **279**, 14473–14476 (2004).
64. Christian, B. E. & Spremulli, L. L. Mechanism of protein biosynthesis in mammalian mitochondria. *Biochim Biophys Acta* **1819**, 1035–1054 (2012).
65. Hofhaus, G., Weiss, H. & Leonard, K. Electron microscopic analysis of the peripheral and membrane parts of mitochondrial NADH dehydrogenase (Complex I). *J Mol Biol* **221**, 1027–1043 (1991).
66. Vinothkumar, K. R., Zhu, J. & Hirst, J. Architecture of mammalian respiratory complex I. *Nature* **515**, 80–84 (2014).
67. Zickermann, V. *et al.* Structural biology. Mechanistic insight from the crystal structure of mitochondrial complex I. *Science* **347**, 44–49 (2015).
68. Walker, J. E. The NADH:ubiquinone oxidoreductase (complex I) of respiratory chains. *Q Rev Biophys* **25**, 253–324 (1992).
69. Friedrich, T. *et al.* Two binding sites of inhibitors in NADH: ubiquinone oxidoreductase (complex I). Relationship of one site with the ubiquinone-binding site of bacterial glucose:ubiquinone oxidoreductase. *Eur J Biochem* **219**, 691–698 (1994).
70. Sazanov, L. A. Respiratory complex I: mechanistic and structural insights provided by the crystal structure of the hydrophilic domain. *Biochemistry* **46**, 2275–2288 (2007).
71. Sazanov, L. A. From the ‘black box’ to ‘domino effect’ mechanism: what have we learned from the structures of respiratory complex I. *Biochem J* **480**, 319–333 (2023).

72. Murphy, M. P. How mitochondria produce reactive oxygen species. *Biochem J* **417**, 1–13 (2009).
73. Wallace, D. C. A mitochondrial paradigm of metabolic and degenerative diseases, aging, and cancer: a dawn for evolutionary medicine. *Annu Rev Genet* **39**, 359–407 (2005).
74. Finkel, T. & Holbrook, N. J. Oxidants, oxidative stress and the biology of ageing. *Nature* **408**, 239–247 (2000).
75. Balaban, R. S., Nemoto, S. & Finkel, T. Mitochondria, oxidants, and aging. *Cell* **120**, 483–495 (2005).
76. Du, Z. *et al.* Structure of the human respiratory complex II. *Proc Natl Acad Sci U S A* **120**, e2216713120 (2023).
77. Xia, D. *et al.* Crystal structure of the cytochrome bc₁ complex from bovine heart mitochondria. *Science* **277**, 60–66 (1997).
78. Iwata, S. *et al.* Complete structure of the 11-subunit bovine mitochondrial cytochrome bc₁ complex. *Science* **281**, 64–71 (1998).
79. Crofts, A. R. *et al.* The Q-cycle reviewed: How well does a monomeric mechanism of the bc₁(1) complex account for the function of a dimeric complex? *Biochim Biophys Acta* **1777**, 1001–1019 (2008).
80. Xia, D. *et al.* Structural analysis of cytochrome bc₁ complexes: implications to the mechanism of function. *Biochim Biophys Acta* **1827**, 1278–1294 (2013).
81. Turrens, J. F. Mitochondrial formation of reactive oxygen species. *J Physiol* **552**, 335–344 (2003).
82. Muller, F. L., Liu, Y. & Van Remmen, H. Complex III Releases Superoxide to Both Sides of the Inner Mitochondrial Membrane. *Journal of Biological Chemistry* **279**, 49064–49073 (2004).

83. Yoshikawa, S. *et al.* Redox-coupled crystal structural changes in bovine heart cytochrome c oxidase. *Science* **280**, 1723–1729 (1998).
84. Tsukihara, T. *et al.* The whole structure of the 13-subunit oxidized cytochrome c oxidase at 2.8 Å. *Science* **272**, 1136–1144 (1996).
85. Kadenbach, B., Hüttemann, M., Arnold, S., Lee, I. & Bender, E. Mitochondrial energy metabolism is regulated via nuclear-coded subunits of cytochrome c oxidase. *Free Radic Biol Med* **29**, 211–221 (2000).
86. Vercellino, I. & Sazanov, L. A. The assembly, regulation and function of the mitochondrial respiratory chain. *Nature Reviews Molecular Cell Biology* Preprint at <https://doi.org/10.1038/s41580-021-00415-0> (2021).
87. Althoff, T., Mills, D. J., Popot, J. L. & Kühlbrandt, W. Arrangement of electron transport chain components in bovine mitochondrial supercomplex I1III2IV1. *EMBO J* **30**, 4652–4664 (2011).
88. Davies, K. M., Blum, T. B. & Kühlbrandt, W. Conserved in situ arrangement of complex I and III2 in mitochondrial respiratory chain supercomplexes of mammals, yeast, and plants. *Proc Natl Acad Sci U S A* **115**, 3024–3029 (2018).
89. Letts, J. A., Fiedorczuk, K. & Sazanov, L. A. The architecture of respiratory supercomplexes. *Nature* **537**, 644–648 (2016).
90. Letts, J. A., Fiedorczuk, K., Degliesposti, G., Skehel, M. & Sazanov, L. A. Structures of Respiratory Supercomplex I+III2 Reveal Functional and Conformational Crosstalk. *Mol Cell* **75**, 1131-1146.e6 (2019).
91. Vercellino, I. & Sazanov, L. A. Structure and assembly of the mammalian mitochondrial supercomplex CIII2CIV. *Nature* **598**, 364–367 (2021).
92. Lopez-Fabuel, I. *et al.* Complex I assembly into supercomplexes determines differential mitochondrial ROS production in neurons and astrocytes. *Proc Natl Acad Sci U S A* **113**, 13063–13068 (2016).

93. Wu, M., Gu, J., Guo, R., Huang, Y. & Yang, M. Structure of Mammalian Respiratory Supercomplex I1III2IV1. *Cell* **167**, 1598-1609.e10 (2016).
94. den Brave, F. & Becker, T. Supercomplex formation boosts respiration. *EMBO Rep* **21**, (2020).
95. Berndtsson, J. *et al.* Respiratory supercomplexes enhance electron transport by decreasing cytochrome c diffusion distance. *EMBO Rep* **21**, (2020).
96. Acín-Pérez, R. *et al.* Respiratory complex III is required to maintain complex I in mammalian mitochondria. *Mol Cell* **13**, 805–815 (2004).
97. Jha, A. K. *et al.* Network integration of parallel metabolic and transcriptional data reveals metabolic modules that regulate macrophage polarization. *Immunity* **42**, 419–430 (2015).
98. Xian, H. *et al.* Metformin inhibition of mitochondrial ATP and DNA synthesis abrogates NLRP3 inflammasome activation and pulmonary inflammation. *Immunity* **54**, 1463-1477.e11 (2021).
99. Kelly, B., Tannahill, G. M., Murphy, M. P. & O'Neill, L. A. J. Metformin Inhibits the Production of Reactive Oxygen Species from NADH:Ubiquinone Oxidoreductase to Limit Induction of Interleukin-1 β (IL-1 β) and Boosts Interleukin-10 (IL-10) in Lipopolysaccharide (LPS)-activated Macrophages. *Journal of Biological Chemistry* **290**, 20348–20359 (2015).
100. Jin, Z., Wei, W., Yang, M., Du, Y. & Wan, Y. Mitochondrial complex I activity suppresses inflammation and enhances bone resorption by shifting macrophage-osteoclast polarization. *Cell Metab* **20**, 483–498 (2014).
101. Leshinsky-Silver, E. *et al.* NDUFS4 mutations cause Leigh syndrome with predominant brainstem involvement. *Mol Genet Metab* **97**, 185–189 (2009).
102. Adjobo-Hermans, M. J. W. *et al.* NDUFS4 deletion triggers loss of NDUFA12 in *Ndufs4*^{-/-} mice and Leigh syndrome patients: A stabilizing role for NDUFAF2. *Biochim Biophys Acta Bioenerg* **1861**, (2020).

103. Park, D. W. *et al.* Activation of AMPK Enhances Neutrophil Chemotaxis and Bacterial Killing. *Molecular Medicine* **19**, 387 (2013).
104. Garaude, J. *et al.* Mitochondrial respiratory-chain adaptations in macrophages contribute to antibacterial host defense. *Nat Immunol* **17**, 1037–1045 (2016).
105. Chouchani, E. T. *et al.* Mitochondrial ROS regulate thermogenic energy expenditure and sulfenylation of UCP1. *Nature* **532**, 112–116 (2016).
106. Tannahill, G. M. *et al.* Succinate is an inflammatory signal that induces IL-1 β through HIF-1 α . *Nature* **496**, 238–242 (2013).
107. Mills, E. L. *et al.* Succinate Dehydrogenase Supports Metabolic Repurposing of Mitochondria to Drive Inflammatory Macrophages. *Cell* **167**, 457-470.e13 (2016).
108. Lampropoulou, V. *et al.* Itaconate Links Inhibition of Succinate Dehydrogenase with Macrophage Metabolic Remodeling and Regulation of Inflammation. *Cell Metab* (2016) doi:10.1016/j.cmet.2016.06.004.
109. Cordes, T. *et al.* Immunoresponsive gene 1 and itaconate inhibit succinate dehydrogenase to modulate intracellular succinate levels. *Journal of Biological Chemistry* **291**, 14274–14284 (2016).
110. Acín-Pérez, R. *et al.* Fgr kinase is required for proinflammatory macrophage activation during diet-induced obesity. *Nature Metabolism* **2020 2:9 2**, 974–988 (2020).
111. Guzy, R. D. *et al.* Mitochondrial complex III is required for hypoxia-induced ROS production and cellular oxygen sensing. *Cell Metab* **1**, 401–408 (2005).
112. Ahmed, D. *et al.* Differential remodeling of the electron transport chain is required to support TLR3 and TLR4 signaling and cytokine production in macrophages. *Scientific Reports* **2019 9:1 9**, 1–13 (2019).

113. Angireddy, R. *et al.* Cytochrome c oxidase dysfunction enhances phagocytic function and osteoclast formation in macrophages. *FASEB J* **33**, 9167–9181 (2019).
114. Raschke, W. C., Baird, S., Ralph, P. & Nakoinz, I. Functional macrophage cell lines transformed by abelson leukemia virus. *Cell* **15**, 261–267 (1978).
115. Suzuki, K. *et al.* In vivo genome editing via CRISPR/Cas9 mediated homology-independent targeted integration. *Nature* **540**, 144–149 (2016).
116. Bujan, N. *et al.* Multicentric Standardization of Protocols for the Diagnosis of Human Mitochondrial Respiratory Chain Defects. *Antioxidants (Basel)* **11**, (2022).
117. Scacco, S. *et al.* Pathological mutations of the human NDUFS4 gene of the 18-kDa (AQDQ) subunit of complex I affect the expression of the protein and the assembly and function of the complex. *J Biol Chem* **278**, 44161–44167 (2003).
118. Kahlhöfer, F., Kmita, K., Wittig, I., Zwicker, K. & Zickermann, V. Accessory subunit NUYM (NDUFS4) is required for stability of the electron input module and activity of mitochondrial complex I. *Biochimica et Biophysica Acta (BBA) - Bioenergetics* **1858**, 175–181 (2017).
119. Billingham, L. K. *et al.* Mitochondrial electron transport chain is necessary for NLRP3 inflammasome activation. *Nature Immunology* **2022** 23:5 **23**, 692–704 (2022).
120. Shouval, D. S. *et al.* Interleukin-10 receptor signaling in innate immune cells regulates mucosal immune tolerance and anti-inflammatory macrophage function. *Immunity* **40**, 706–719 (2014).
121. Zigmond, E. *et al.* Macrophage-restricted interleukin-10 receptor deficiency, but not IL-10 deficiency, causes severe spontaneous colitis. *Immunity* **40**, 720–733 (2014).


122. Carl, V. S., Gautam, J. K., Comeau, L. D. & Smith, M. F. Role of endogenous IL-10 in LPS-induced STAT3 activation and IL-1 receptor antagonist gene expression. *J Leukoc Biol* **76**, 735–742 (2004).
123. Huynh, J., Chand, A., Gough, D. & Ernst, M. Therapeutically exploiting STAT3 activity in cancer — using tissue repair as a road map. *Nature Reviews Cancer* **2018** 19:2 **19**, 82–96 (2018).
124. Noe, J. T. & Mitchell, R. A. Tricarboxylic acid cycle metabolites in the control of macrophage activation and effector phenotypes. *J Leukoc Biol* **106**, 359–367 (2019).
125. Chun, K. S., Jang, J. H. & Kim, D. H. Perspectives Regarding the Intersections between STAT3 and Oxidative Metabolism in Cancer. *Cells* **2020**, Vol. 9, Page 2202 **9**, 2202 (2020).
126. Xie, Y., Kole, S., Precht, P., Pazin, M. J. & Bernier, M. S-Glutathionylation Impairs Signal Transducer and Activator of Transcription 3 Activation and Signaling. *Endocrinology* **150**, 1122–1131 (2009).
127. Sancho, D., Enamorado, M. & Garaude, J. Innate immune function of mitochondrial metabolism. *Frontiers in Immunology* vol. 8 Preprint at <https://doi.org/10.3389/fimmu.2017.00527> (2017).
128. Benmoussa, K., Garaude, J. & Acín-Pérez, R. How Mitochondrial Metabolism Contributes to Macrophage Phenotype and Functions. *Journal of Molecular Biology* vol. 430 3906–3921 Preprint at <https://doi.org/10.1016/j.jmb.2018.07.003> (2018).
129. Mimaki, M., Wang, X., McKenzie, M., Thorburn, D. R. & Ryan, M. T. Understanding mitochondrial complex I assembly in health and disease. *Biochimica et Biophysica Acta (BBA) - Bioenergetics* **1817**, 851–862 (2012).
130. Walloschke, B., Fuhrmann, H. & Schumann, J. Macrophage cell line RAW264.7 but not P-388D1 is an appropriate in vitro-model for studying

- oxidative burst as well as cytokine production in context of fatty acid enrichment. *Cell Immunol* **262**, 58–61 (2010).
131. Scrima, R. *et al.* Para-hydroxyphenylpyruvate inhibits the pro-inflammatory stimulation of macrophage preventing LPS-mediated nitro-oxidative unbalance and immunometabolic shift. *PLoS One* **12**, e0188683 (2017).
 132. Ugalde, C. *et al.* Human mitochondrial complex I assembles through the combination of evolutionary conserved modules: a framework to interpret complex I deficiencies. *Hum Mol Genet* **13**, 2461–2472 (2004).
 133. Lazarou, M., McKenzie, M., Ohtake, A., Thorburn, D. R. & Ryan, M. T. Analysis of the Assembly Profiles for Mitochondrial- and Nuclear-DNA-Encoded Subunits into Complex I. *Mol Cell Biol* **27**, 4228–4237 (2007).
 134. Antonicka, H. *et al.* Identification and Characterization of a Common Set of Complex I Assembly Intermediates in Mitochondria from Patients with Complex I Deficiency. *Journal of Biological Chemistry* **278**, 43081–43088 (2003).
 135. Ogilvie, I., Kennaway, N. G. & Shoubridge, E. A. A molecular chaperone for mitochondrial complex I assembly is mutated in a progressive encephalopathy. *J Clin Invest* **115**, 2784–2792 (2005).
 136. Ugalde, C., Janssen, R. J. R. J., van den Heuvel, L. P., Smeitink, J. A. M. & Nijtmans, L. G. J. Differences in assembly or stability of complex I and other mitochondrial OXPHOS complexes in inherited complex I deficiency. *Hum Mol Genet* **13**, 659–667 (2004).
 137. González-Quintana, A. *et al.* Uniparental isodisomy as a cause of mitochondrial complex I respiratory chain disorder due to a novel splicing NDUFS4 mutation. *Mol Genet Metab* **131**, 341–348 (2020).
 138. Janssen, A. J. M. *et al.* Spectrophotometric assay for complex I of the respiratory chain in tissue samples and cultured fibroblasts. *Clin Chem* **53**, 729–734 (2007).

139. Petruzzella, V. *et al.* A nonsense mutation in the NDUF54 gene encoding the 18 kDa (AQDQ) subunit of complex I abolishes assembly and activity of the complex in a patient with Leigh-like syndrome. *Hum Mol Genet* **10**, 529–535 (2001).
140. Budde, S. M. S. *et al.* Clinical heterogeneity in patients with mutations in the NDUF54 gene of mitochondrial complex I. *J Inherit Metab Dis* **26**, 813–815 (2003).
141. Calvaruso, M. A. *et al.* Mitochondrial complex III stabilizes complex I in the absence of NDUF54 to provide partial activity. *Hum Mol Genet* **21**, 115–120 (2012).
142. Rossignol, R. *et al.* Energy substrate modulates mitochondrial structure and oxidative capacity in cancer cells. *Cancer Res* **64**, 985–993 (2004).
143. Zhao, R. Z., Jiang, S., Zhang, L. & Yu, Z. Bin. Mitochondrial electron transport chain, ROS generation and uncoupling (Review). *Int J Mol Med* **44**, 3–15 (2019).
144. Pagano, G. *et al.* Oxidative stress and mitochondrial dysfunction across broad-ranging pathologies: toward mitochondria-targeted clinical strategies. *Oxid Med Cell Longev* **2014**, (2014).
145. Leadsham, J. E. *et al.* Loss of cytochrome c oxidase promotes RAS-dependent ROS production from the ER resident NADPH oxidase, Yno1p, in yeast. *Cell Metab* **18**, 279–286 (2013).
146. Cai, S. *et al.* Mitochondrial dysfunction in macrophages promotes inflammation and suppresses repair after myocardial infarction. *J Clin Invest* **133**, (2023).
147. García Del Río, A. *et al.* The Mitochondrial Isoform of FASTK Modulates Nonopsonic Phagocytosis of Bacteria by Macrophages via Regulation of Respiratory Complex I. *J Immunol* **201**, 2977–2985 (2018).

148. Cardaci, S. *et al.* Pyruvate carboxylation enables growth of SDH-deficient cells by supporting aspartate biosynthesis. *Nat Cell Biol* **17**, 1317–1326 (2015).
149. Saxena, N. *et al.* SDHB-Deficient Cancers: The Role of Mutations That Impair Iron Sulfur Cluster Delivery. *J Natl Cancer Inst* **108**, (2016).
150. Bezawork-Geleta, A., Rohlena, J., Dong, L., Pacak, K. & Neuzil, J. Mitochondrial Complex II: At the Crossroads. *Trends Biochem Sci* **42**, 312–325 (2017).
151. Lorendeau, D. *et al.* Dual loss of succinate dehydrogenase (SDH) and complex I activity is necessary to recapitulate the metabolic phenotype of SDH mutant tumors. *Metab Eng* **43**, 187–197 (2017).
152. Guzy, R. D., Sharma, B., Bell, E., Chandel, N. S. & Schumacker, P. T. Loss of the SdhB, but Not the SdhA, Subunit of Complex II Triggers Reactive Oxygen Species-Dependent Hypoxia-Inducible Factor Activation and Tumorigenesis. *Mol Cell Biol* **28**, 718–731 (2008).
153. Bae, H. *et al.* AMP-activated protein kinase enhances the phagocytic ability of macrophages and neutrophils. *FASEB J* **25**, 4358–4368 (2011).
154. Guragain, D. *et al.* AMPK is essential for IL-10 expression and for maintaining balance between inflammatory and cytoprotective signaling. *Biochimica et Biophysica Acta (BBA) - General Subjects* **1864**, 129631 (2020).
155. Benkhart, E. M., Siedlar, M., Wedel, A., Werner, T. & Ziegler-Heitbrock, H. W. L. Role of Stat3 in Lipopolysaccharide-Induced IL-10 Gene Expression. *The Journal of Immunology* **165**, 1612–1617 (2000).
156. Dowling, J. K. *et al.* Mitochondrial arginase-2 is essential for IL-10 metabolic reprogramming of inflammatory macrophages. *Nat Commun* **12**, (2021).
157. Maklashina, E., Rajagukguk, S., Iverson, T. M. & Cecchini, G. The unassembled flavoprotein subunits of human and bacterial complex II have

- impaired catalytic activity and generate only minor amounts of ROS. *Journal of Biological Chemistry* **293**, 7754–7765 (2018).
158. Wen, Z., Zhong, Z. & Darnell, J. E. Maximal activation of transcription by Stat1 and Stat3 requires both tyrosine and serine phosphorylation. *Cell* **82**, 241–250 (1995).
159. Zhang, X., Blenis, J., Li, H. C., Schindler, C. & Chen-Kiang, S. Requirement of Serine Phosphorylation for Formation of STAT-Promoter Complexes. *Science (1979)* **267**, 1990–1994 (1995).
160. Chung, J., Uchida, E., Grammer, T. C. & Blenis, J. STAT3 Serine Phosphorylation by ERK-Dependent and -Independent Pathways Negatively Modulates Its Tyrosine Phosphorylation. *Mol Cell Biol* **17**, 6508–6516 (1997).
161. Lim, C. P. & Cao, X. Serine phosphorylation and negative regulation of Stat3 by JNK. *Journal of Biological Chemistry* **274**, 31055–31061 (1999).
162. Wegrzyn, J. *et al.* Function of mitochondrial Stat3 in cellular respiration. *Science (1979)* **323**, 793–797 (2009).
163. Viola, A., Munari, F., Sánchez-Rodríguez, R., Scolaro, T. & Castegna, A. The metabolic signature of macrophage responses. *Frontiers in Immunology* vol. 10 Preprint at <https://doi.org/10.3389/fimmu.2019.01462> (2019).
164. Hooftman, A. *et al.* The Immunomodulatory Metabolite Itaconate Modifies NLRP3 and Inhibits Inflammasome Activation. *Cell Metab* **32**, 468-478.e7 (2020).
165. Hoyle, C., Green, J. P., Allan, S. M., Brough, D. & Lemarchand, E. Itaconate and fumarate derivatives inhibit priming and activation of the canonical NLRP3 inflammasome in macrophages. *Immunology* **165**, 460–480 (2022).
166. Bambouskova, M. *et al.* Itaconate confers tolerance to late NLRP3 inflammasome activation. *Cell Rep* **34**, (2021).

- 
167. Kurczy, M. E. *et al.* Global Isotope Metabolomics Reveals Adaptive Strategies for Nitrogen Assimilation. *ACS Chem Biol* **11**, 1677–85 (2016).
168. Pacesa, M. *et al.* Structural basis for Cas9 off-target activity. *Cell* **185**, 4067-4081.e21 (2022).
169. Yin, M. & O'Neill, L. A. J. The role of the electron transport chain in immunity. *The FASEB Journal* **35**, e21974 (2021).
170. Yang, Y. *et al.* Succinate dehydrogenase inhibitor dimethyl malonate alleviates LPS/d-galactosamine-induced acute hepatic damage in mice. *Innate Immun* **25**, 522–529 (2019).
171. Xu, J. *et al.* Inhibiting Succinate Dehydrogenase by Dimethyl Malonate Alleviates Brain Damage in a Rat Model of Cardiac Arrest. *Neuroscience* **393**, 24–32 (2018).

Annexes



Table 1: Oligonucleotides and primers used for cloning

Name	Description	Sequence
CL1	gRNA Ndufs4 FWD	5'– <u>CACC</u> TCGCTGAGACAGGCGATGTT–3'
CL2	gRNA Ndufs4 REV	5'– <u>AAAC</u> AACATCGCCTGTCTCAGCGC–3'
CL3	gRNA Sdha FWD	5'– <u>CACC</u> GGCGGGCGCTTGGCGTAACTG–3'
CL4	gRNA Sdha REV	5'– <u>AAAC</u> CAGTTAACGCCAAGCGCCGC–3'
CL5	gRNA Sdhb FWD	5'– <u>CACC</u> GAGCCGGGAAGCCGCGCTTCA–3'
CL6	gRNA Sdhb REV	5'– <u>AAAC</u> TGAAGCGCGGCTTCCCGGCTC–3'
CL7	Ndufs4 BLAS FWD	5'–TAA <u>GTCGACT</u> CGCTGAGACAGGCGATGTT <u>AG</u> <u>G</u> TAGATAGTTAGCGACAATCCCGGGTCTCCGCG –3'
CL8	Ndufs4 BLAS REV	5'–ATT <u>GGAT</u> <u>CCTAACATCGCCTGTCTCAGCGAG</u> <u>GCTGCAGGAATTCGATCTGGG</u> –3'
CL9	Sdha BLAS FWD	5'–TAA <u>GTCGACTT</u> CGAGGCTTCTTCGCGGG <u>AGG</u> <u>TAGATAGTTAGCGACAATCCCGGGTCTCCGCG</u> – 3'
CL10	Sdha BLAS REV	5'–ATT <u>GGAT</u> <u>CCTCCCGCGAAGAAGCCTCGAAG</u> <u>GCTGCAGGAATTCGATCTGGG</u> –3'
CL11	Sdhb BLAS FWD	5'–TAA <u>GTCGAC</u> AGCCGGGAAGCCGCGCTT <u>CAA</u> <u>GG</u> TAGATAGTTAGCGACAATCCCGGGTCTCCGCG <u>G</u> –3'
CL12	Sdhb BLAS REV	5'–ATT <u>GGAT</u> <u>CCTTGAAGCGCGGCTTCCCGGCTG</u> <u>GCTGCAGGAATTCGATCTGGG</u> –3'

Bold: target sequences, PAM sequences are underlined. Red: restriction enzyme sites (Sall in CL5 and CL7, BamHI in CL6 and CL8), BbsI compatible overhangs are underlined. Orange: stop sequences. Green: sequences that match with pBluescript II KS+.

Table 2: Primers used for PCR and sequencing

Name	Description	Sequence
CL13	Ndufs4 Gen FWD	5'-GGGCTTCTCAGCCTCAATGT-3'
CL14	Ndufs4 Gen REV	5'-GAGCCACGATCCAGTTCACA-3'
CL15	Sdha Gen FWD Bis1	CCTACCTCAGACGTGTTGGCC
CL16	Sdha Gen REV Bis1	ACGAATAACAGGTGACCGGC
CL17	Sdha Gen FWD Bis2	GCAGAATCTTCCAAGCCCGA
CL18	Sdha Gen REV Bis2	CGCAACACTGGATGAACACG
CL15	Sdhb Gen FWD	5'-TGTACCGACGTGACGTTTCAT-3'
CL16	Sdhb Gen REV	5'-AGGCCTCCCTTTCACACAAG-3'
CL17	Insert blast FWD	5'-TAAGGCATAGGCATCAGGGG-3'
CL18	Insert blast REV	5'-GCAGGCGTTACATAACTTACGG-3'
CL19	Seq PX330 FWD	5'-ACTATCATAGCTTACCGTAAC-3'

Table 3: Primers used for real-time PCR

Name	Description	Sequence
RT1	Arg1-FWD	5'-AAGAATGGAAGAGTCAGTGTGG-3'
RT2	Arg1-REV	5'-GGGAGTGTTGATGTCAGTGTG-3'
RT3	Bcl3-FWD	5'-CACCCCTACTCCATGATATGC-3'
RT4	Bcl3-REV	5'-AGACAGCGGCTATGTTATTCTG-3'
RT5	Hprt-FWD	5'-GCGTCGTGATTAGCGATGATG-3'
RT6	Hprt-REV	5'-GAGCAAGTCTTTCAGTCCTGT-3'
RT7	IFN- β -FWD	5'-GATGACGGAGAAGATGCAGAAG-3'
RT8	IFN- β -REV	5'-ACCCAGTGCTGGAGAAATTG-3'
RT9	IL-6-FWD	5'-CTTCCATCCAGTTGCCTTCT-3'
RT10	IL-6-REV	5'-CTCCGACTTGTGAAGTGGTATAG-3'
RT11	IL-10-FWD	5'-ACAGCCGGGAAGACAATAAC-3'
RT12	IL-10-REV	5'-CAGCTGGTCCTTTGTTTGAAG-3'
RT13	Socs3-FWD	5'-GAAGATTCCGCTGGTACTGAG-3'
RT14	Socs3-REV	5'-GCTGGGTCACTTTCTCATAGG-3'
RT15	Tnf- α -FWD	5'-AGCCGATGGGTTGTACCTTGTCTA-3'
RT16	Tnf- α -REV	5'-TGAGATAGCAAATCGGCTGACGGT-3'

Table 4: Antibodies used for Western blot

Reagent	Source	Identifier
iNOS Monoclonal Antibody (CXNFT), APC	Thermo Fisher Scientific	Cat#17-5920-82; RRID:AB_2573244
Monoclonal antibody anti- β -actin-peroxidase	Sigma-Aldrich	Cat#A3854; RRID:AB_262011
Rabbit polyclonal anti-AMPK α	Cell Signaling	Cat#2532; RRID:AB_330331
Rabbit polyclonal anti-Phospho-AMPK α (Thr172)	Cell Signaling	Cat#2531; RRID:AB_330330
Rabbit polyclonal anti-HIF-1 α	Novus Biologicals	Cat# NB100-449
Mouse monoclonal anti-SDHA (B-1)	Santa Cruz Biotechnology, Inc.	Cat#sc-166909; RRID:AB_10611174
Mouse monoclonal anti-SDHB (21A11AE7)	Thermo Fisher Scientific	Cat#459230; RRID:AB_2532233
Rabbit polyclonal anti-Stat3	Cell Signaling	Cat#9132;RRID: AB_331588
Mouse monoclonal anti-Phospho-Stat3 (Ser727)	Cell Signaling	Cat#9136; RRID:AB_331755
Rabbit polyclonal anti-Phospho-Stat3 (Tyr705)	Cell Signaling	Cat#9131;RRID: AB_331586
Mouse monoclonal anti-ATP5A	Abcam	Cat#ab14748
Rabbit polyclonal anti-ATP5B	Abcam	Cat#ab128743
Mouse monoclonal anti-COX5A	Abcam	Cat#ab110262
Mouse monoclonal anti-NDUFA9	Abcam	Cat#ab14713
Rabbit polyclonal anti-NDUFS4	Thermo Fisher Scientific	Cat#PA5-92940
Mouse monoclonal anti-NDUFV1	Santa Cruz Biotechnology, Inc.	Cat#sc-100566
Mouse monoclonal anti-UQCR2	Abcam	Cat#ab14745



Table 5: Target site sequencing of *Ndufs4*^{-/-}, *Sdha*^{-/-} and *Sdhb*^{-/-} clones

Gene	Clone	Genotype	Sequence	Modification
<i>Ndufs4</i>	#1	HM	ATGGCGGCGGTCTCAATGTCAGTG TCGCTGAGACAGGCGATGTTATGT ATACCGATCGGATCTGCAGGCGTT ACATAACTTACGGTAAATGGCCCG CCTGGCTGA	Donor plasmid insert
<i>Ndufs4</i>	#2	HM	ATGGCGGCGGTCTCAATGTCAGTG TC -del 49 pb- TCCGTCTGTAGAGTTCCATCCGGT AACATAACTGTCAGCCTTGTCGAG CTATTCATTCAGGGT	Deletion
<i>Ndufs4</i>	#3	HM	AGAACGGAGGAAGTGAGTCCCTAG CGGGGATCCGTA CTGCATCCTGG CGTTTGCCTACAGGGGGCGCGCCG GGATCTATAACTTCGTATAGCATA CATTATACGAAGTTATAAGCTTCA GCATAG	Deletion +Donor plasmid insert
<i>Sdha</i>	#1	HT	ATGGCCGGGGTTGGCGCAGTTTCG AGGCTTCTTCGCGGGCGGCGCTTG GCGTTAAACGCCAAGCGCCGCGGC TGCAGGAATTCGATCTGGGGGCGC GCCGGGATCTATAACTTCGTATAG CATA CA	Donor plasmid insert
			TACCCCTGGAGCAGAGCCCATCAG CGTTGCTGCCACCCTACCTCAGAC GTGCGCGGCGGGCGCTAGGGCGCT GTTATGTATAACCGATCGGATCTGC AGGCGTTACATAACTTACGGTAAA TGGCCC	Deletion +Donor plasmid insert
<i>Sdha</i>	#2	HT	ATGGCCGGGGTTGGCGCAGTTTCG AGGCTTCTTCGCGGGCGGCGCTTG GCGTTACTGAGGTAGATAGTTAGC GACAATCCCGGTCTCCGCGGATA ACTTCGTATAATGTATGCTATACG AAGTTA	Donor plasmid insert
			ATGGCCGGGGTTGGCGCAGTTTCG AGGCTTCTTCGCGGGCGGCGCTTG GCGTTAA -del 28 bp- GGCAGGCGCTAGGAGTGCGCCACG ATTCCACCCGAGTTGGCCTGAGTC TGGGAAGGTGCAG	Deletion

Gene	Clone	Genotype	Sequence	Modification
<i>Sdha</i>	#3	HT	ATG GCCGGGGTGGCGCAGTTTCG AGGCTTCTTCGCGGGCGGCGCTTG GCGTTAA -del 2 bp- GGGCGGTGAGTTAGTGCCACGAAA TGGGGCGGTGAGTTAGTGCCACGA AATGGCAGGCGCT	Deletion
			ATG GCCGGGGTGGCGCAGTTTCG AGGCTTCTTCGCGGG AGGTAGATA GTTAGCGACAATCCCGGGTCTCCG CGGATAACTTCGTATAATGTATGC TATACGAAGTTATGTATAACCGATC GGATCT	Donor plasmid insert
<i>Sdha</i>	#4	HM	ATG GCCGGGGTGGCGCAGTTTCG AGGCTTCTTCGCGGGCGGCGCTTG GCGT CGCCAAGCGCCGCGGCTGCA GGAATTCGATCTGGGGGCGCGCCG GGATCTATAACTTCGTATAGCATA CATTAT	Donor plasmid insert
<i>Sdhb</i>	#1	HM	TGTCGCTAACTAT CCGGCTGCCGT TCTCGGCAGAGT	Donor plasmid insert
<i>Sdhb</i>	#2	HM	CTCAGGGTGAGAGGCCGGCTTCCC ACCGCGG -del 144 bp - AGTGGGGAGCCGTGCCCGT	Deletion
<i>Sdhb</i>	#3	HT	ATG GCGGCGACGGTCGGGGTCTCC TAACGCTTTTTTGACACAACATGGG GGATCATGTAACTCGCCTTGATCG TTGGGAACCGAGCTGAATGAAGC CATACCAA	Donor plasmid insert
			ATG GCGGCGACGGTCGGGGTCTCC TTGAC CAATCCCGGGTCTCCGCGGA TAACTTCGTATAATGTATGCTATA CGAAGTTATGTATAACCGATCGGAT CTGCAGGCG	Donor plasmid insert
<i>Sdhb</i>	#4	HM	ATG GCGGCGACGGTCGGGGTCTCC TT TCAAGCCTCT	Donor plasmid insert

Black: parental RAW 264.7 genomic sequence

Red: donor plasmid sequence

HM: homozygous

HT: heterozygous

Table 6: Key resources table

Reagent or resource	Source	Identifier
Cell lines/Organisms strains/Bacterial strains		
C57BL/6J	The Jackson Laboratory	Cat#000664; RRID:IMSR_JAX:000664
<i>Escherichia coli</i> DH10 β	Thermo Fisher Scientific	Cat#EC0113
<i>Escherichia coli</i> DH5 α	Thermo Fisher Scientific	Cat#18258012
L929 cells	ATCC	RRID:CVCL_AR58
RAW 264.7	ATCC	Cat#TIB-71; RRID:CVCL_0493
Chemicals, peptides, and recombinant proteins		
2,6-Dichloroindophenol sodium salt hydrate (SDS)	Sigma-Aldrich	Cat#D1878; CAS:1266615-56-8
4-Octyl itaconate	Sigma-Aldrich	Cat#SML2338; CAS:3133-16-2
Rat Monoclonal anti-CD210/IL-10R (1B1.3a)	Thermo Fisher Scientific	Cat#16-2101-85; RRID:AB_2573082
Antimycin A	Sigma-Aldrich	Cat# A8674; CAS:1397-94-0
BamHI	Thermo Fisher Scientific	Cat#ER0051
BbsI	Thermo Fisher Scientific	Cat#ER1012
Blasticidin	Invivogen	Cat#ant-bi-05
Calcium chloride	VWR Chemicals	Cat#22317.260
Carbonyl cyanide 4-(trifluoromethoxy)phenylhydrazone (FCCP)	Sigma-Aldrich	Cat#C2920; CAS:370-86-5
Chloroform	Thermo scientific	Cat#158210025
Compound C	Sigma-Aldrich	Cat#171260; CAS:866405-64-3
Decylubiquinone	Sigma-Aldrich	Cat#D7911; CAS:55486-00-5
Dimethyl fumarate	Thermo Fisher Scientific	Cat#11324489; CAS:624-49-7
Dimethyl malonate	Thermo Fisher Scientific	Cat#A11007; CAS:108-59-8
Dimethyl sulfoxide (DMSO)	Fisher bioreagents	Cat#BP231-1 CAS:67-68-5
dNTPs	EURx	Cat#E0502-02
Dulbecco's Modified Eagle's Medium (DMEM)	Gibco	Ref 41965-039
EDTA	VWR Chemicals	Cat#443882G
Ethanol	labkem	Ref#ETHA-90P-5K0
Fetal bovine serum (FBS)	Gibco	Ref 10270-106
Fluorescein-5-Isothiocyanate (FITC)	Thermo Fisher Scientific	Cat#F1906; CAS:3326-32-7
Glycogen	Thermo Scientific	Cat#R0561
Isopropanol	Davila Villalobos SL.	Cat#1219 CAS:67-63-0
Laemli buffer	Serva	Cat#42526.02
LB agar, Lennox	Becton-Dickinson	Cat#240110
LB broth, Lennox	Fisher bioreagents	Cat#BP1427-2 CAS:73049-73-7
L-glutamine	Gibco	Ref#25030-081
Lipopolysaccharides from <i>Escherichia coli</i> O55:B5	Sigma-Aldrich	Cat#L6529
Magnesium chloride	VWR Chemicals	Cat#25108.260
MitoSOX Red	Thermo Fisher Scientific	Cat#M36008
MitoTEMPO	Sigma-Aldrich	Cat#SML0737; CAS:1334850-99-5
MitoTracker Red CMXRos	Thermo Fisher Scientific	Cat#M7512; CAS:167095-09-2

Reagent or resource	Source	Identifier
MitoView Green	Biotium	Cat#70054
Mouse IL-10 Recombinant Protein	Thermo Fisher Scientific	Cat#RMIL105
Non-essential amino acids (NEAA)	Gibco	Ref#11140-035
Oligomycin A	Sigma-Aldrich	Cat#75351; CAS:579-13-5
Penicillin/ streptomycin	Gibco	Ref#15070-063
Phosphate-buffered saline (PBS)	Fisher bioreagents	Cat#BP399-1
Phusion™ Hot Start II DNA polymerase	Thermo Scientific	F549L
PowerUp SYBR Green PCR Master Mix	Thermo Fisher Scientific	Cat#A25742
Proteinase K	iNtRON Biotechnology	Cat#R314-0741.46
Recombinant Mouse IL-10	Thermo scientific	Cat#RMIL105
Rotenone	Sigma-Aldrich	Cat#R8875; CAS:83-79-4
Sall	Thermo Fisher Scientific	Cat#ER0641
Sodium chloride	Fisher Scientific	Cat#S/3160/65
Sodium pyruvate	Gibco	Ref#11360-039
Tris Base	Fisher Scientific	Cat#BP152-1 CAS:77-86-1
TRIzol	Thermo Fisher Scientific	Cat#15596026
Trypsin-EDTA	Corning	Cat#25-052-CV
XF Base Medium	Agilent Technologies	Cat#103193-100
Commercial assays		
ABTS ELISA Buffer Kit	Peprotech	Cat#900-K00
Buffers P1, P2, and P3	Qiagen	Cat#19051/2/3
First Strand cDNA Synthesis Kit	Thermo Fisher Scientific	Cat#K1612
Fumarate Assay Kit	Sigma-Aldrich	Cat#MAK060
Griess Reagent Kit for Nitrite Determination	Thermo Fisher Scientific	Cat#G7921
Mouse IFN-β ELISA kit	Finetest	Cat#EM1148
Murine IL-10 Mini ABTS ELISA Development Kit	Peprotech	Cat#900-M53
Murine IL-1β Mini ABTS ELISA Development Kit	Peprotech	Cat#900-M47
Murine IL-6 Mini ABTS ELISA Development Kit	Peprotech	Cat#900-M50
Murine TNF-α Mini ABTS ELISA Development Kit	Peprotech	Cat#900-M54
Pierce Detergent Compatible Bradford Assay Reagent	Thermo Scientific	# 23246
Pierce MicroBCA Protein Assay kit	Thermo FisherScientific	#23235
PureLink HiPure Plasmid Midiprep kit	Thermo Fisher Scientific	K210005
Seahorse XFp Real-Time ATP Rate Assay Kit	Agilent Technologies	Cat# 103591-100
Succinate Colorimetric Assay Kit	Sigma-Aldrich	Cat#MAK184
Oligonucleotides/ Recombinant DNA		
Oligonucleotides (see Table 1-3)	Sigma-Aldrich	https://www.sigmaaldrich.com/
pBluescript II KS+	Stratagene	Cat#212207
pX330-U6-Chimeric_BB-CBh-hSpCas9	Cong <i>et al.</i> , 2013	Addgene Plasmid #42230
Software and algorithms		
CRISPOR	Concordet <i>et al.</i> , 2018	http://crispor.tefor.net/
GraphPad Prism v.8.0	GraphPad Software	https://www.graphpad.com/

Reagent or resource	Source	Identifier
ImageJ	Schneider <i>et al.</i> , 2012	https://imagej.nih.gov/ij/
Kaluza software version 1.1 Leica	Beckman Coulter Life Sciences	https://www.beckman.com/
Wave version 2.6.3	Agilent Technologies	https://www.agilent.com/
Equipment		
Densitometer Umax PowerLook 2100XL	BIO-RAD	GS-800
Cytation 5 Cell Imaging Multi-Mode Reader	BioTek Instruments	Serial#21010727
Gallios Flow Cytometer	Beckman Coulter Life Sciences	https://www.beckman.com/
LightCycler 480	Roche Diagnostics	Serial#25230
MyCycler™ Thermal Cycler	BIO-RAD	Serial#563BR1536
NanoDrop 1000	NanoDrop technologies	Serial#E611
PowerPac power source	Bio-Rad	Serial#041BR84317
Q-TOF mass spectrometer	Waters	SYNAPT HDMS G2
Seahorse XFp Extracellular Flux Analyzer	Agilent Technologies	Model #S7802A
VersaMax microplate reader	Molecular Devices	https://www.moleculardevices.com/
Other		
Acquity CORTECS UPLC C18 column	(Waters)	Ref#176003149
Amicon® Ultra-0.5 centrifugal filter	Merck, Millipore	Ref#UFC501024
NativePAGE Bis-Tris gel	Thermo Fisher Scientific	Ref#BN1001BOX



Solutions composition

-GMC buffer: 50 mM CaCl₂, 50 mM MgCl₂

-Laemli buffer 5X: 325 mM Tris-HCl pH 7.5, 50% glycerol, 10% (w/v) SDS, 10% β-mercaptoethanol, and 0,01 mg/mL bromophenol blue.

-Lysis buffer: 10 mM Tris-HCl, 10 mM NaCl, 0.5% SDS, 10 mM EDTA.

-RIPA buffer: 150 mM NaCl, 1 mM EDTA, 20 mM Tris-HCl pH 7.4, 0.1% SDS, 1% Sodium deoxycholate, 1% Nonidet P-40 (v/v).

-Running buffer: 25 mM Tris base, 192 mM glycine and 0.1% SDS, pH 8.3.

-TAE buffer: 40 mM Tris-HCl pH 8.2, 1 mM EDTA, 20 mM Acetic acid.

-TE buffer: 10 mM Tris-HCl pH 8, 1 mM EDTA.

-Transfer buffer: 25 mM Tris base, 192 mM glycine, 10% methanol (v/v).

-TTBS (TBS-Tween): 10 mM Tris-HCl pH 7.6, 137 mM NaCl, 0.05% Tween-20 (v/v).